

HYDROGEOLOGIC AND SPELEOGENETIC CONSTRAINTS OF A COASTAL
KARST AQUIFER: SISTEMA JAGUAR, QUINTANA ROO, MEXICO

by

Aubri A. Jenson, B.S.

A dissertation submitted to the Graduate Council of
Texas State University in partial fulfillment
of the requirements for the degree of
Doctor of Philosophy
with a Major in Aquatic Resources and Integrated Biology
December 2019

Committee Members:

Benjamin F. Schwartz, Chair

Patricia A. Beddows

Yongli Gao

Thomas B. Hardy

Todd M. Swannack

COPYRIGHT

by

Aubri A. Jenson

2019

FAIR USE AND AUTHOR'S PERMISSION STATEMENT

Fair Use

This work is protected by the Copyright Laws of the United States (Public Law 94-553, section 107). Consistent with fair use as defined in the Copyright Laws, brief quotations from this material are allowed with proper acknowledgement. Use of this material for financial gain without the author's express written permission is not allowed.

Duplication Permission

As the copyright holder of this work I, Aubri A. Jenson, authorize duplication of this work, in whole or in part, for educational or scholarly purposes only.

DEDICATION

This work is dedicated to my parents, John and Cheryle Jenson,
who always encouraged my scientific curiosity.

ACKNOWLEDGEMENTS

I have my committee members to thank for their input and guidance on the scope of this work: Patricia Beddows, Yongli Gao, Thom Hardy, and Todd Swannack. Patricia Beddows provided a tremendous amount of insight into the hydrogeology of the project area that she has studied for so many years, and she encouraged me to think critically and creatively to develop my own ideas. Yongli Gao and his students, Lijun Tian and Yunxia Li, provided the technical expertise and lab work for the Uranium-Thorium (U-Th) dating in Chapter. 4. He also provided guidance on many of the statistical methods used in Chapter 2. Thank you to Thom Hardy and Todd Swannack for providing reviews from outside perspectives that led me to design a project with a clear sense of purpose and realistic objectives.

Peter Sprouse deserves recognition as the de-facto patron of this research. Scientific work near Paamul was a natural extension of his 10-year commitment to map caves with the highest quality standards and to share data with explorers and scientists alike. I've also learned a great deal from his organized and thoughtful leadership style.

Lorena Martinez was an invaluable field assistant, without whom the final season of fieldwork may not have been possible. In addition to assisting with scientific tasks, she contributed her language skills, and helped in many other ways, despite being paid primarily in tacos and beer.

I am indebted to many cavers for their help and company in the field over the course of six two-weeks trips occurring between December 2015 and August 2018. The following people willingly chopped trails through the jungle, retrieved data loggers, counted holes in the ground, carried rocks in their pack, or otherwise contributed directly to this research: Cait McCann, Jessica Gordon, Andy Edwards, Edgar Garcia, Galen Falgout, Guin McDaid, Alan Cobb, and Larry Keel. I thank Barbara Luke for her field assistance and mentorship, and Nick Banks for his role as a gracious host and guide on several adventures. Natalie Gibb & Rory O’Keefe, two exceptional cave divers, have my gratitude for exploring the far reaches of Sistema Jaguar and obtaining underwater speleothem samples despite challenging logistical conditions. A thank-you also goes to all of the guides and management of Rio Secreto who not only permit scientific work in their caves but encourage it and reach out to educate the public.

I have friends and family to thank for support and encouragement over the years, especially during times when it would have been easier to quit. Thank you to Saj Zapitello, Andrea Croskrey, Dalila Loiacomo, and Will Coleman for feedback on presentations and project scope. I also am grateful to Jean Krejca, Krista McDermid, and all of my coworkers at Zara for their professional guidance, camaraderie and moral support. Finally, I want to thank my advisor, Benjamin Schwartz, whose critical eye and attention to detail has refined my work and improved my professionalism.

TABLE OF CONTENTS

	Page
ACKNOWLEDGEMENTS.....	v
LIST OF TABLES.....	x
LIST OF FIGURES.....	xi
LIST OF ABBREVIATIONS.....	xv
CHAPTER	
1. INTRODUCTION.....	1
1.1 Study Area.....	4
1.1.1 Climate & surface hydrology.....	4
1.1.2 Geologic setting.....	4
1.1.3 Study site.....	9
1.2 Chapter Topics and Objectives.....	13
2. SINKHOLE MORPHOLOGY AND DISTRIBUTION AS INDICATORS OF GEOLOGIC CONTROLS ON KARSTIFICATION AT A SUB-BASIN SCALE: QUINTANA ROO, MEXICO.....	16
2.1 Introduction.....	16
2.1.1 Geologic setting.....	18
2.1.2 Study area.....	20
2.2 Methods.....	22
2.2.1 LiDAR-derived DEM analysis.....	23
2.2.2 Cave entrance data.....	29
2.2.3 Line-intercept field surveys.....	30
2.3 Results.....	33
2.3.1 LiDAR- derived DEM analysis.....	33
2.3.2 Cave entrance data.....	47
2.3.3 Line-intercept field surveys.....	50
2.4 Discussion.....	53
2.4.1 DEM Analysis.....	53

2.4.2	Cave entrance data	57
2.4.3	Line-transect surveys.....	58
2.5	Conclusions	59
3.	CONSTRAINING AQUIFER PROPERTIES IN A TRIPLE-POROSITY COASTAL KARST BASIN: SISTEMA JAGUAR, QUINTANA ROO, MEXICO.....	61
3.1	Introduction	61
3.2	Regional Setting and Study Site.....	67
3.2.1	Geology	67
3.2.2	Climate	68
3.2.3	Study site.....	69
3.3	Materials and Methods	72
3.3.1	Instrumentation and data collection	72
3.3.2	Quantitative analysis	76
3.4	Results	81
3.4.1	Aquifer properties: D, T, and K	81
3.4.2	Hydraulic gradient.....	85
3.4.3	Recession curve analysis.....	89
3.4.4	Estimated discharge and velocity using tidal-derived D... ..	93
3.5	Discussion	94
3.5.1	Aquifer properties	94
3.5.2	Hydraulic gradient.....	96
3.5.3	Recession curve analysis.....	99
3.5.4	Implications for the water budget.....	100
3.6	Conclusions	101
4.	EVIDENCE OF UPLIFT IN THE YUCATAN PENINSULA USING EPIPHREATIC INTERFACE DEPOSITS (EID) AS SEA LEVEL PROXIES: QUINTANA ROO, MEXICO	102
4.1	Introduction	103
4.1.1	Geologic setting.....	104
4.1.2	Karst landscape evolution	105
4.1.3	Uncertainties in sea level history	107
4.1.4	Speleothems as age records and sea level proxies	111
4.2	Methods.....	114

4.2.1	Study site.....	114
4.2.2	Sample collection.....	117
4.2.3	Sample preparation and laboratory analysis.....	120
4.3	Results.....	123
4.4	Discussion.....	127
4.4.1	Evidence of uplift.....	127
4.4.2	Sample outliers.....	130
4.4.3	Accuracy of sea level curves.....	133
4.4.4	Comparison to coral and other speleothem records.....	136
4.4.5	Landscape evolution.....	139
4.5	Conclusions.....	144
5.	CONCLUSIONS.....	146
5.1	Review of Chapter Objectives.....	146
5.1.1	Chapter 2: Identify hydrogeologic controls on karstification.....	146
5.1.2	Chapter 3: Quantify and constrain coastal aquifer properties.....	148
5.1.3	Chapter 4: Constrain timing of conduit development.....	150
5.2	Significance.....	151
5.2.1	Scientific contribution.....	151
5.2.2	Application and social impact.....	152
6.	APPENDIX SECTION.....	154
7.	REFERENCES.....	164

LIST OF TABLES

Table	Page
2-1. A comparison of methods for sinkhole identification and analysis.	23
2-2. Summary statistics of depression geometry.	36
2-3. Mean morphometric parameters compared across geologic units.	37
2-4. Sinkholes identified in line-intercept surveys.	52
3-1. Discharge estimates from prior work.	64
3-2. Summary of diffusivity values by site.	84
3-3. Diffusivity calculated using storm event recession curves.	92
3-4. Parameters used to calculate discharge and mean linear velocity.	93
3-5. Comparison of coastal karst aquifer properties from other studies.	96
3-6. Gradient measurements from prior work.	98
4-1. U-Th ages from speleothem samples and their collection elevations.	124
4-2. Fossil corals documented near the study area by prior work.	137
4-3. Modeled and measured rates of tropical karst denudation.	140
4-4. A summary of observations and assumptions of tectonic stability.	144

LIST OF FIGURES

Figure	Page
1-1. A conceptual diagram of research scope.	2
1-2. Tectonic structures of the Yucatan Peninsula.	7
1-3. Geologic map of the Yucatan Peninsula.	8
1-4. Map of large caves in the study area.	11
1-5. Freshwater pools in cave passages in Sistema Jaguar.	12
2-1. Simplified geologic map of the Yucatan Peninsula.	20
2-2. Aerial photo of the study area.	21
2-3. Morphometric parameters describing depression shape.	25
2-4. Diagram of depression orientation measurement.	26
2-5. Diagram of depression alignment measurement.	28
2-6. Map of sinkhole survey transects.	32
2-7. Examples of sinkholes documented in a line-intercept survey.	33
2-8. Processed DEM with depressions of at least 2 m depth.	34
2-9. Frequency distributions of depression size.	35
2-10. Frequency distributions of depression morphology.	37
2-11. Orientations of depressions identified in the DEM.	38
2-12. Point density of depression centroids.	39
2-13. Nearest Neighbor statistic for all centroids.	40
2-14. A frequency plot of 1 st Nearest Neighbor distances.	41

2-15.	Distance to 9 th Nearest Neighbor by geologic unit.....	42
2-16.	Direction to 1 st Nearest Neighbor rose plots.	43
2-17.	Results of Ripley’s K function.	44
2-18.	Kernel Density Map with a search radius of 380 m.	44
2-19.	Clustering identified by Anselin Local Moran’s I.....	45
2-20.	Linear trends of cave passage.....	46
2-21.	Linear trends of all cave passage as defined by bounding boxes.	46
2-22.	Point density comparisons in a 10 x 10 km sampling grid.....	47
2-23.	Access bias in cave entrance data.....	49
2-24.	Map of sinkhole survey transects.	51
2-25.	A box-plot comparison of survey transects.....	52
2-26.	Directional data from field measurements.	53
3-1.	Geologic map of the Yucatan Peninsula.	68
3-2.	Geologic map of the study area with mapped cave passage.	70
3-3.	Summary of water level data collection periods.	73
3-4.	Diagram of water table observation methods.....	75
3-5.	Conceptual diagram of the coastal karst system.	77
3-6.	Workflow used to calculate hydrogeologic properties.....	81
3-7.	Water level data recorded at 1 min intervals on 11-14 August, 2015.....	82
3-8.	Tidal efficiency with distance inland.	83
3-9.	Hydraulic conductivity vs distance inland in Sistema Jaguar.	85

3-10.	Map of the measured coastal hydraulic gradient.....	86
3-11.	Water level elevations from caves and cenotes in the Paamul area.	87
3-12.	Water level and hydraulic gradient response to precipitation.	88
3-13.	Gradient response to tidal signal.	89
3-14.	Analysis of stormwater recession curves.	90
3-15.	Diffusivity values plotted by component type.	91
3-16.	A comparison of K and D values across sites.	92
4-1.	Structural features of the Yucatan Peninsula.	105
4-2.	Conceptual cross-section of coastal karst in Quintana Roo, Mexico.	106
4-3.	A comparison of past sea levels and observed cave elevations.	109
4-4.	A conceptual diagram of Epiphreatic Interface Deposits (EID).	113
4-5.	Assumptions examined in this research.	114
4-6.	Examples of cave passage in Sistema Jaguar.	115
4-7.	Map of the study area.	117
4-8.	Examples of EID <i>in situ</i> in cave passage.	118
4-9.	Speleothem sample elevations.....	119
4-10.	Close-up of a speleothem with EID coatings.	121
4-11.	A reflective scanned image of a slice of EID.	122
4-12.	Speleothem age comparison with sea level records.	126
4-13.	Possible prior conduit depths constrained by uplift.	129
4-14.	A comparison of Pleistocene sea level curves.....	135

4-15.	A comparison of outlier EID elevations.....	136
4-16.	Published U-Th dates from coral and speleothem samples.....	138
4-17.	A diagram representing phases of cave development.	143

LIST OF ABBREVIATIONS

Abbreviation	Description
amsl	above mean sea level
BP	Before Present
bmsl	below mean sea level
EID	Epiphreatic Interface Deposits
ET	Evapotranspiration
Ga	<i>Giga annum</i> (1,000,000,000 years)
ka	<i>kilo annum</i> (1,000 years)
Ma	<i>Milo annum</i> (1,000,000 years)
MAP	Mean Annual Precipitation
MC-ICP-MS	Multi-collector Inductively Coupled Plasma Mass Spectrometry
Th	Thorium
U	Uranium

ABSTRACT

Karst aquifers are self-organizing, scale-dependent systems with highly heterogeneous hydrogeologic properties. Coastal karst systems are especially complex because sea level changes affect porosity development through geologically rapid processes that result in dissolution or deposition. Regional-scale coastal aquifer models often fail to describe heterogeneity at smaller scales because detailed data is unavailable for parameterization. My research evaluates hydrogeologic heterogeneity in the context of formative processes related to sea level history in a coastal karst aquifer sub-basin in Quintana Roo, Mexico. First, I measured and analyzed data describing morphology, distribution, and orientation of sinkholes and cave passages, and investigated their utility as indicators of structural and hydrogeologic controls on karstification. Results suggest that karst features are primarily controlled by hydrogeologic properties and secondarily by structural features. Second, I quantified and constrained aquifer properties of diffusivity, transmissivity, hydraulic conductivity, and hydraulic gradient, using long-term, high-resolution water level data collected in cave passages that intersect the water table. The hydraulic gradient steepens near the coastline, which differs from previous measurements near coastal springs and has implications for water budgets. Finally, I constrained the timing of speleogenesis by comparing sea level records with U-Th dates of speleothems, and calcite overgrowths that form at the water table. Together, these data revealed that conduits are much older than previously assumed, formed at much lower elevations than their current positions, and that significant amounts of both regional uplift

and landscape denudation have occurred. These findings contradict assumptions of recent conduit formation, and tectonic stability in the Yucatan Peninsula throughout the Quaternary. My work concludes that the modern hydrogeologic function and position of conduits is the combined result of dynamic uplift, speleogenesis, and changing sea levels that occurred over the past >650,000 years.

1. INTRODUCTION

An aquifer is a natural system containing enough permeable rock or sediment to conduct groundwater and to yield economically significant quantities of water to wells and springs (Neuendorf et al., 2005). The essential attributes of any aquifer are that it must 1) capture, 2) store, 3) transmit, and 4) discharge groundwater that is available for human use (Ford & Williams, 2007). To effectively manage groundwater, especially in areas of rapid urban or agricultural development, it is essential to have complete and accurate aquifer models that incorporate parameterization or consideration for each of these aspects. A conceptual aquifer model is a representation of the various geologic and hydraulic parameters that control how groundwater is stored and transmitted through rock, and can be applied to construct a better scientific understanding the aquifer (White, 2003). Once the framework of a system has been conceptualized, it may be parameterized through field observations and described as a set of related numerical relationships, which can then be utilized to construct a numerical model (i.e., computer program) to simulate or predict conditions when one or more of these parameters change (Remson et al., 1971) (**Figure 1-1**).

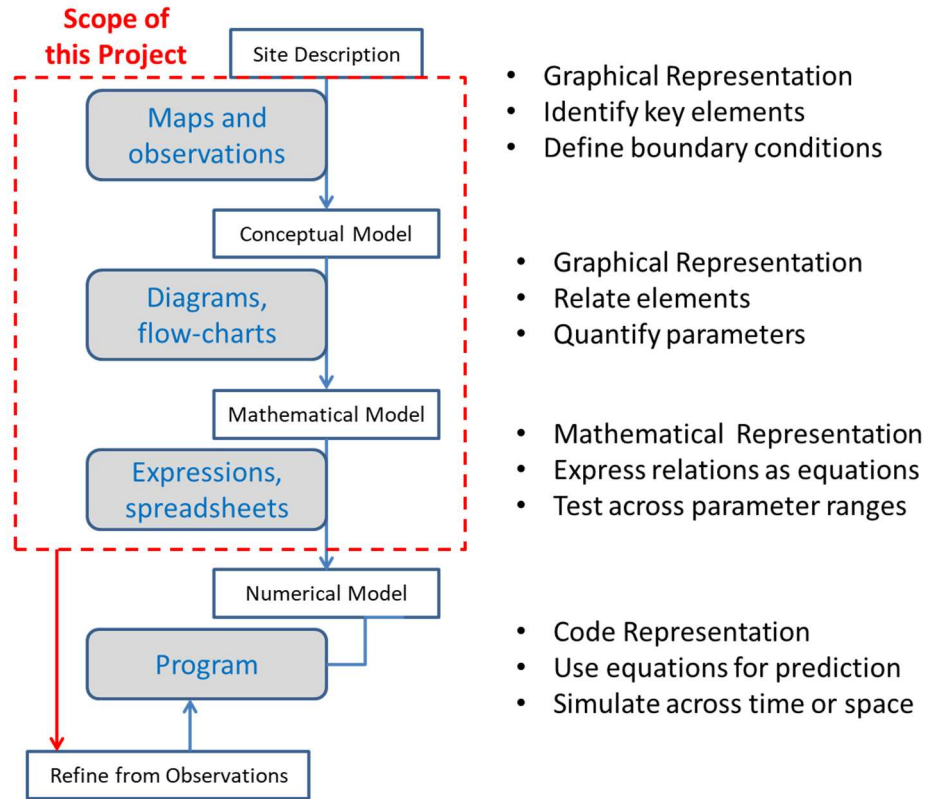


Figure 1-1 A conceptual diagram of research scope. This dissertation provides detailed field data needed to develop accurate groundwater models and to apply them effectively.

A characteristic feature of a karst aquifer is the presence of connected conduits or fractures in the rock that are enlarged or created via chemical dissolution, flow, and solute transport (Worthington et al., 2017). Numerical modeling of karst aquifers is complicated by low-resistance pathways where water can move rapidly through the system and can re-route flow under varying hydrologic conditions or over long time periods (White, 2002). Karst aquifers are dynamic systems that evolve relatively rapidly over geologic time. Where conduits provide pathways for water, they are potentially enlarged by geochemical interactions and mechanical erosion or can be occluded by sediment deposition. Karst models can be divided into contrasting types that describe hydrogeologic variation across space (as a "plumbing system"), and those that describe

geologic evolution across time from a geochemical perspective (White, 2003). The former has practicality for engineering applications (e.g., determining where to drill water wells and how fast to pump them), but the latter addresses questions of basic science. To provide a framework for reliable engineering, a model must describe not only the average modern conditions, but how they vary over time and across regional to local scales. A thorough scientific understanding of an aquifer's evolution provides context for interpreting the hydrogeologic function of the modern system.

The research described in this dissertation provides quantitative characterization of portions of a coastal karst aquifer, informed by insight into the geologic and hydraulic boundary conditions of the system, and new data and hypotheses about its speleogenetic history. Such insights facilitate parameterization of aquifer properties and leads to more reliable solutions to problems of groundwater management.

A large coastal karst aquifer in Quintana Roo, Mexico, on the Caribbean side of the Yucatan Peninsula, supports >1.5 million people and is growing at ~3.5 %/yr (INEGI, 2015). Most prior work has focused on regional-scale aquifer properties (Gondwe, 2010; González-Herrera et al., 2002; Moore et al., 1992), yet these data are often applied at much smaller scales. We examined hydrogeological heterogeneity at a sub-basin scale in the northeastern Yucatan where the water table is accessible in extensive networks of large epiphreatic conduits that intersect the modern water table but were formed under phreatic conditions. These recently mapped systems provide an opportunity to collect new data that offer insight into the origins and hydrodynamics of the modern system.

1.1 Study Area

1.1.1 Climate & surface hydrology

The regional climate of the Yucatan Peninsula is subtropical, with average annual rainfall ranging from 55 cm on the north end of the peninsula to 150 cm along the eastern coast, and precipitation mostly falling during the rainy season between June and October (Bauer-Gottwein et al., 2011). Evapotranspiration (ET) is difficult to quantify but is significant due to dense vegetation and a shallow water table (Bautista et al., 2009). Pan evaporation experiments suggested that ET is about 900 mm/year along the eastern coast (Lesser, 1976). Remote sensing data for 2004-2008 indicated that ET varies spatially from 350 mm/year inland to 1,500 mm/year near the coast (Gondwe, 2010).

The entire northern Yucatan peninsula has a well-drained karstic land surface, and virtually no surface water exists except in low-lying areas where the ground elevation is below the water table (Perry et al., 2009). The southern portion of the peninsula has inland marshes and coastal wetlands. The largest of these, known as the Sian Ka'an Biosphere Reserve, extends ~120 km along the Caribbean coastline between Tulum and Chetumal and has been designated as a UNESCO world heritage site (UNESCO, 2019). Freshwater discharge from the peninsula occurs in the coastal and near shore areas as submarine springs or shallow seeps (Ward et al., 1985), but potentially occurs offshore in deeper springs or seeps.

1.1.2 Geologic setting

The Yucatan Peninsula is part of the Maya tectonic block, which includes the land mass from the modern carbonate shelf, known as the Campeche Bank, to the southern highlands bordering the Chortis Block to the south (**Figure 1-2**). The Maya block, part of

the North American plate, and the Chortis block, part of the Caribbean plate, converge along a strike-slip boundary that extends into the Yucatan Basin (Rosencrantz, 1990). The Maya Block has been in place since the Late Jurassic (163-145 Ma) (Mann, 2007), and the Chortis block collided with it in the Late Cretaceous (100-65 Ma) (Lodolo et al., 2009).

The Chicxulub impact crater, known for marking the cataclysmic end of the Cretaceous period 66 Ma, is centered offshore of the peninsula to the northwest. Although the impact crater has been buried by carbonate deposits 1-2 km thick, its outline is apparent at the exposed surface of the platform where it is bordered by many deep, water-filled pits, called the “Ring of Cenotes”. The Ring of Cenotes is thought to be the surface manifestation of a zone of high permeability developed in Tertiary-age (66-2.6 Ma) carbonate rocks (Perry et al., 2009). Sedimentation during Tertiary time (66-2.6 Ma) was mostly restricted to the region within the buried crater, and a semicircular moat existed until at least Pliocene time (5.3-2.6 Ma) (Pope et al., 1996). Interpretations of gravity data shows patterns in the distribution of karst features east of the Ring of Cenotes and these patterns have been hypothesized to result from deformation related to faulting that parallels the shelf edge of the eastern Yucatan (Connors et al., 1996).

A series of NE-trending normal faults, called the Catoche Fault Zone, extends from the submerged shelf into the eastern central portion of the Yucatan peninsula. This zone had been inferred to reflect subsidence in and adjacent to a Paleozoic basement rock high, the Xcan Arch, that was detected by exploratory oil wells drilled in the 1970s (Ward et al., 1985). In the northeast corner of the peninsula, a ~10 km wide zone of linear depressions trending 5-10° parallel to the coastline is described as the Holbox Fracture

Zone. It was originally described based on LANDSAT imagery (Ward et al., 1985) as extending only 50 km south from the northern shoreline, but gravitational and electromagnetic data (Connors et al., 1996; Gondwe, 2010) have since indicated that it extends as far as 150 km south. The southern extent of the Holbox Fracture Zone intersects the Rio Hondo Fault Zone, a series of parallel normal faults that continues into northern Belize and off shore (Lodolo et al., 2009). The Holbox Fracture Zone has been interpreted as a surficial expression of extension fractures associated with a buried horst-and-graben system, and related to the Rio Hondo Zone and off-shore tectonism (Ward et al., 1985).

Other prominent structural features on the peninsula include the Sierrita de Ticul and the Libertad Arch. The Sierrita de Ticul is a normal fault located to the south of the Ring of Cenotes that trends 305° and is approximately 160 km in length; it is exposed at the surface as a NE facing escarpment (Ward et al., 1985). The fault has been identified as a zone of high permeability based on groundwater geochemistry (Perry et al., 2009). The Libertad Arch is an anticline along the Maya mountains with a fault zone to the south that defines the southern boundary of the Yucatan peninsula (Miller, 1996).

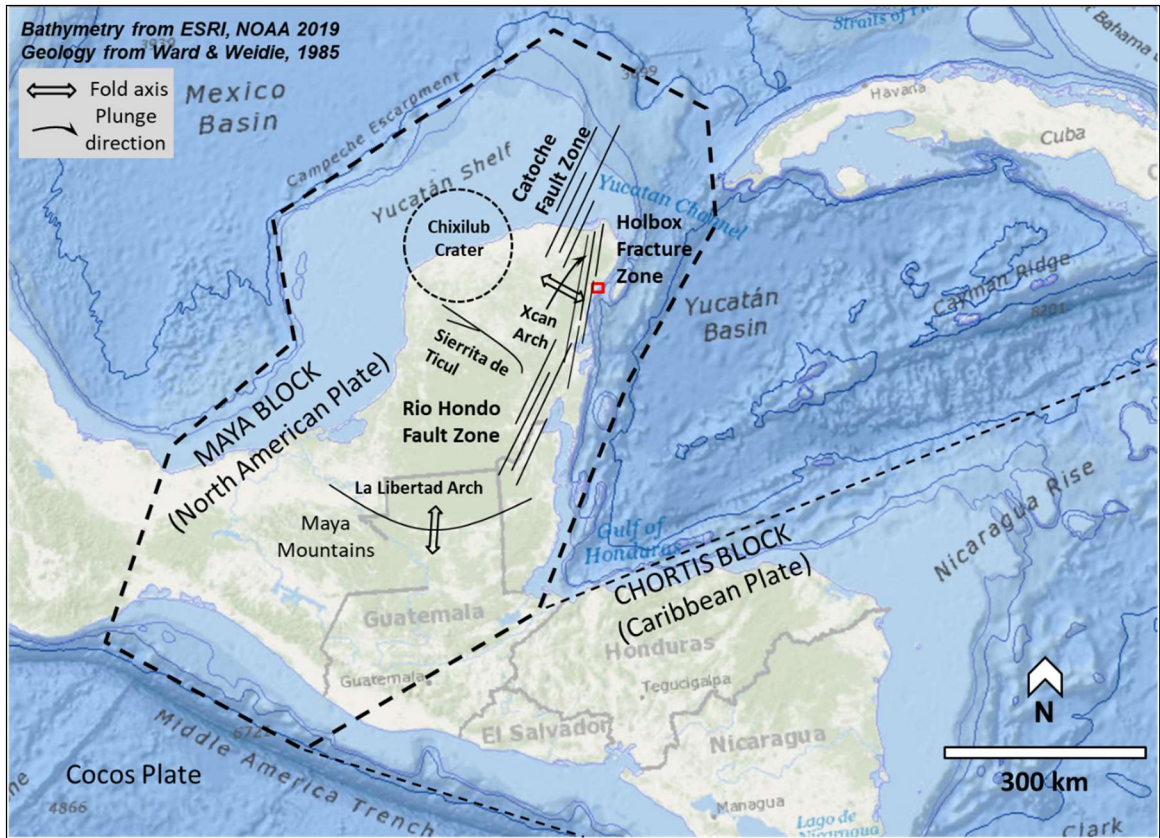


Figure 1-2. Tectonic structures of the Yucatan Peninsula. The study site, outlined in red, is located on the north-eastern edge of the Maya Block. The Holbox Fracture Zone, Rio Hondo Fault Zone, and Catoche Fault Zones are normal fault systems that continue offshore into the Caribbean Sea. Bathymetry lines of 2,000 m outline the extent of the submerged portion of the carbonate platform.

The carbonate strata comprising the peninsula were formed in shallow to deep marine depositional environments that were present from the Cenozoic through the Holocene. These deposits formed a sequence of limestone and dolomite layers >1,500 m thick, below which lie volcanic basement rocks (Ward et al., 1985). Geologic formations exposed at the surface range in age from Eocene (34-56 Ma) limestone at the center of the peninsula to Holocene beach sediments along the coastline (**Figure 1-3**). The upper Pleistocene formation near the coast has been dated to 125 ka BP (Ward et al., 1985), which correlates to the last high stand at 6 m amsl.

The inland limestone in eastern Quintana Roo is thought to be of Pliocene age (2.6-5.3 Ma) (Perry et al., 2009). Coastal carbonates are primarily of Pleistocene-age reef and shallow sea limestones, and beach deposits, with a layer of re-calcified limestone (calcrete) up to a meter thick over much of the surface (Richards & Richards, 2007). The coastline itself consists of Holocene deposits overlying Pleistocene beach-plain aeolianites and reef limestone (Lauderdale et al., 1979).

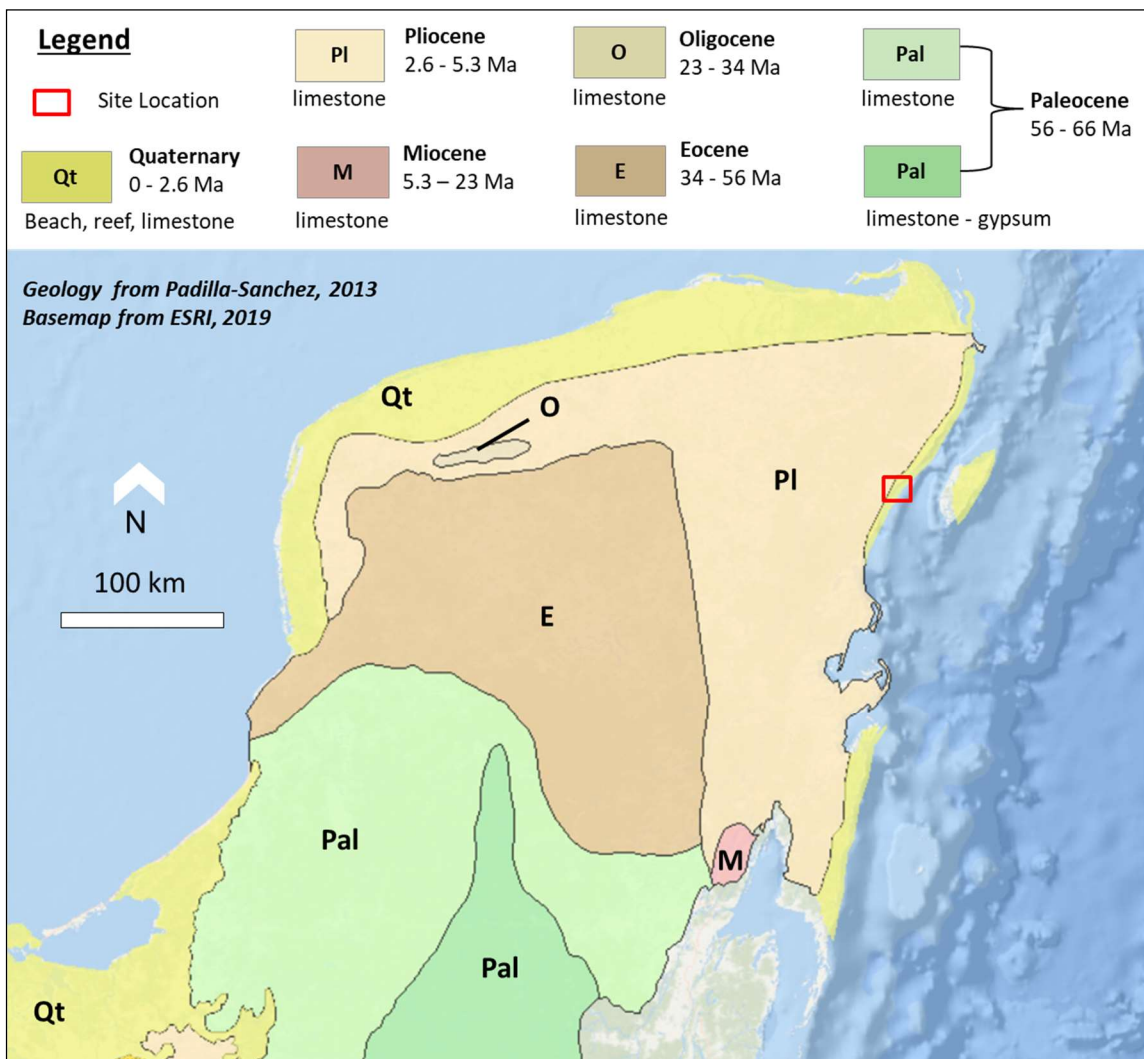


Figure 1-3. Geologic map of the Yucatan Peninsula. The study area is located in Pliocene to Holocene (2.6 Ma - modern) rock and consists of limestone from a variety of depositional environments including reefs, shallow marine deposits, and ancient to modern beaches (data from Padilla-Sanchez, 2013).

While all of the Yucatan Peninsula is heavily karstified, the eastern coastline of Quintana Roo contains an exceptional volume of conduit development, most of which lies between 10 m amsl and 20 m bmsl (Kambesis, 2014). The area around Tulum is known globally for its extensive underwater caves, including Sistema Sac Actun, the world's longest underwater cave containing ~365 km of surveyed passage (QRSS, 2019). Mixing dissolution at the freshwater-saltwater interface is accepted as the primary mode of speleogenesis (Back et al., 1979; Sanford & Konikow, 1989; Smart et al., 2006), although this process could be accelerated by organic input (Gulley et al., 2016a; Haukebo, 2014; Perry et al., 2002) and extensive catchment areas available to provide large amounts of groundwater discharge (Smart et al., 2006).

Underwater caves in eastern Quintana Roo are horizontally extensive, with flat ceilings and wide passages. Most cave passages terminate at 10 to 12 km inland, coinciding with the eastern edge of the Holbox Fracture Zone (Coke, 2012), though this does not define the western watershed boundary. Coastal cave morphology is typically anastomosing and oriented parallel to the shoreline, but inland becomes more linear, fracture controlled, and oriented perpendicular to the coastline. (Kambesis, 2014; Kambesis & Coke, 2016).

1.1.3 Study site

The study area chosen for this research is within 10 km of the coastline near the towns of Paamul and Puerto Aventuras, approximately 70 km south of Cancun, Mexico. Collapse sinkholes that open to the water table (locally called cenotes, from the Mayan word *dznot*) are prevalent and commonly associated with horizontal cave passages

beneath the water. Inland vadose caves (informally known as “dry” caves) are very shallow, often within just a few meters of the surface. Dry caves often have many collapsed entrances, depending on their location and the land elevation; many caves closer to the coast tend to have more collapse. Like underwater caves, passages are horizontally extensive with generally level ceilings and typically contain abundant speleothems.

The cave system selected for this research, Sistema Jaguar, extends 7 km inland perpendicular to the coastline from the Paamul area (**Figure 1-4**). The cave lies entirely at or above the water table, thereby providing relatively easy access on foot and by raft for observing aquifer hydrology and morphology without the need for SCUBA equipment. About 45 km of passage have been mapped in Sistema Jaguar alone, and an additional 215 km have been mapped in adjacent caves (QRSS, 2019). Cave passages tend to be more maze-like nearer to the coastline and gradually converge into a larger single passage inland. Shallow isolated pools <1 m deep are common near the coastline, but water is often 2-5 m deep inland and can form mostly continuous pool networks up to several kilometers in length (**Figure 1-5**). The most-inland passage known in Sistema Jaguar terminates in a singular passage with water up to 5 m deep. Flow toward the coast at ~5-10 cm/s has been observed in a few places in the back of the cave, but velocities are low enough to be difficult or impossible to detect in most of the cave. Tidal or storm related volume changes in isolated pools are assumed to represent flow through the matrix. This exchange could be vertical or horizontal movement between isolated water-table pools and the larger matrix flow system, or via an as-yet undiscovered

hydrologically active conduit network. Other parts of the cave are known to contain unexplored water-filled passages that potentially connect to deeper phreatic conduits.

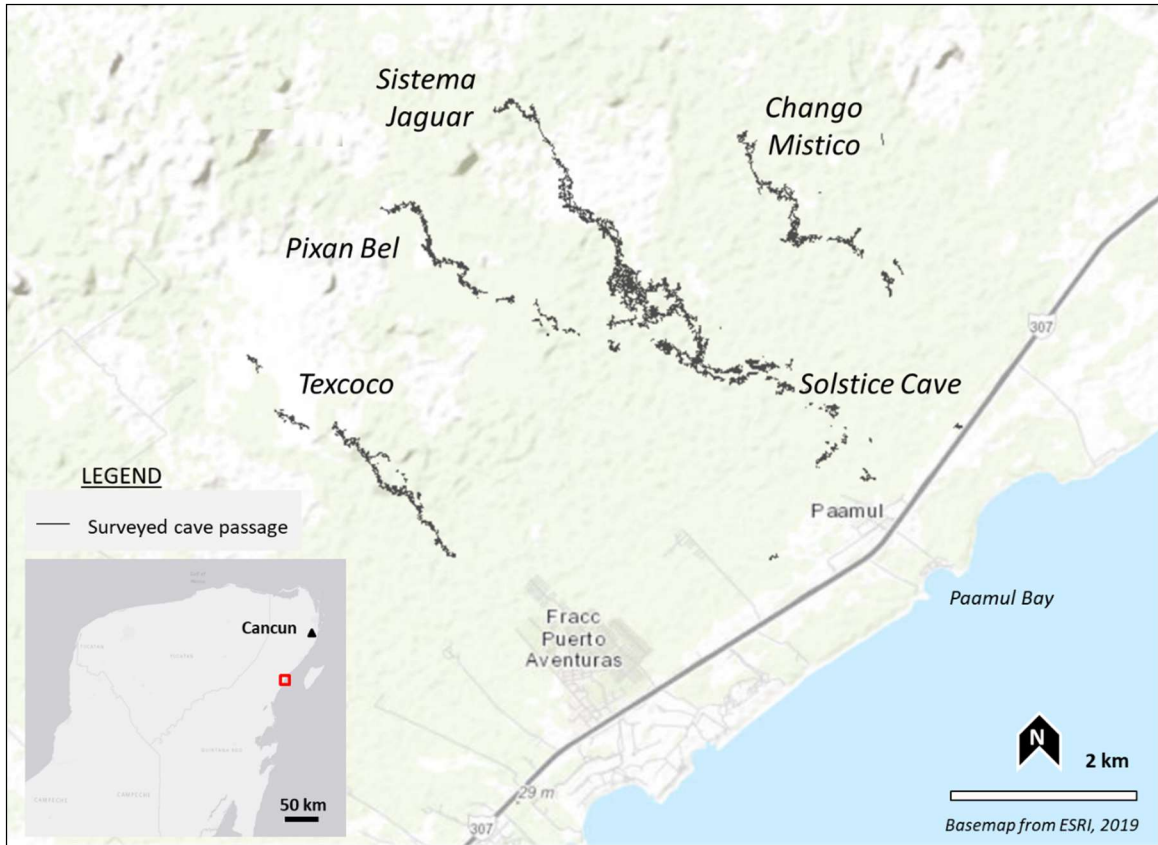


Figure 1-4. Map of large caves in the study area. Known cave systems in the study area are almost exclusively positioned at or above the water table. The largest caves trend subparallel to one another and perpendicular to the coastline. Gaps between caves along a linear trend represent zones of collapsed passage.



Figure 1-5. Freshwater pools in cave passages in Sistema Jaguar. Cave passage is partially inundated where the elevation of the cave floor is below the water table. Intermittent shallow pools occur <5 km inland **(A)** (photo: Isabel Grajales) and nearly continuous deeper pools occur ~6.5 km inland **(B)** (photo: Benjamin Schwartz).

Concentrated discharge from phreatic conduits (i.e. underwater caves) forms a series of coastal springs in bays known as caletas. No large underwater springs are observed along the beach in Paamul Bay, a sandy cusped beach on the coastline adjacent to Sistema Jaguar. Instead, many freshwater seeps can be observed in the sand and

shallow water of the bay. It is possible that a sediment-plugged conduit lies beneath Paamul Bay, or that large submarine springs exist beyond the reef.

1.2 Chapter Topics and Objectives

This research addresses the following gaps in the literature and challenges several long-held assumptions about the hydrogeologic history of the Yucatan Peninsula:

***Ch. 2 Objective:** Identify hydrogeologic controls on karstification.*

Structural and lithologic controls on speleogenesis have been inferred from the maze-like morphology and passage dimensions of underwater caves systems (Kambesis & Coke, 2016; Smart et al., 2006), but these data have not been systematically collected or statistically tested. Linear alignment of sinkholes and trends of closed depressions have been observed to coincide with regional fault zones and are hypothesized to influence the hydraulic gradient (Gondwe, 2010; Tulaczyk et al., 1993). Because karstification is a scale-dependent process, a detailed morphometric analysis of sinkholes and caves, utilizing both remote sensing and field observations, provides a means to more thoroughly investigate potential correlations between hydrogeologic controls and morphology. In Chapter 2, I examine the morphology, distribution, and alignment of sinkholes and cave passages, and relationships between the two, to identify patterns indicative of geologic or structural controls on speleogenesis.

***Chapter 3 Objective:** Quantify and constrain coastal karst aquifer properties.*

The modern aquifer system is thought to be driven by very low regional hydraulic gradients and drained primarily via conduit flow, with negligible contribution from matrix flow (Bauer-Gottwein et al., 2011). However, an increase in flow velocities near

the coastline suggests steepening of the gradient (Beddows, 2004) and ill-defined boundary conditions complicate efforts to establish a water budget and evaluate storage, transport, and discharge. Very low flow velocities observed in epiphreatic caves suggest high exchange between matrix and conduits. This research quantifies aquifer parameters through measurements of the gradient and changing water levels observed in epiphreatic caves. In Chapter 3, I identify, relate, and constrain aquifer parameters and variables that are needed to answer fundamental questions of how and where water is moving through the system, which provides a scientific foundation for potential aquifer models applicable to these coastal karst regions.

Chapter 4 Objective: Constrain the timing of conduit formation.

The Yucatan Peninsula is assumed to have remained tectonically stable for at least the past 120 ka (Szabo et al., 1978), and shallow caves are generally assumed to be <120 ka, with caves formed through geochemical processes occurring at or below sea level (Gulley et al., 2016b; Haukebo, 2014; Sanford & Konikow, 1989; Smart et al., 2006). Under an assumption of tectonic stability, cave elevations are expected to correspond with cumulative time at which sea level stands occurred over the past two million years (Gulley et al., 2016a; Kambesis, 2014; Smart et al., 2006), yet large and extensive caves lie at and above the modern water table, which is well above where the sea level has remained stable for the vast majority of the peninsula's geologic history. In a framework of changing sea levels over the past two million years, modern or recent hydrologic and geochemical conditions are inadequate to explain recent cave formation in their present location. Therefore, these shallow caves must either have 1) formed very rapidly during the brief sea level high stands during late Pleistocene interglacial periods, or 2) have

formed at lower elevations and since been lifted into their present location. A third contradiction in the assumption of tectonic stability is that measured and modeled rates of landscape denudation in tropical karst systems indicate that the land surface elevation should be much lower if no uplift has occurred. In Chapter 4, I use Uranium-Thorium (U-Th) dating methods to constrain the age of the caves, to refine Pleistocene sea level history in the Caribbean, and to challenge the prevailing paradigm of long-term regional tectonic stability.

Chapter 5 evaluates how well these objectives were met, poses questions for future research, and comments on the scientific and applied significance of this work as a whole.

2. SINKHOLE MORPHOLOGY AND DISTRIBUTION AS INDICATORS OF GEOLOGIC CONTROLS ON KARSTIFICATION AT A SUB-BASIN SCALE: QUINTANA ROO, MEXICO

Abstract

Geologic structures and properties control the orientation and extent of karstification, which in turn affects flow paths and hydraulic gradients. In areas where surface geology is not well exposed or easily accessible, inferences about local- to regional-scale hydrogeologic controls and insight into past conditions can be gained from morphological analysis of karst features using LiDAR-derived Digital Elevation Models (DEM) supported by field observations. We quantified and analyzed the morphology, distribution, and orientation of sinkholes and cave passages at a sub-basin scale in north eastern Quintana Roo, Mexico. Sinkhole morphology was similar across geologic units and consistent with regional-scale data. Higher sinkhole densities and clustering in Tertiary rock is consistent with a more mature karst landscape. Three dominant long-axis orientations were identified at 45°, 285°, and 345°, which suggest influence from the intersection of regional fault zones. Nearest Neighbor analysis identified trends in sinkhole alignment perpendicular and parallel to the coastline, and these are interpreted to represent flow paths along higher hydraulic gradient and along coastal deposits of higher permeability, respectively.

2.1 Introduction

Positive-feedback between discharge and conduit enlargement in karst systems means that the geometry and extent of caves are often controlled by structural and stratigraphic features and properties (Palmer, 1991). For example, direct mapping, numerical modeling, and fractal analysis in complex network-maze gypsum caves in the

Western Ukraine have shown that orientations of faults and joints control conduit formation (Andreychouk et al., 2013; Klimchouk & Andrejchuk, 2005; Rehrl et al., 2008). Similarly, sinkhole formation is influenced by a combination of geologic and hydrologic factors, and the manner and timing of the interaction between these factors determine where, when, and how an individual sinkhole may form (Doctor & Doctor, 2012). Sinkholes are often distributed in clusters or patterns that are related to structural and geologic features such as fractures, faults, or differences in lithology (Ford & Williams, 2007). In the Valley and Ridge province in Virginia, sinkhole distributions can be explained by concentrations of joints and fractures that locally increase permeability, and inclined carbonate strata bordered by aquitards or aquicludes that channel surface water and groundwater to and through carbonate rocks (Hubbard, 2001).

Morphometric analysis of karst features provides a basis for relating hydraulic properties to geomorphic characteristics, allowing inferences about aquifer history where data are otherwise scarce or uncertain. The common aim of a morphometric approach is to describe karst landforms and look for relationships between their distribution and density with any other factors, including geology, hydrology, and topography, or those related to anthropogenic influences (Brinkmann et al., 2008). These studies commonly use surface features such as sinkholes that are readily identified using topographic maps (Angel et al., 2004), or DEMs (Doctor & Young, 2013). In this study we assess sinkholes in a sub-basin area (100 km²) in the Yucatan Peninsula to infer information about structural and geologic influences on speleogenesis.

2.1.1 Geologic setting

The Yucatan peninsula is a carbonate platform that accumulated in shallow seas between 65 and 2 million years ago (Lopez, 1975). The oldest geologic formations are found in the interior of the peninsula, with progressively younger formations toward the coastline (**Figure 2-1**). Carbonate strata consist of Tertiary to Quaternary marine sequences of limestone, dolomite, and other sedimentary strata >1,500 m thick, below which lie Paleozoic quartz arenites (Ward et al., 1985). A PEMEX petroleum well drilled in western Quintana Roo encountered igneous basement rock at 2,390 m bmsl (Ward et al., 1985). Carbonates exposed at the surface range in age from Eocene at the center to Holocene sands along the coastline (Padilla-Sanchez, 2013). Strata are generally flat lying, resulting in a nearly level topography across the entire peninsula; elevations in the State of Quintana Roo are generally <30 m amsl, with local relief of 5 to 10 m (Ward et al., 1985).

Relatively few major structures are expressed on the surface of the Yucatan peninsula. The buried Chicxulub impact crater in the northwestern portion of the Peninsula has a series of deep pits around its southern rim, called the “Ring of Cenotes”, which are thought to be related to faulting in the outer slump of the crater (Connors et al., 1996). Cenote development is also likely influenced by depositional differences along the crater rim; Late Tertiary sedimentation was mostly restricted to the region within the buried crater, and a semicircular lagoon existed until at least Pliocene time (Pope et al., 1996). Three fault zones extend across the northeastern Yucatan Peninsula: The Catoche Fault Zone, the Rio Hondo Fault Zone, and the Holbox Fracture Zone. The Catoche Fault Zone is a system of NE trending normal faults that are mostly submarine across the Campeche Bank, but are also observed in the northern coastal plain of the peninsula.

The Rio Hondo Fault Zone is a series of normal faults that extends off-shore; Cozumel Island is interpreted as a horst block bounded by normal faults (Ward et al., 1985). The Holbox Fracture Zone is a zone of lineaments trending 5-10° that was initially identified by LANDSAT imagery (Ward et al., 1985) as extending 50 km southward from the northern shoreline, but has since been confirmed to extend as far as 120 km to Sian Ka'an Biosphere Reserve, south of Tulum ~ (20° N) (Gondwe, 2010).

The Holbox system is subparallel to a structural high in the Paleozoic basement called the Xcan Arch, identified by PEMEX drilling in the 1970's (Ward et al., 1985). Fracture sets in the Holbox fracture zone occur at orientations of 30-40° and 290-300°, but these fractures do not guide the regional orientation of lineaments that define the zone at 5-10° (Ward et al., 1985). The alignment of elongate solution depressions is parallel to offshore tectonic features (Tulaczyk, 1993; Southworth, 1985). Tulaczyk (1993) proposed a hydrogeologic model in which collapsed and buried karst features provide pre-existing pathways for groundwater flow, and thereby influence flow in shallower layers. Caves in the study area appear to have some structural control based on visual observations of linear passage orientations, but no data have been collected to test this statistically.

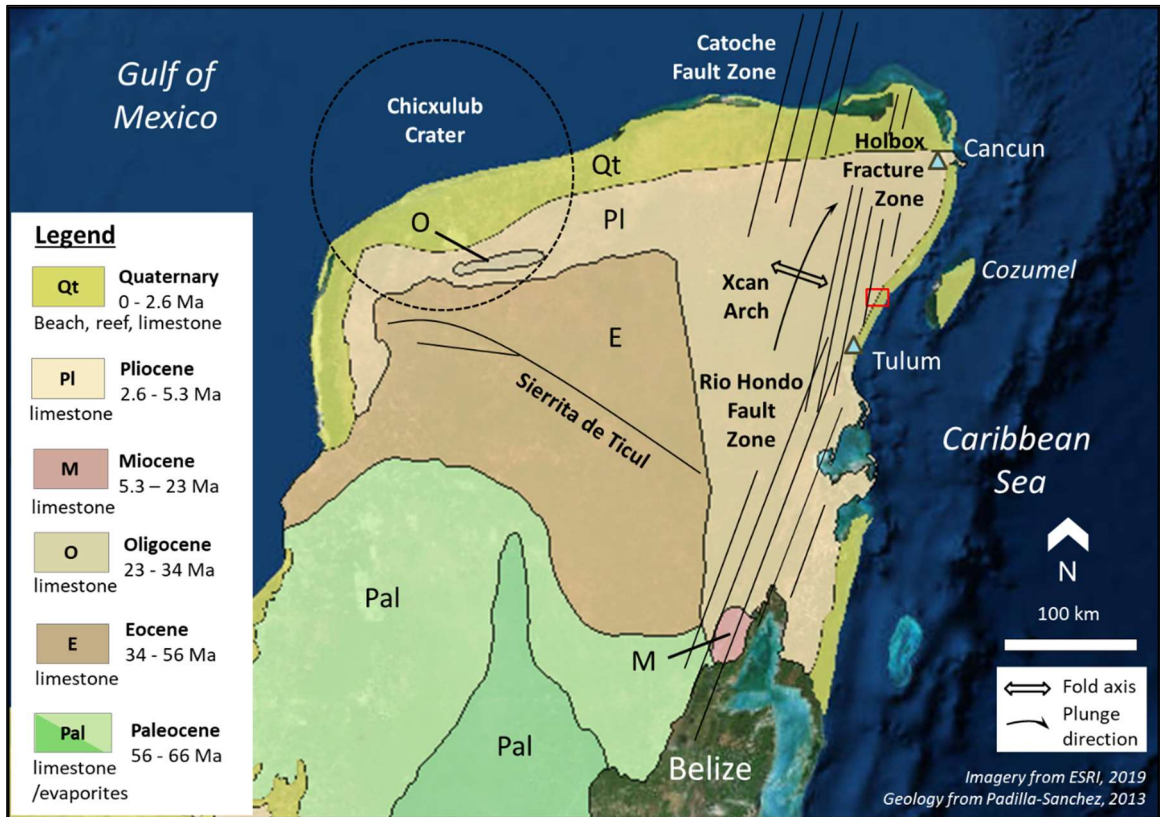


Figure 2-1. Simplified geologic map of the Yucatan Peninsula. Regional structural features relevant to this research are annotated. The red box outlines the study area.

2.1.2 Study area

The study area is located approximately 70 km south of Cancun (**Figure 2-2**) and contains numerous epiphreatic caves (i.e., intercepting the modern water table), most of which are within 10 km of the coast. This distance is likely a result of sampling bias rather than a lack of inland cave systems (Gondwe et al., 2010; Smart et al., 2006; Beddows, 2004), as it reflects vicinity to population centers and the effort required to traverse dense vegetation. Epiphreatic caves are characterized by horizontally extensive, maze-like networks that converge inland and are often oriented perpendicular to the coastline. Passages are very shallow, often only a few meters below the surface, and collapses of the thin ceiling create numerous circular entrances. Phreatic caves in this

area are sometimes connected with caves at and above the water table, and these generally have similar morphology to epiphreatic caves (Kambesis, 2014). It is thought that epiphreatic caves formed in the same manner as phreatic caves, but have since been drained by a drop in sea level relative to their time of formation (Kambesis & Coke, 2013; Smart et al., 2006).

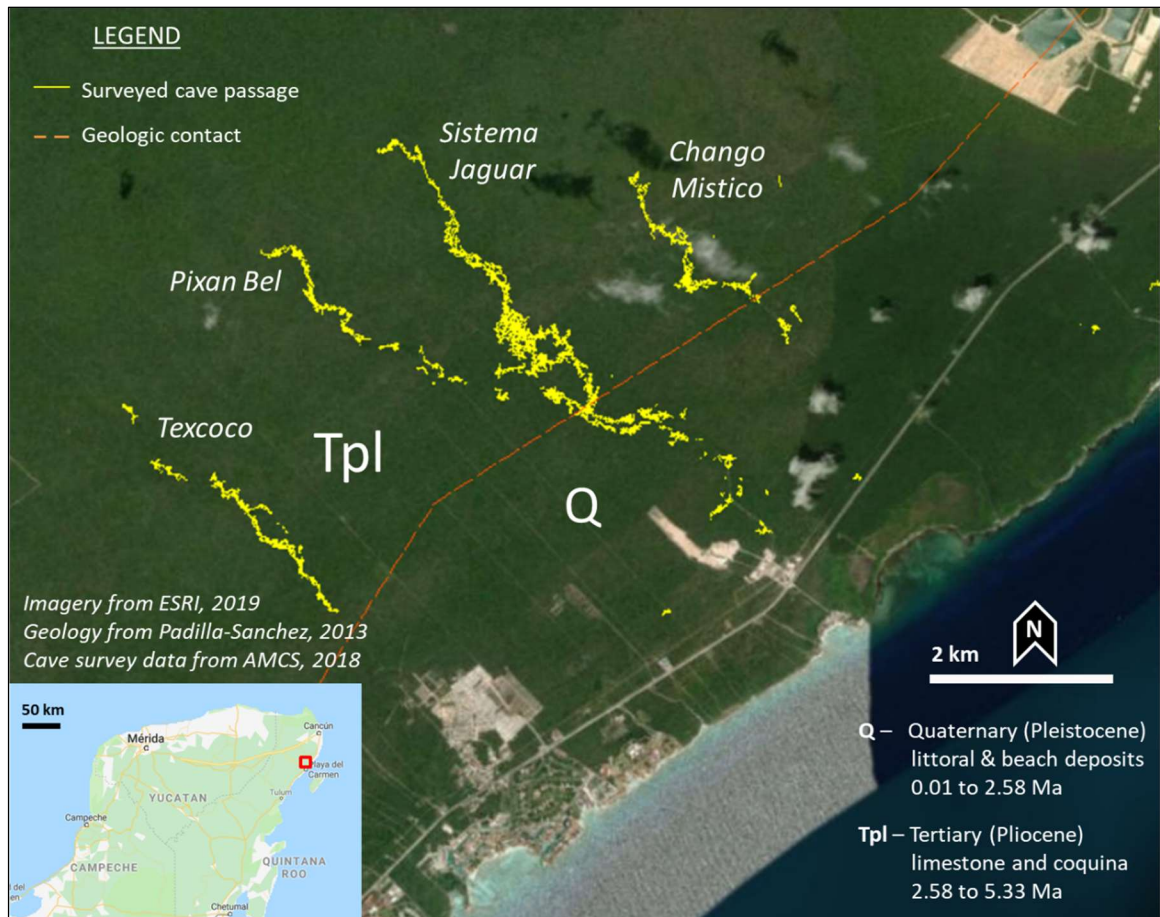


Figure 2-2. Aerial photo of the study area. Surveyed epiphreatic cave passage is indicated by the solid yellow lines, and an approximate geologic contact (from Padilla-Sanchez, 2013) is shown as a dashed orange line 3-4 km parallel to the coastline.

Poorly expressed structural features and indistinct geologic contacts, as well as generally level topography, make field assessments of karst features difficult. However, analysis of shape, orientation, and distribution of many karst features can provide insight into potential lithologic and/or structural controls on regional hydrology and speleogenesis that are otherwise unrecognizable on the surface. The objective of this study is to perform a spatial statistical analysis of karst depressions using a combination of LiDAR-derived data and traditional field survey techniques to address two research questions: 1) Are differences in sinkhole distribution, size, or shape related to recognized geologic differences? and 2) Is orientation or alignment of sinkholes and other karst features related to known regional structural trends?

2.2 Methods

We used both a LiDAR-derived DEM and field data to perform sinkhole morphology and distribution analyses. LiDAR-derived DEM analysis is the preferred method when high-resolution data is available, although any automated method requires critical evaluation to ensure that it produces meaningful results. Field data can also be used to ground-truth automated results, and a large dataset of documented cave entrances was also referenced for this research. However, cave entrances are a human-sized subset of all existing karst features, and available data are limited to documented sinkholes in areas that have been physically explored. As a result, known entrances are generally restricted to those that formed by collapse into a mapped cave passage. Systematic sampling methods were used in field studies to reduce bias and provide geologic context. Patterns of sinkhole orientation and alignment were compared with linear trends in cave passages that were identified by drawing bounding rectangles around sections from cave

survey data at 1:10,000 scale in ArcMap 10.6 and plotted using GeoRose 0.4.3 (Yong Technology Inc., 2014).

Table 2-1. A comparison of methods for sinkhole identification and analysis.

DEM Analysis	Cave Entrance Data	Line-intercept Survey
+ A large amount of data is available, and quality is improving	+ Information is available, collected by volunteers	+ Informed by field observations
+ Can be performed across a range of scales	- Selective of human-sized voids formed by collapse	+ Unbiased when done correctly
- Process dependant; may contain artifacts or misleading data	- Biased by the limits of exploration	- Difficult and time consuming

2.2.1 LiDAR-derived DEM analysis

GIS analyses used ArcMap 10.6 and a LiDAR derived DEM with 5 m horizontal and 1 m vertical resolution (INEGI, 2017). The fill tool was applied to the DEM raster of the study area to create a depressionless topographic surface and the original raster was subtracted to identify depressions. The resulting raster was converted to a polygon layer following the pixel outlines of cells with similar values. Concentric feature boundaries were dissolved to generate an outline of each depression. Bounding polygons were generated around each outline, and the centroid coordinates were extracted to a new point layer. The maximum depth value was extracted from the underlying raster using the Zonal Statistics tool. All depressions <2 m deep were removed due to the large number of artifacts at this scale. Morphometric analyses utilized the processed polygon layer, and spatial statistics used the centroid point layer.

2.2.1.1 Morphometrics and Orientation.

Geometric attributes of depth, area, perimeter, length, and width were calculated for each polygon, and these were used to calculate morphometric indices of shape. Shape can be measured in many different ways, and using at least two different metrics provides more robust results (Zhu & Pierskalla, 2016). Four morphometric indices used in this research are described below and summarized in **Figure 2-3**:

Circularity, also called the *Gravelius coefficient* used to characterize water sheds (Bendjoudi & Hubert, 2002), is a measure of the difference between the perimeters of a polygon P and a perfect circle with the same area A :

$$[2.1] \quad Ci = \frac{P}{2\sqrt{\pi A}}$$

This value will tend to one when the object is most similar to a circle, and will deviate from one when the object has a more irregular shape (Fragoso-Servón et al., 2014).

Compactness is measure of the area that a polygon occupies within an enclosing circle with an area A and perimeter P (Davis, 2002):

$$[2.2] \quad Cp = \frac{4\pi A}{P^2}$$

Elongation is the ratio of width w to length l of the fitted minimum bounding rectangle of a polygon (Wu et al., 2016):

$$[2.3] \quad El = \frac{w}{l}$$

Eccentricity is a measure of the elongation of a depression compared to an enclosing circle, where l and w are the lengths of the long and short axis, respectively (Doctor & Young, 2013):

$$[2.4] \quad Ec = \sqrt{1 - \frac{w^2}{l^2}}$$

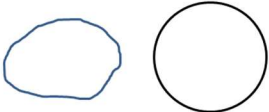
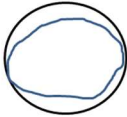
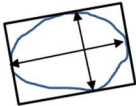
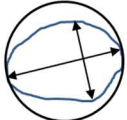
<p style="text-align: center;">Circularity (Grevalius's coefficient)</p> $Ci = \frac{P}{2\sqrt{\pi A}}$  <p>The ratio of perimeter between a polygon and a perfect circle of equivalent area A</p>	<p style="text-align: center;">Compactness</p> $Cp = \frac{4\pi A}{P^2}$  <p>The area that a polygon occupies within an enclosing circle of area A and perimeter P</p>
<p style="text-align: center;">Elongation</p> $El = \frac{w}{l}$  <p>The ratio of the short axis (w) to the long axis (l) of a minimum bounding rectangle</p>	<p style="text-align: center;">Eccentricity</p> $Ec = \sqrt{1 - \frac{w^2}{l^2}}$  <p>The ratio of elongation compared to that of an enclosing circle</p>

Figure 2-3. Morphometric parameters describing depression shape.

The orientations of depressions were measured in GIS as the azimuth θ of the long axis relative to north (**Figure 2-4**).

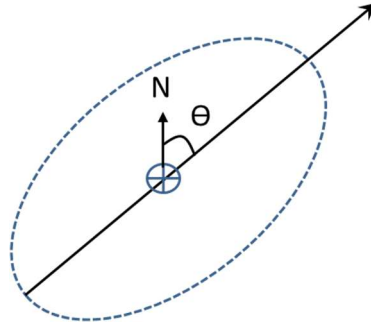


Figure 2-4. Diagram of depression orientation measurement.

Morphometric data was compared in R using the non-parametric Kruskal-Wallis test by ranks (Kruskal & Wallis, 1952), which may be used between sample sets of different sizes with a minimum sample size of five. The test statistic H is given by:

$$[2.5] \quad H = \frac{[(N-1) \sum_{i=1}^g (n(r(i) - \mu(i))^2)]}{\sum_{i=1}^g (r(ij) - \mu)^2}$$

Where N is the number of all observations across groups, n is the number of samples in group i, r(i) is the average rank of all samples in group I, $\mu(i)$ is the mean of all samples in group i, r (ij) is the average rank of a sample in groups i and j, and μ is the mean of all samples across groups.

2.2.1.2 Distribution and alignment.

The following spatial statistic tests were applied to describe the spatial distribution and density of depressions within the study area:

Nearest Neighbor Analysis (NNA) is a statistical test used to evaluate whether a data set is clustered, dispersed, or randomly distributed, based on the average distance

between points. NNA was applied to identify clustering of depressions in relation to the distances between their respective centroids, and this was done from the first through the ninth nearest neighbor to detect differences in clustering by scale. Similarly, the *Direction to Nearest Neighbor (DNN)* can also reveal patterns of depression alignment across scales. DNN was applied from the first through the ninth nearest neighbor.

Ripley's K function evaluates the distribution of a set of points across a range of scales. This statistical approach compares expected density assuming random distribution to observed density within an expanding radius around an arbitrarily chosen point. Density is iteratively recalculated at increasing distances, and the difference between expected and random results is a metric of clustering or dispersion. Higher than expected values indicate clustering and lower than expected values indicate dispersion. The maximum positive difference corresponds to the distance at which clustering is greatest. All distributions appear dispersed at a sufficiently great scale, and this threshold is identified by where the difference becomes negative. Ripley's K function is:

$$[2.6] \quad L(d) = \frac{\sqrt{K(d)}}{\pi}$$

Where $K(d)$ is the expected number of points within a distance d of an arbitrary point assuming random distribution. $L(d)$ is recalculated iteratively at least nine times and averaged for a single date set. Ripley's K was used to identify the maximum clustering distance, and this value was used as the search radius for kernel density mapping.

Kernel Density Mapping (KDM) is a technique used to identify areas of high point density. The radius of highest clustering identified by Ripley's K analysis is used as a

range around each point to calculate point density at that location. The resulting value is assigned to a cell in a raster to produce a visual representation of point distribution across a surface. KDM was used to identify clusters of depression centroids.

Moran's I (Spatial Autocorrelation) is a measure of spatial distribution of attributes within a data set. Given a set of features and an associated attribute value, it evaluates whether the pattern expressed is clustered, dispersed, or random. A local z-score can also be calculated at each point based on the similarities to its neighbors, and areas of clustering can be mapped according to their statistical significance (Anselin Local Moran's I). Moran's I was applied to determine if clustering was present by orientation, and Anselin Local Moran's I was applied to identify areas where sinkholes with similar orientations are significantly clustered.

Alignment of depressions was measured in ArcMap 10.6 as the azimuth θ between centroids relative to north (**Figure 2-5**). Distance and direction to the 1st through 9th nearest neighbors were obtained using the Near Table tool.

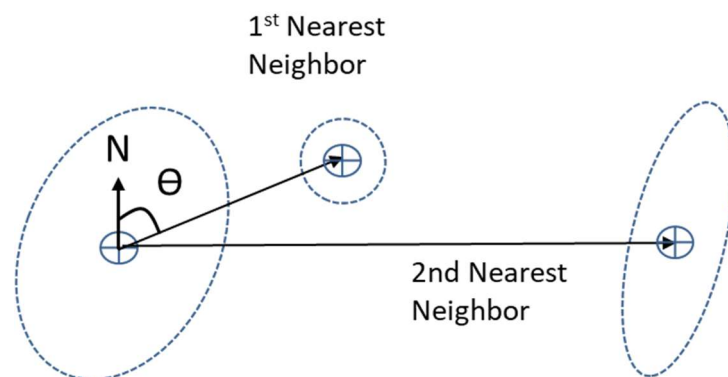


Figure 2-5. Diagram of depression alignment measurement.

2.2.2 Cave entrance data

Entrance location coordinates were recorded by volunteers using a hand-held GPS (Garmin ± 2 m horizontal) (AMCS, 2014). The point layer of entrance coordinates was overlain on the DEM and a 10 x 10 km grid net was generated to provide cells for systematic sampling (cell size = 1 km²). A Kruskal-Wallis test was used to test for differences in the point density of cave entrances between Quaternary (Q) and Tertiary (T_{pl}) geologic units.

Cave entrance data were analyzed for access bias using a cost-map raster that contains cell values weighted according to the relative difficulty of moving to a point. The study area for this portion of the project was expanded to include all available data of documented cave entrances. The DEM for the area containing these data was bounded by a 140 km x 70 km (9,800 km²) rectangle parallel to the coastline and clipped to match the shoreline and inland political boundary of Quintana Roo, Mexico. The cost map was generated using a weighted overlay that accounted for factors affecting cave access, including: (1) slope, (2) vegetation cover, and (3) proximity to roads. Access according to landownership was considered but disregarded because landowners in the study area were agreeable to exploration that might lead to development of ecotourism in caves on their property. Slope was generated from the DEM raster and reclassified in 1 to 3 intervals of from zero to a maximum of 30% grade. Vegetation was reclassified from 1 to 3 according to type and in order of increasing impedance to access. Class 1 contains land zoned as urban, human settlement or devoid of vegetation. Class 2 contains agricultural land, including seasonal agriculture and coastal dunes. Class 3 contains various types of tropical forest, secondary growth, and mangroves. Proximity to roads was calculated

using Euclidean distance and classified into bands of 1 to 3 km from the nearest road. Slope, vegetation, and road distance were weighted equally at 33% and cell values were added to generate the final weighted-overlay raster.

Buffers were generated at 0.5 km intervals around roads and an average entrance density was calculated within each zone. Average densities were used rather than a density gradient because cave distribution is highly clustered. Densities from similar distance intervals were compared across geologic units to evaluate differences between older limestone formations inland and younger formations along the coast. This was accomplished by creating polygon layers of individual geologic units and then selecting entrance locations within them.

2.2.3 Line-intercept field surveys

Sinkhole surveys were performed using the line-intercept method, a sampling technique first developed in forestry to estimate the number of trees remaining after logging (Warren & Olsen, 1964), and later applied in ecology to estimate the populations of plant species or sessile animals (Gillison & Brewer, 1985). In line-intercept surveys, a sample is counted if a predetermined line (transect) crosses its location (Kaiser, 1983). Four transects were drawn in ArcGIS at approximately equidistant spacing of 1.5 km, starting at points where the surface was known to be accessible via cave entrances. Each transect extended 1 km from and roughly perpendicular to the cave, parallel to the coastline (60°), with 30 m long sub-transects every 100 m at alternating directions perpendicular to the main transect (150° and 330°) (**Figure 2-6**). Karst features were documented if they met the following criteria: 1) within 10 m of the sub-transect line 2) have a vertical relief of at least 1 m, and/or 3) have a visible drain or cave entrance.

Depression dimensions, long-axis orientations, and locations were documented using the ArcGIS Collector application for Android phones (Samsung Galaxy 9, ± 3 m accuracy). Examples of typical features are shown in **Figure 2-7**.

A Kruskal-Wallis test (Equation 2-5) was used to identify any significant difference exists in the average number of sinkholes per line compared across all transects. A post-hoc Dunn's test of multiple comparisons (Dunn, 1964) was applied to identify which transects are significantly different from one another. This test uses the average rankings from the prior Kruskal-Wallis test to compare the mean rankings in each group. The R package `dunn.test` (Dinno, 2017) was used for this analysis.

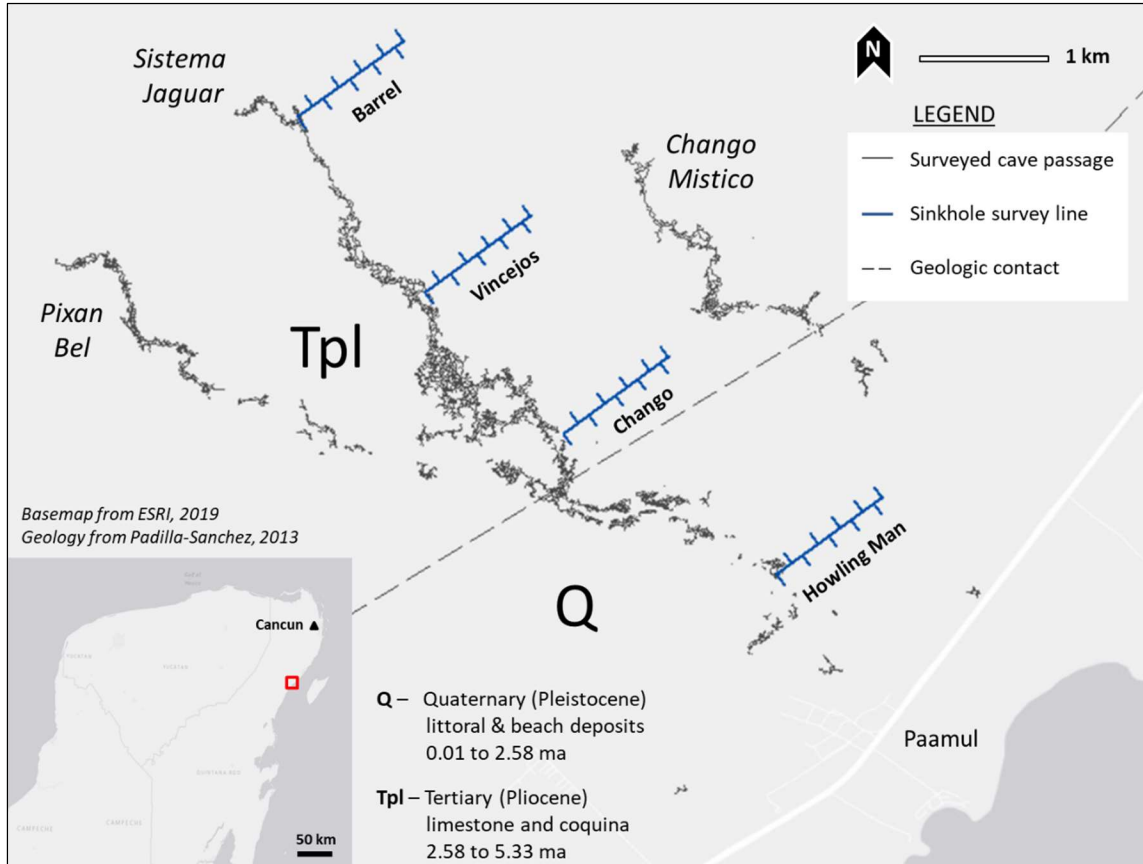


Figure 2-6. Map of sinkhole survey transects. Each transect extends for 1-km parallel to the coastline. Inset shows the location of the study site approximately 70 km south of Cancun.



Figure 2-7. Examples of sinkholes documented in a line-intercept survey. Common morphologies included closed depressions (A) and cylindrical shafts (B). The closed depression shown is approximately 2 m in diameter and 1 m deep. The tape next to the cylindrical shaft is extended 30 cm.

2.3 Results

2.3.1 LiDAR- derived DEM analysis

2.3.1.1 Morphometrics and orientation

GIS processing of the DEM identified 2,005 depressions with a minimum area of 25 m² and a minimum depth of 2 m (Figure 2-8). Frequency distributions of length, width, and depths of all depression are shown in Figure 2-9. Frequencies were categorized by increments of 5 m up to a maximum length of 870 m and width of 1,224 m. An outlier that appears in both length and width plots is an unusually large shallow (2-5 m deep) depression to the north of Chango Mistico (Figure 2-8). This was removed from calculations of summary statistics of geometric attributes, which are compared across geologic units in Table 2-2.

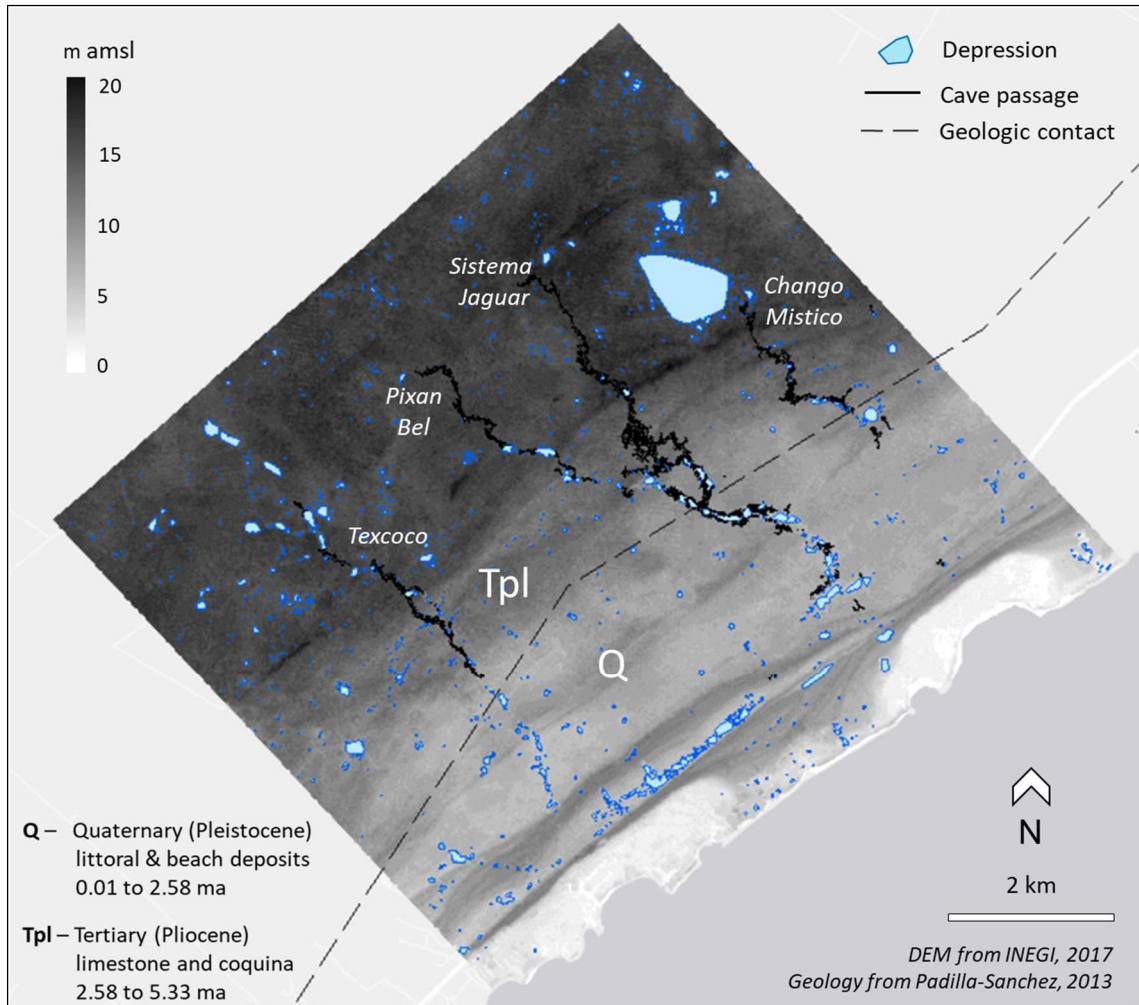


Figure 2-8. Processed DEM with depressions of at least 2 m depth. Depressions are shown by polygons in blue ($n=2,005$). Surveyed cave passage is shown by the solid black lines. The geologic contact between younger (Q) and older (Tpl) rock units, represented by the dashed line, occurs 2-4 km inland subparallel to the coast (Padilla-Sanchez, 2013).

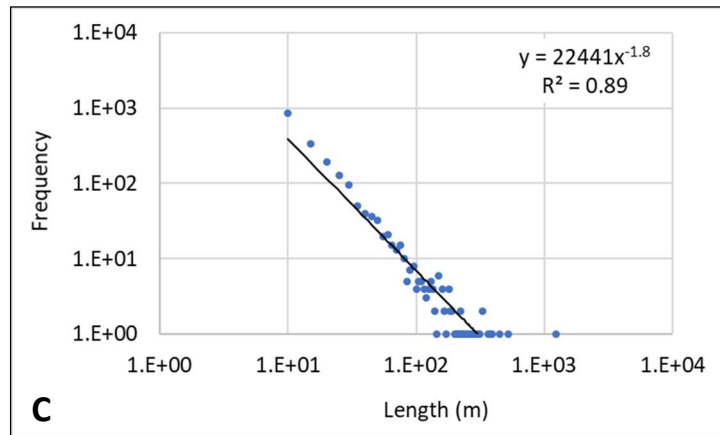
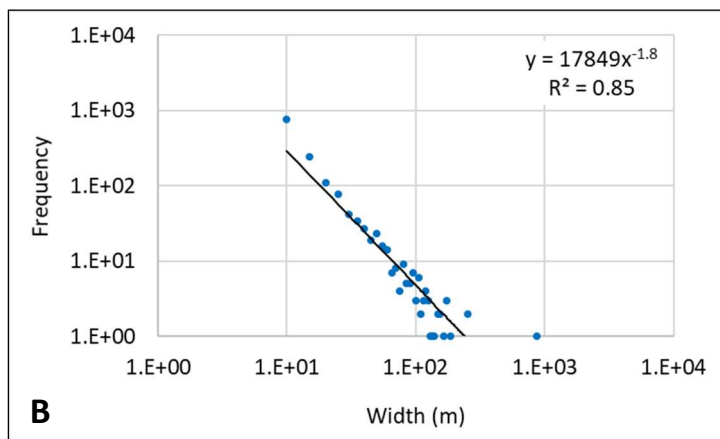
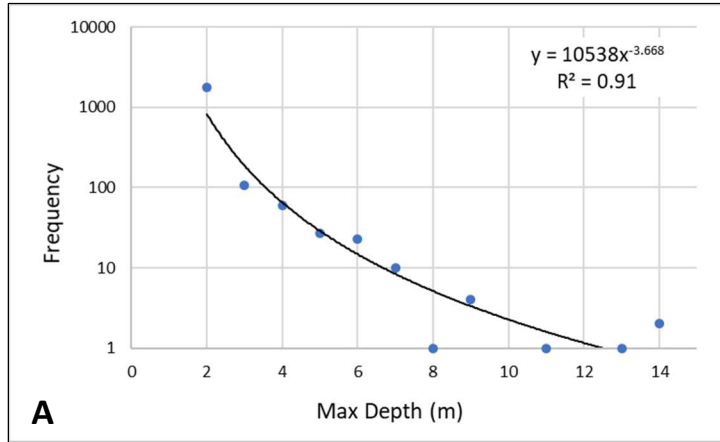


Figure 2-9. Frequency distributions of depression size. The depth (A), width (B), and length (C) of all depressions (n= 2,005) display power distributions.

Table 2-2. Summary statistics of depression geometry. Average values of each metric are compared across each geologic unit using the Kruskal-Wallis χ^2 test. (Q: n= 599; Tpl: n= 1,406)

	Quaternary (Q)				
	Depth (m)	Perimeter (m)	Area (m ²)	Length (m)	Width (m)
<i>Ave</i>	2	74	801	25	16
<i>Max</i>	7	1,512	43,254	520	255
<i>Min</i>	2	19	16	5	5
<i>Std. dev</i>	1	122	3,314	41	22
	Tertiary (Tpl)				
	Depth (m)	Perimeter (m)	Area (m ²)	Length (m)	Width (m)
<i>Ave</i>	2	67	773	24	15
<i>Max</i>	14	1131	58,042	444	251
<i>Min</i>	2	19	16	5	5
<i>Std. dev</i>	1	148	19,782	51	31
χ^2	11.716	2.699	2.628	2.027	4.318
P, df=1	0.001	0.101	0.105	0.155	0.038

Sinkhole shape is described by the four morphometric parameters calculated from the geometric attributes (**Figure 2-10**). Differences between these parameters according to geologic unit are presented in **Table 2-3**. A Kruskal-Wallis χ^2 test detected no significant difference in depression shape between the geologic units. The orientations of all depressions displayed three dominant trends at 45 to 50°, 285 to 290°, and 340 to 345° (**Figure 2-11**).

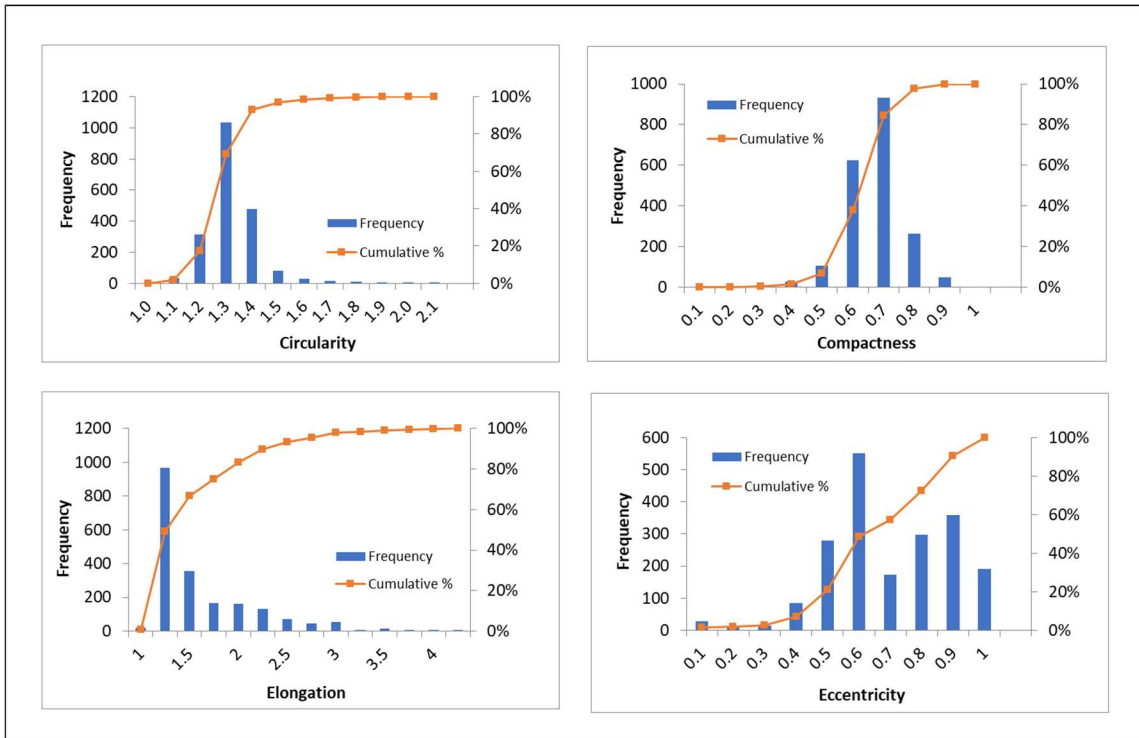


Figure 2-10. Frequency distributions of depression morphology.

Table 2-3. Mean morphometric parameters compared across geologic units.

	Circularity	Compactness	Elongation	Eccentricity
Q	1.28	0.61	1.51	0.64
Tpl	1.30	0.60	1.52	0.64
χ^2	2.91	3.27	0.06	0.0002
P, df=1	0.09	0.07	0.81	0.99

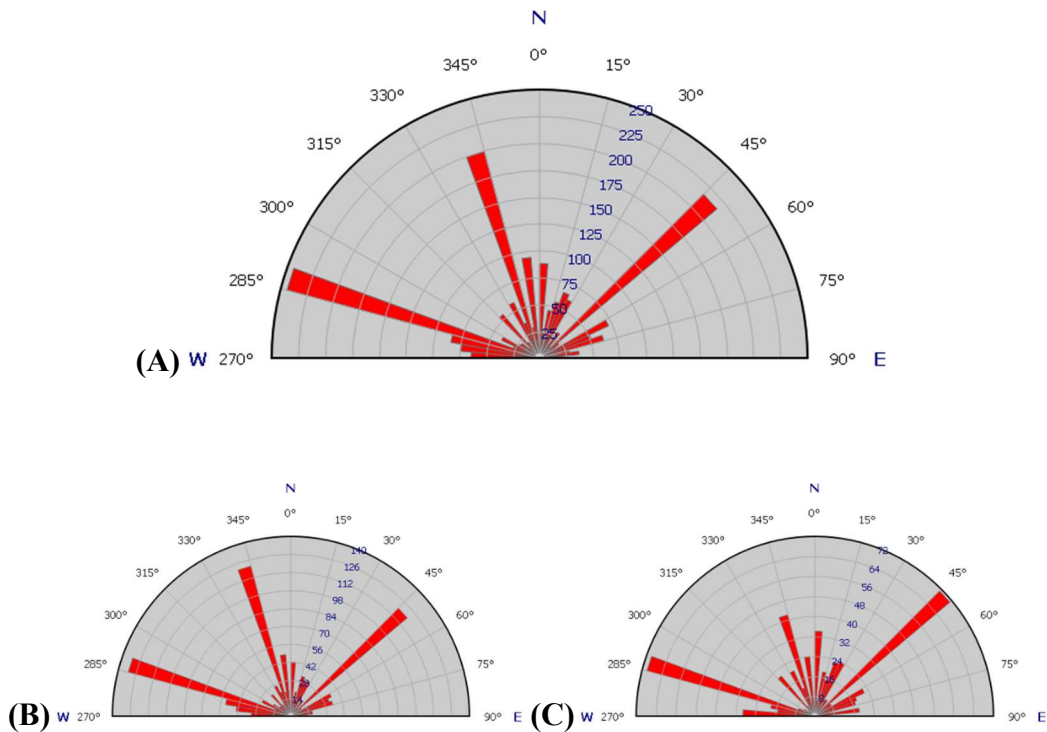


Figure 2-11. Orientations of depressions identified in the DEM. Frequencies of the long-axis azimuths of depressions >2 m depth in the entire study area (n= 2,005) **(A)**, in Tertiary-age rock (n= 1,406) **(B)**, and in Quaternary-age rock (n= 599) **(C)**.

2.3.1.2 Distribution and alignment

The DEM of the study area was overlain with a 10 x 10 km grid of 1-km² cells for systematic sampling and to compare point density between geologic units (**Figure 2-12**). Six cells along the coastline containing only water and beach sediments were removed from analysis. Point density within the older (Tertiary) rock unit (n= 54 cells) is 26 depressions/km², and point density within the younger coastal rock unit (n= 41 cells) is 15 depressions/km². A Kruskal-Wallis χ^2 test revealed a significant difference in depression density between the Q and Tpl geologic units ($\chi^2= 11.6$, df= 1, p= 0.0006).

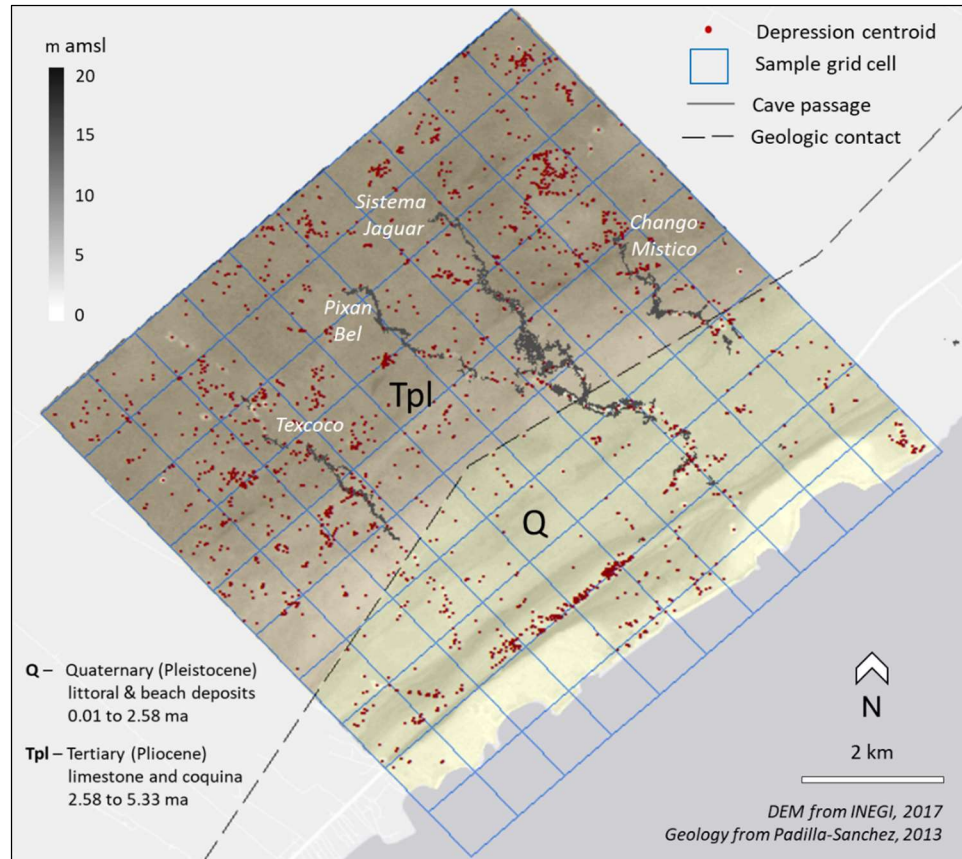


Figure 2-12. Point density of depression centroids. A sampling grid of 1-km² cells (blue lines) was overlain to statistically compare point densities of depressions identified in the DEM across geologic units.

Euclidean distances to the first nearest neighbor were calculated for all centroids, and the degree of clustering was compared to a random set of points generated within an equal area. Points near the study area boundary potentially have nearest neighbors that lie outside of the data set, producing an error called “edge effects”. Points with a distance to site boundary less than the distance to the 1st nearest neighbor were removed (n= 34) to correct for edge effects. This process is repeated for each iteration of nearest neighbor analysis and for any other boundaries within the study area such as geologic units. In cases where point location is provided by reporting or drilling, it is advised to also remove points in areas that have not been thoroughly explored or described and may have

nearest neighbors not included in the data set (Gao et al., 2012). Because all depressions in the study area were identified by the same automated method, no points were removed for this criterion.

Using an average Nearest Neighbor Analysis of the entire study area (~92 km²) the observed mean distance is 58 m, with an expected mean distance of 108 m between random points, resulting in a Nearest Neighbor Ratio of 0.53 ($z = -39.5$; $p < 0.0001$), which indicates a pattern of clustering (**Figure 2-13**). Nearest neighbor distances display lognormal distributions (**Figure 2-14**).

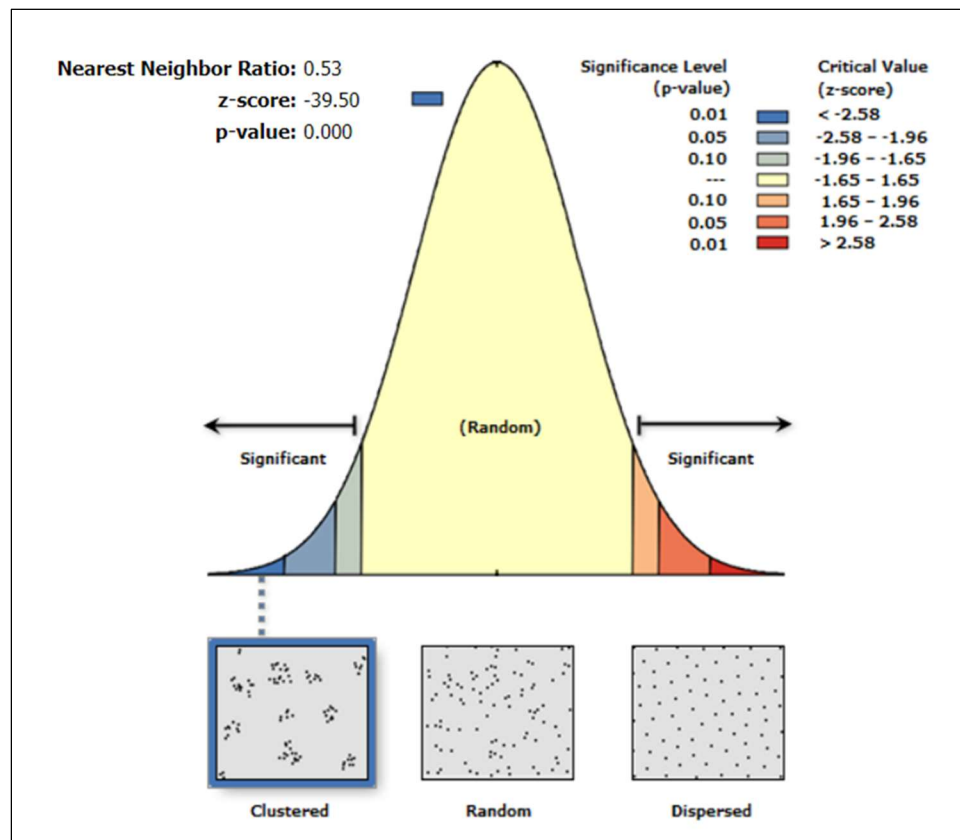


Figure 2-13. Nearest Neighbor statistic for all centroids.

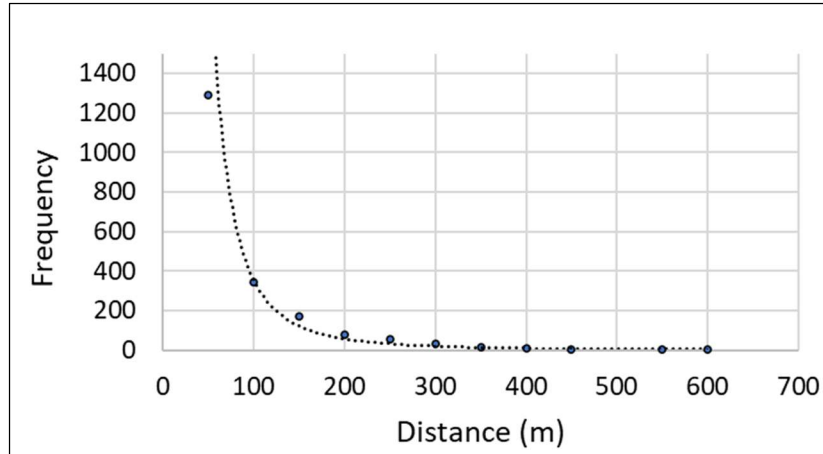


Figure 2-14. A frequency plot of 1st Nearest Neighbor distances. Distances are plotted in 50 m increments. (n= 1,971).

The 1st Nearest Neighbor Analysis was repeated within geologic units, with edge effect corrections applied and removing ten additional points along the geologic contact. In the coastal Quaternary-age rock (~35 km², n = 580), the observed mean distance between centroids was 59 m compared to an expected distance of 122 m, with an NNR of 0.48 (z = -24; p = <0.0001). In the inland Tertiary-age rock (~57 km², n = 1,372) the mean observed distance was 57 m compared to an expected distance of 101 m, with an NNR of 0.57 (z = -31, p = <0.0001). Average nearest neighbor distances calculated from the 1st through the 9th Nearest Neighbor demonstrate similar trends for each geologic unit across scales from a distance of 38 m (1st NN) to 262 m (9th NN) (**Figure 2-15**). Plots comparing the cumulative probability distribution of observed distances to an expected log normal distribution of distances between random points (P-P) plots are useful for demonstrating transitions between clustered and dispersed patterns. P-P plots of the 1st through 9th nearest neighbors showed that depressions are more highly clustered at smaller scales, and dispersion occurs beyond the 3rd nearest neighbor (**Appendix A**).

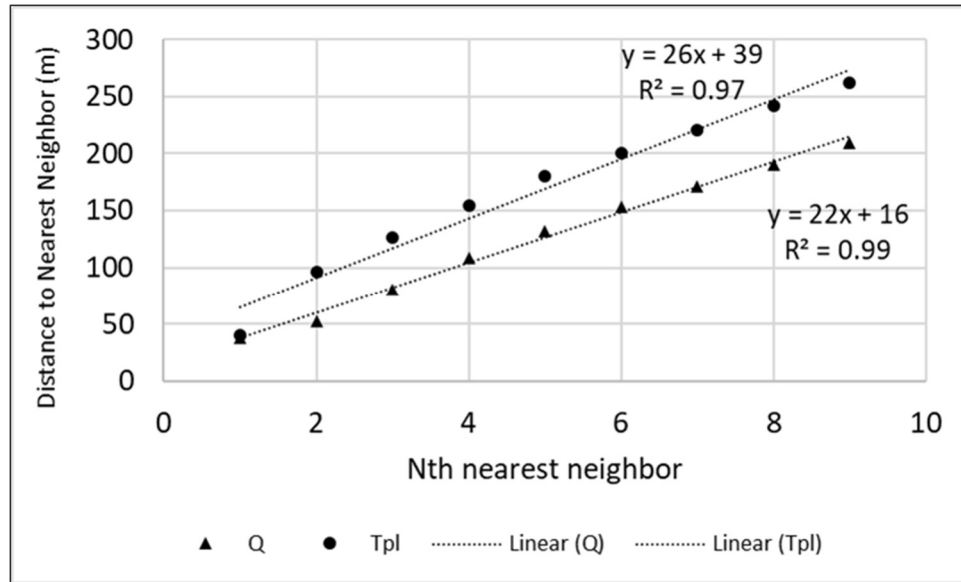


Figure 2-15. Distance to 9th Nearest Neighbor by geologic unit.

The Direction to Nearest Neighbor was calculated as an azimuth from a centroid to the centroid of its first nearest neighbor. This analysis revealed two trends in sinkhole alignment across the study area at 45-50° and at 315-342° (**Figure 2-16**). The same dominant trends in alignment appeared in both geologic units. Analysis was repeated through the 9th nearest neighbor to evaluate changes across scales. Directional data from all nine nearest neighbor distances are provided as rose plots in **Appendix A**.

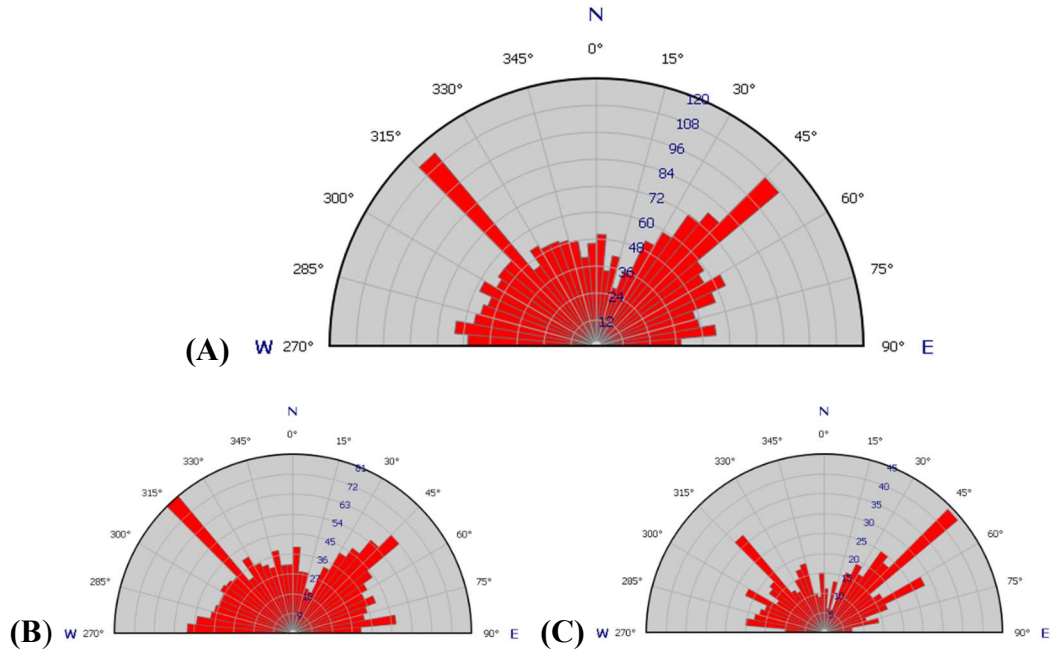


Figure 2-16. Direction to 1st Nearest Neighbor rose plots. Azimuths of direction to nearest neighbors is shown for all centroids n= 1,971 (A), centroids in Tertiary rock n= 1,372 (B), and in Quaternary rock, n= 580 (C).

Ripley's K statistic identified maximum clustering at a 380 m search radius (Figure 2-17). A kernel density map using this search radius shows hot spots parallel to the coastline and to the northeast of the terminus of cave systems (Figure 2-18).

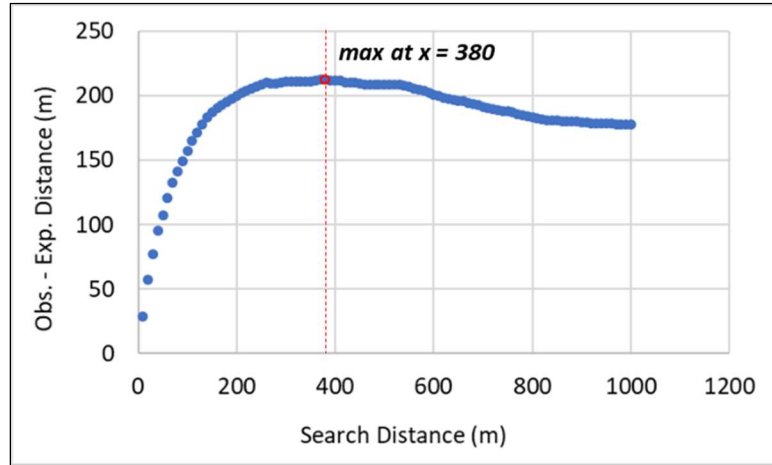


Figure 2-17. Results of Ripley's K function. Clustering plateaued between 250 and 500 m, and peaked at 380 m.

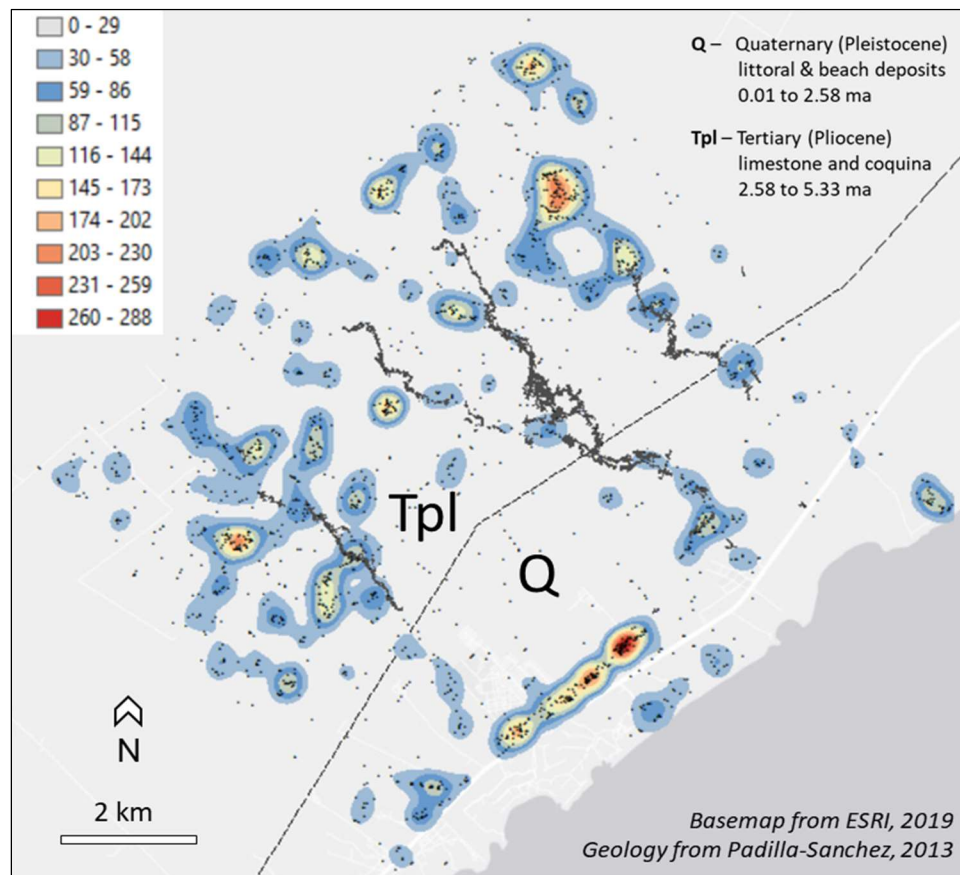


Figure 2-18. Kernel Density Map with a search radius of 380 m.

In addition to geographic clustering, patterns of attribute distribution were evaluated for depth, area, and orientation using Moran's I. Of these, only the orientation of the long axis of depressions demonstrates significant clustering ($I = 0.038$, $z = 3.8$, $p < 0.0001$). The similarity of neighbors surrounding each clustered point was evaluated using Anselin Local Moran's I (**Figure 2-19**). The significance of each cluster is identified as follows: a cluster of high values (High-High), a cluster of low values (Low-Low), outlier in which a high value is surrounded primarily by low values (High-Low), and outlier in which a low value is surrounded primarily by high values (Low-High). High value clusters occur at 343- 344°, and low value clusters at 11°- 19°.

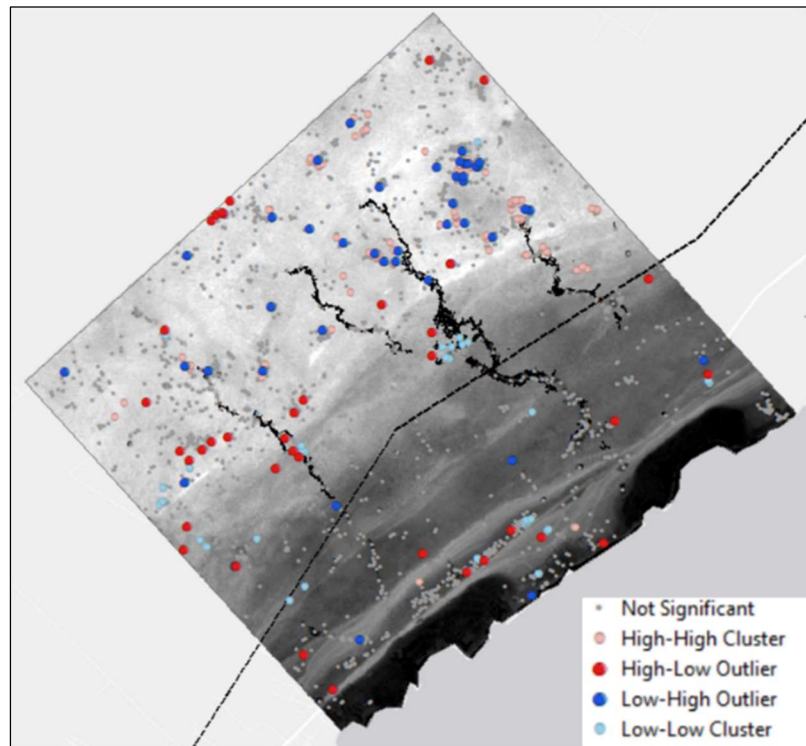


Figure 2-19. Clustering identified by Anselin Local Moran's I.

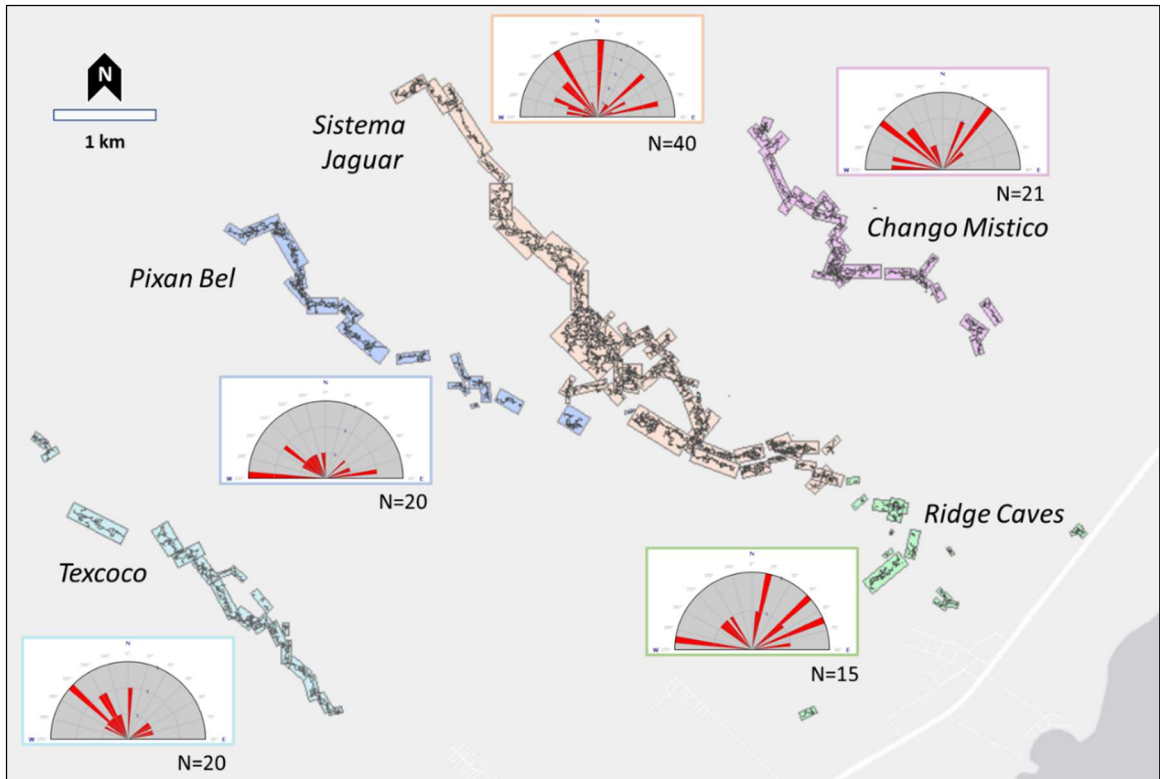


Figure 2-20. Linear trends of cave passage. Trends were measured from the long-axis orientation of bounding boxes drawn at 1:10,000 scale.

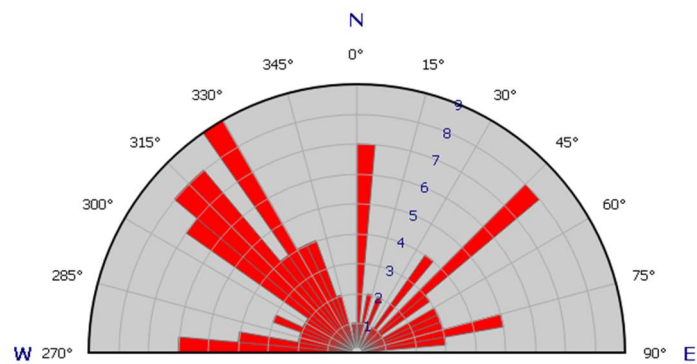


Figure 2-21. Linear trends of all cave passage as defined by bounding boxes. (n= 116).

2.3.2 Cave entrance data

The point density of cave entrances is higher in sampling grid cells over Quaternary age rock compared to Tertiary age rock (**Figure 2-22**). Cells over the Quaternary unit (n= 41) have an average point density of 6 cave entrances per km², while those over the Tertiary unit (n= 54) contain an average of 1 cave entrance per km². A Kruskal-Wallis χ^2 test found a significant difference in the point density between geologic units ($\chi^2= 19.8$, df= 1, p <0.0000).

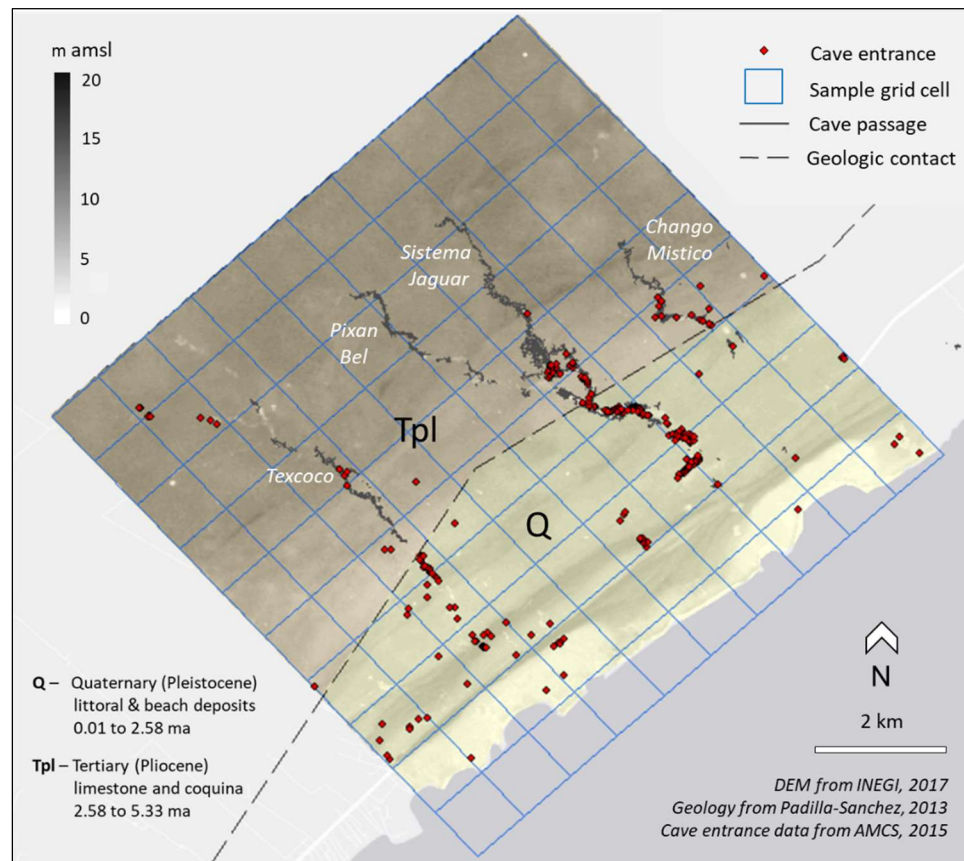


Figure 2-22. Point density comparisons in a 10 x 10 km sampling grid. The point density distribution of known cave entrance locations (red dots) was compared across mapped geologic units. The 1-km² sampling grid outlined in red was used for comparison of point density. Cells over water and beach sediments containing no points were removed from analysis.

Access bias was evaluated using the total available data set of cave entrances, rather than the 10 x 10 study area used elsewhere in this work, in order to include additional roads. A cost map with all factors weighted evenly is overwhelmingly uniform around distance from roads, which is consistent with knowledge that slope varies little across the study area, and that vegetation is generally either jungle or cleared. This visually demonstrates that of the factors considered, distance from roads presents the strongest control in entrance accessibility. A near-distance table was generated to report the straight-line distance between each cave entrance in the study area and the nearest known road. The first kilometer interval contains 1,315 entrances, or about 68% of the total data set and the number of cave entrances decreases with each additional kilometer from the nearest road.

Cave entrance densities were calculated using the area of each kilometer interval zone as obtained from the attribute table and the number of entrances within that layer selected by location. This process was repeated to obtain finer resolution within the 1 km zone using buffer intervals of 0.25 km out to 1 km and then 0.5 km out to 2.5 km. Cave entrance density per square kilometer decreases geometrically with increasing distance from roads (**Figure 2-23**).

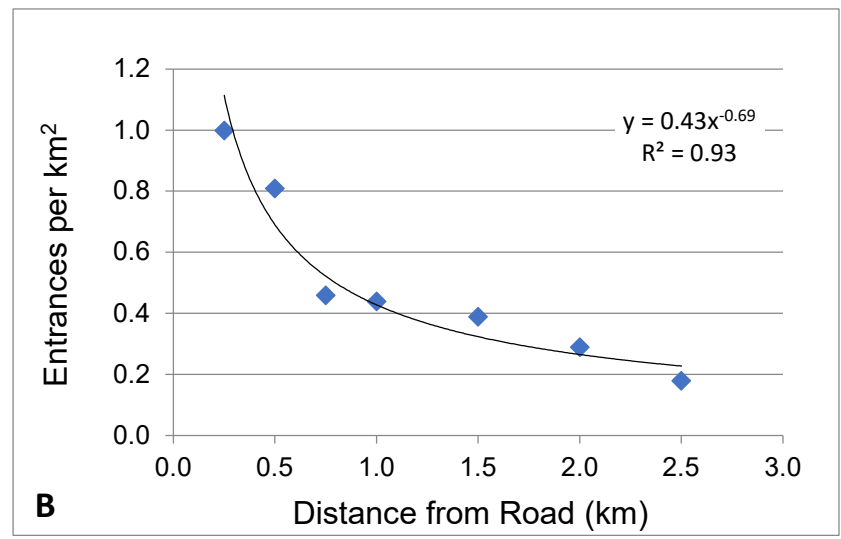
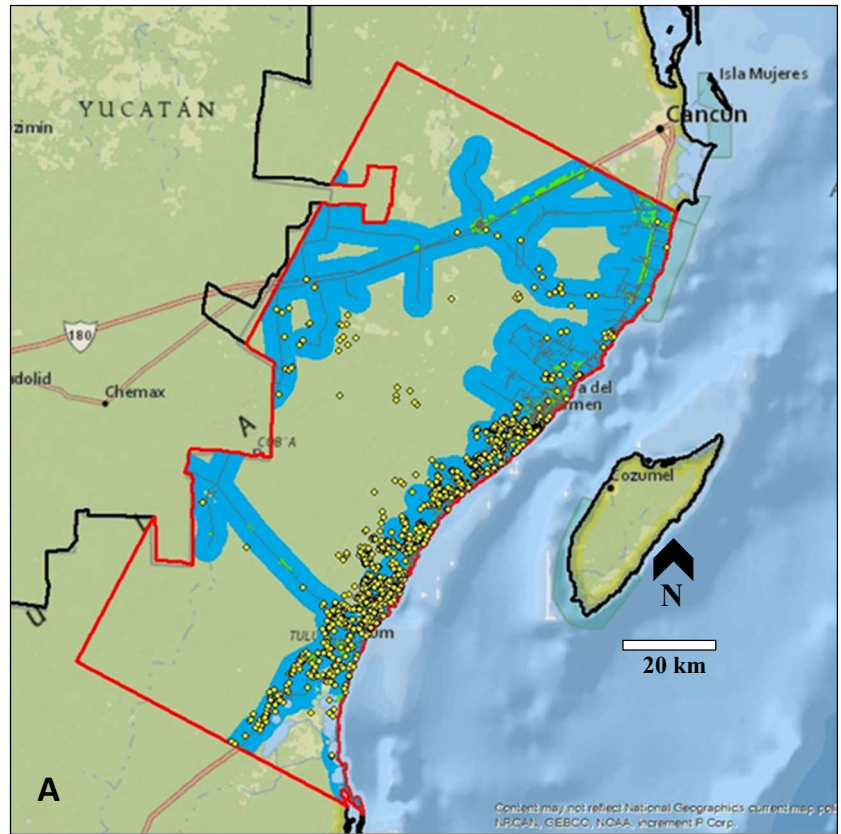


Figure 2-23. Access bias in cave entrance data. A weighted overlay was applied across the study area (A) to assess cave entrance density as a function of distance from roads (B).

2.3.3 Line-intercept field surveys

Line-intercept surveys adjacent to Sistema Jaguar documented 119 sinkholes along four transects: 24 sinkholes along Howling Man, 28 along Chango, 40 along Vincejos, and 27 along Barrel (**Figure 2-24**). Results are summarized in **Table 2-4**. Ten 30-m lines were surveyed on each transect, except at Barrel where time constraints permitted only 7 lines. The number of sinkholes encountered along each line ranged from one to eight (**Figure 2-25**). A Kruskal-Wallis chi-squared statistic of 7.85 (df= 3), demonstrated a slightly significant difference between the mean number of sinkholes sampled along each line (p-value= 0.05). A post-hoc Dunn's test of multiple comparisons found significant differences between Howling Man and Barrel transects (z= 2.14, p= 0.02) and between Howling Man and Vincejos transects (z= 2.32, p= 0.01).

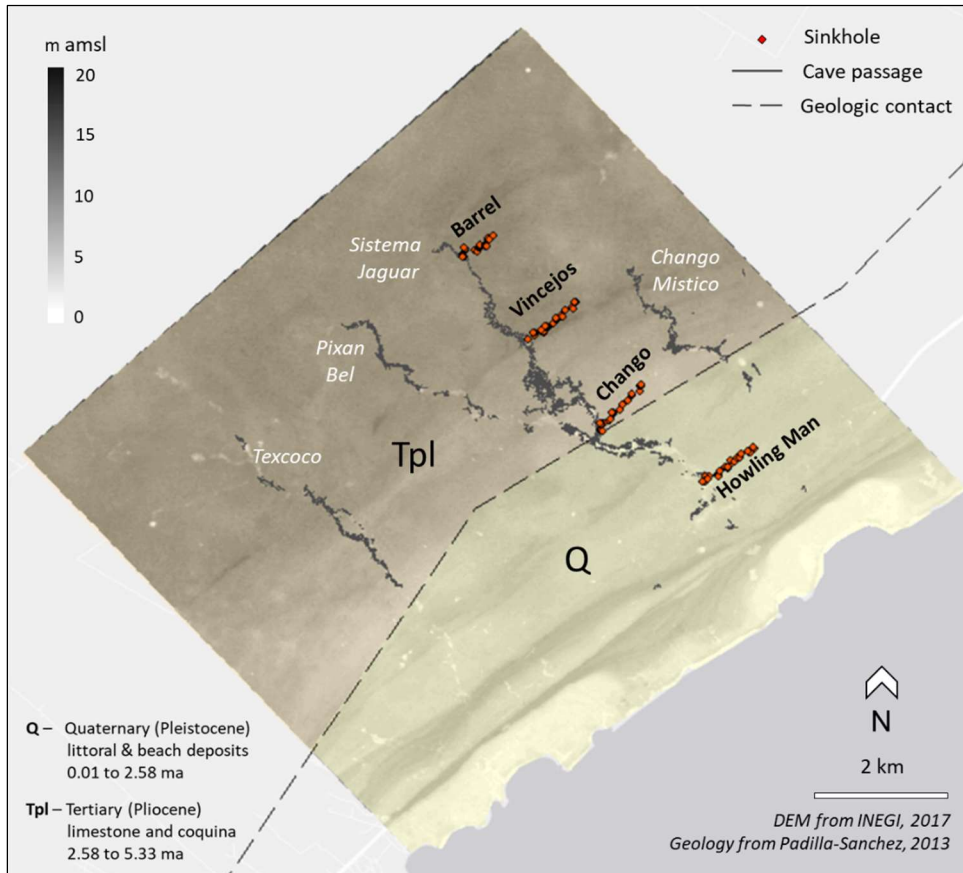


Figure 2-24. Map of sinkhole survey transects. Line-intercept surveys of sinkholes (red dots) were compared to corresponding zones of depression densities estimated from a DEM.

Table 2-4. Sinkholes identified in line-intercept surveys.

Line no.	Howling Man	Chango	Vincejos	Barrel
1	2	5	8	5
2	3	2	4	3
3	2	3	3	4
4	3	5	5	4
5	4	3	3	6
6	2	2	5	3
7	1	1	3	2
8	4	3	2	NA
9	2	1	4	NA
10	1	3	3	NA
Total	24	28	40	27
Ave. per line	2.4	2.8	4.0	3.9

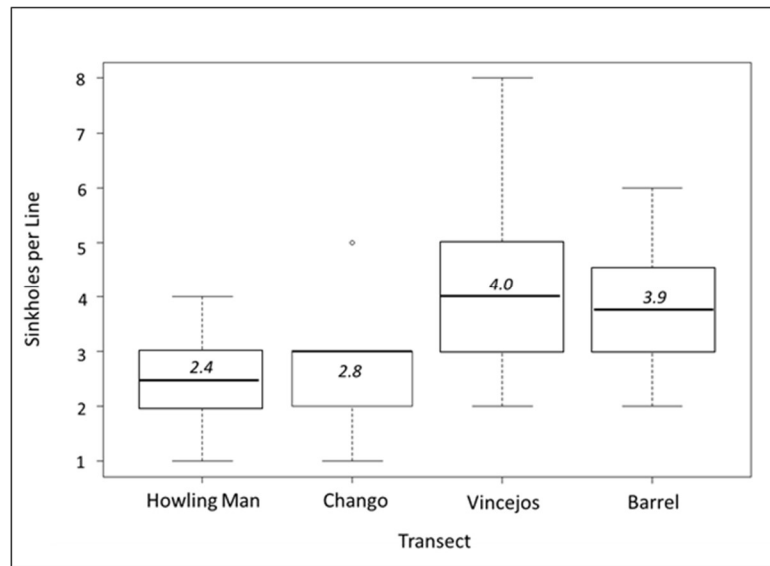


Figure 2-25. A box-plot comparison of survey transects. Each box depicts the summary statistics for the number of sinkholes found per line along each survey transect.

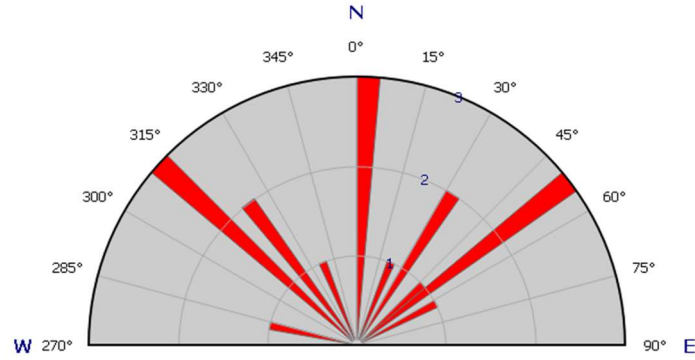


Figure 2-26. Directional data from field measurements. Nearest neighbor direction was measured as the alignment in clusters of sinkholes in the field, and orientations were measured as the long axes for elongate sinkholes (circular depressions had no orientation) (n= 18).

2.4 Discussion

2.4.1 DEM Analysis

2.4.1.1 Frequency distributions of spatial scale

Sinkholes occur across a range of scales depending on their formation process and geologic influences. When all formation processes and hydrogeologic conditions are equal, the scale of sinkhole development is expected to follow a probabilistic distribution, i.e., the frequency of an occurrence of a given size (or depth) is inversely proportional to some power of its size (Pardo-Igúzquiza et al., 2019). Power distributions are observed for depression depth, length, and width (**Figure 2-9**). Length and width dimensions are grouped into 5 m bins with a minimum size of 5-10 m based on the limit of the DEM resolution. One exceptionally large, shallow depression (~255 m x 520 m) is an outlier in both width and length distributions.

DEM processing identifies depressions based on the elevation difference from the surrounding land surface but does not recognize artifacts such as roadside ditches, and cannot measure the depth of water-filled cenotes or distinguish between collapse and solution sinkholes. The potential for anthropogenic artifacts is low in the study due to the lack of urban development, and so all depressions were considered in analysis. LiDAR tends to reflect off water surfaces, and therefore the bottom elevations of cenotes represents the water table rather than total depth. Cenotes are only identifiable in the DEM by visual comparison with satellite imagery and were not considered separately in the automated sink-fill process. Sinkholes in the study area are expected to fall in three categories defined by their origin process: 1) “collapse sinkholes” formed by the thinning and failure of cave ceilings, 2) “solution sinkholes” that form as a result of focused water infiltration and dissolution along vertical pathways, and 3) “swales” that are hypothesized to form where a solution sinkhole intercepts the water table and continues to develop laterally into a wide, shallow depression (Tulaczyk, 1993).

2.4.1.2 Morphometrics & Orientation

Differences in sinkhole morphology have been used to categorize sinkholes at a regional scale in Quintana Roo and to the west in the state of Yucatan (Aguilar et al., 2016; Fragoso-Servón et al., 2014). Depression classes in those regional studies included “poljes” with an area $>1 \text{ km}^2$, “uvalas” with an area $<1 \text{ km}^2$ and a circularity greater than 1.3 (tending away from circular), and “dolines” with an area $<1 \text{ km}^2$ and a circularity less than <1.3 (circular). In our sub-basin scale study, there were no features that qualified as poljes, although the largest depression had an area of 0.73 km^2 . Nearly all depressions in this study qualified as ‘uvalas’, with a circularity index centered at 1.3. The measure of

eccentricity showed two groups, centered at 0.6 and 0.9. However, because these did not show any patterns in geographic distribution or correlation to other parameters, eccentricity is not a conclusive metric for sinkhole classification. All measures of morphology were similar across geologic units, suggesting that formation processes are acting equally across the study area despite local differences in rock properties.

The orientation of all depressions, measured by the azimuth of the long axes, displayed three dominant trends at 45 to 50°, 285 to 290°, and 340 to 345° (**Figure 2-11**). The depressions in each geologic unit showed similar trends, although there were proportionally more oriented at 340 to 345° in the older, Tertiary-age unit. The hydraulic gradient has been measured approximately perpendicular to the coastline, which is close to this orientation, and suggests that karstification along regional flowpaths controls the orientation and alignment of at least a portion of the depressions in the study area. This is supported by the orientation of mapped cave passages in the study area, which are also generally perpendicular to the coast. Trends at 45 to 50° potentially represents structural control along the Rio Hondo fault zone that extends southeast toward Tulum, and the set at approximately 285 to 290° is could be related to jointing, though no joints were document in caves or on the surface due to lack of outcrops.

2.4.1.3 Distribution & alignment

Clustered distributions of sinkholes can be explained by two processes: (1) areas containing sinkhole clusters have similar geologic and topographical settings that favor formation; (2) positive feedback systems promote sinkhole formation: i.e., existing sinkholes focus runoff into underlying passage, which increases the solution and erosional processes in adjacent areas and leads to new sinkholes (Gao et al., 2005).

Sinkholes in the study area were highly clustered, and those in the older, inland rock unit were more clustered than those in the younger, coastal rock. Greater clustering in older rock could simply reflect the greater length of time available for sinkhole formation that is concentrated along flow paths.

The size of a sample area has a considerable influence on results because a set of points may be random at one scale but non-random in the context of the region in which a study site is located (Williams, 1981). The scale-dependent nature of clustering makes it necessary to evaluate patterns at different search distances, such as with increasing nearest neighbors or as an expanding search radius around points. NNA was done up to the 9th Nearest Neighbor distance and compared between geologic units (**Figure 2-15**). Mean clustering distances were similar between geologic units up until the 7th nearest neighbor, at which the younger, coastal unit has a slightly lower clustering distance, which is expected because the distance between centroids is limited by the coastline. Ripley's K is another scale-dependent clustering metric, and this method identified the greatest clustering occurring at a 380 m search distance around a point (**Figure 2-17**). The kernel density map based on this point radius revealed clustering along known cave passage, in areas where no mapped caves occur, and parallel to the coastline. Clusters inland may indicate zones of enhanced dissolution related to local rock or structural properties, or even areas containing unmapped caves. The coastal parallel clustering could contain a few artifacts related to road construction, but largely reflects the alignment of different geologic facies deposited along the shoreline.

The alignment of depressions shown by the direction to nearest neighbor had two dominant trends at 45 and 315°. These directions are roughly parallel and perpendicular to the coastline, respectively, and are similar to the distribution of linear cave passage in the study area (**Figure 2-21**). The alignment of depressions contrasts somewhat with the orientations of sinkholes measured at 45 to 50°, 285 to 290°, and 340 to 345°. The difference between alignment and orientation of karst features suggests that different hydrogeologic and structural controls are acting across scales. The range of orientations suggests that the study area contains structural influence from both the Rio Hondo and the Holbox fault zones, and that local jointing or variability in depositional structures may exert control on sinkhole orientation. The alignment of depressions, and trends of cave passage, likely reflect the direction of hydraulic gradient over the time of their development.

2.4.2 Cave entrance data

Some urban areas developed over karst maintain databases of karst features such as caves and sinkholes or cenotes, and these data can be useful to characterize regional geology or to assess risks of sinkhole formation (Aguilar et al., 2016; Brinkmann et al., 2008; Gao & Alexander, 2008). They can also provide valuable information for scientific purposes but must be used cautiously as the data is selective and potentially biased by exploration or reporting. This study uses cave entrance data to calculate point density in different geologic units and compares results to similar analysis using centroids identified in the LiDAR-derived DEM. The number of cave entrances is 6 per km² in the coastal, Quaternary-age unit, compared to 1 per km² in the interior, Tertiary-age unit. These results contrast with the analysis of point density of depressions, which found 15 per km²

in the coastal unit and 26 per km² in the interior unit. This could reflect a difference in scale, as cave entrances represent a sub-set of all depressions, specifically those that are humanly enterable and usually formed by the collapse of cave passage (in this study area). However, cave entrance data was determined to be biased by the ease of accessibility, and specifically to the proximity to roads, so this suggests that without a full and unbiased dataset, cave entrance density is not a useful indicator of karstification. This does not mean that cave entrance data are un-useable, but that it must be interpreted alongside other data, such as DEM analysis or systematic field sampling. However, higher entrance density might be expected closer to the coast where flow paths converge at discharge points and cave roofs are thinner and more prone to collapse.

2.4.3 **Line-transect surveys**

Systematic sampling methods developed for ecological applications (Gillison & Brewer, 1985; Kaiser, 1983; Warren & Olsen, 1964) provide a means to reduce bias in karst studies. Our line-transect surveys determined only a slightly significant difference in sinkhole density between the four parallel zones. Qualitatively, there appeared to be fewer, but larger, collapse sinkholes in the two transects closer to the coastline, and more, smaller solutional sinkholes in the two zones farther inland. While cave entrance data is selective of large-scale features, our line-intercept surveys represent the smallest practical scale of observation, and therefore results may reflect different factors of influence. Field measurements of sinkhole alignment also detected trends of 315 and 45°, which agrees with Nearest Neighbor Analysis and trends of cave passage, suggesting that similar influences on development and evolution of flow paths are operating across meter to km scales.

2.5 Conclusions

Probabilistic distributions of sinkhole size, and similar morphologies across geologic units are indicative of similar formative processes and hydrogeologic conditions across the study area at the km-scale. Trends in sinkhole orientation observed at 45 to 50° and 285 to 290° potentially reflect flow paths along fracture sets in the Rio Hondo Fault Zone, while trends at 340 to 345° likely reflect flow paths along the hydraulic gradient toward the coastline.

Higher point density and greater clustering of depressions is observed in the older, inland rock unit, which is expected with more time for karstification to occur. More cave entrances are documented along the coast, and entrance distribution is strongly biased by distance to roads. Field surveys noted a change in scale from large collapse sinkholes near the coastline to more numerous solution sinkholes in the interior. The alignment of sinkholes from field observations agreed with those obtained from Nearest Neighbor analysis and from cave passage orientations, indicating that similar processes influence sinkhole and cave development across scales.

Karstification appears to be strongly influenced by structural features associated with the intersections of the Rio Hondo Fault Zone and the Holbox Fracture Zone, which is likely a sub-block of the mostly submarine Catoche Fault Zone. The large number of caves near Tulum has been attributed to the intersection of the Rio Hondo and Holbox zones (Gondwe, 2010; Kambesis & Coke, 2016). Our results support previous work correlating gravitational anomalies with karst features (Connors et al., 1996) that suggested alignments of karst features along the eastern coastline are evidence of fractures paralleling, and probably connecting, the submarine Catoche Fault Zone to the

north and the Rio Hondo Fault Zone in the south. This is consistent with the tectonic interpretation of Cozumel as a fault block in a horst-and-graben extensional fault system that continues off-shore (Ward et al., 1985), and with indications of divergent seismic activity during the Tertiary in the Yucatan basin (Rosencrantz, 1990) and near Belize (Ester Lara, 1993).

Further work could be done to clarify the effects of sinkhole clustering on the elevation of the water table. It would be expected that clusters represent areas of greater permeability and may be correlated with a localized decrease in hydraulic head. In particular, the large shallow depression to the north of Chango Mistico contained a cluster of sinkholes oriented NNE, where flow is thought to be directed along the Rio Hondo fault zone (Tulaczyk, 1993). The common occurrence of wetlands inside large, shallow depressions is indicative of connectivity with groundwater, and these features could be used as monitoring points for water table elevation.

3. CONSTRAINING AQUIFER PROPERTIES IN A TRIPLE-POROSITY COASTAL KARST BASIN: SISTEMA JAGUAR, QUINTANA ROO, MEXICO

Abstract

Tidal and storm signals in water level data from epiphreatic conduits were analyzed over a two-year period to constrain hydrogeologic properties and identify heterogeneity in a coastal karst aquifer. Values ranged from: diffusivity (D) = 1.74×10^7 to 1.02×10^9 m²/d; transmissivity (T) = 5.23×10^6 to 3.07×10^8 m²/d, assuming storativity (S) = 0.1 to 0.3; and hydraulic conductivity (K) = 4.36×10^4 to 2.55×10^6 m/d, using the total permeable aquifer thickness of 120 m. Hydraulic gradient is steepest near the coastline (1.2 m/km at 0.5 km inland) and flattens to ~ 0.1 m/km beyond 5 km inland. We estimate coastal discharge (Q) at 0.38 m³/s per km of coastline, assuming annual precipitation of 1,293 mm/yr and a recharge of 17%, but this is limited by uncertain basin boundaries and spatially variable ET. Storm recession curve analyses results indicate triple-porosity flow partitioning of 61% conduit, 30% fracture, and 9% matrix. Our findings corroborate previous work in active phreatic conduits ~ 50 km to the south but indicate that K is lower near the coastline, as evident by steeper coastal gradients. The coastal units are likely responsible for a locally thicker freshwater lens and engineered modification of the coastline has the potential to significantly drain the aquifer.

3.1 Introduction

The northern portion of the Yucatan Peninsula is a geologically young carbonate platform that is subject to dissolution by rapidly infiltrating rainwater. The landscape is highly karstified, which means that it is characterized by fractures and voids that enlarge

as dissolved carbonate is transported via groundwater flow. This well-drained karst surface does not support lakes or rivers, and consequently, surface water is only found where the low-relief surface intersects the water table, or where bedrock collapse creates windows into the aquifer (locally known as cenotes). Carbonate dissolution is accelerated in coastal karst where fresh and saline waters mix to produce a solution undersaturated with respect to calcite (Back et al., 1986, 1979), although many cenotes are found tens of kilometers away from the coast at depths where no mixing currently occurs. It was assumed that no traversable conduits existed between them until exploration by cave divers began in the 1970's (Worthington et al., 2001). Over 1,300 km of phreatic cave have been mapped in Quintana Roo, and 130 km of cave above the water table has been mapped in just the past 10 years (QRSS, 2019). Traversable connections between caves above and below the water table continue to be discovered, and this on-going exploration has the potential to refine the current understanding of hydrogeologic connectivity.

Our study is the first in this area to examine the hydrogeologic role of recently explored caves at the water table. These conduit networks extend inland perpendicular to the coastline and allow water level measurements along transects that provide valuable insight into hydrogeologic heterogeneity and related changes in coastal hydraulic gradients. Our objectives were to constrain aquifer properties and identify heterogeneities at a sub-basin scale. Small-scale data is needed to inform the development of civil infrastructure that is rapidly occurring as a result of a growing tourism-based economy, yet most prior work has focused on regional-scale aquifer properties (Gondwe, 2010; González-Herrera et al., 2002; Moore et al., 1992).

Groundwater basins in the Yucatan Peninsula are challenging to define because of limited data, extremely flat gradients on the order of 1-10 cm/km (Beddows, 2004; Gondwe, 2010; Marin, 1990; Moore et al., 1992) relatively low topographic relief, and lack of geologic contacts with non-carbonate rocks exposed at the surface. Previous work in the northeastern Yucatan Peninsula has recognized the Holbox Fracture Zone, an area of low-permeability characterized by large NNE-trending karst depressions, as a regional groundwater divide (Gondwe, 2010; Perry et al., 2002; Tulaczyk et al., 1993). This zone runs parallel to a Paleozoic basement structural high and has been interpreted as the surface expression of normal faulting in buried volcanic rock that continues into the Caribbean Sea (Ward et al., 1985). It extends approximately 50 km inland from the coastline and directs flow northward (Gondwe, 2010). The southern terminus near Tulum is characterized by a high concentration of cenotes (Ward et al., 1985). Boundaries between sub-basins within this zone have not been delineated, as these would be strongly controlled by the presence of conduits and the local heterogeneity of bedrock facies that would influence the hydraulic gradient.

Water budgets for the Yucatan Peninsula are poorly constrained. Discharge estimates from prior work based on assumed boundary conditions are compared in **Table 3-1**. Lesser (1976) used the empirical fit Turc equation based on mean annual temperature and precipitation to arrive at 90% ET. He removed an additional 5% based on his observation of very efficient infiltration through the often exposed bedrock, to arrive at 85% ET, a value that has been widely cited (Back et al., 1979; Ward et al., 1985). ET of 85% of a peninsula average MAP of 1,050 mm/year equates to a recharge of 150 mm/yr. This in turn, equates to a discharge of 0.26 m³/s per km of coastline for a

basin boundary that reaches 50 km inland. Similarly, Gondwe (2010) calculated recharge of 17% MAP, or about 200 mm/yr in the area of the Sian Ka'an Biosphere Reserve with MAP of ~1,200 mm/year (50 to 120 km south of study area), based on remotely sensed data. This estimate was arrived at using the 'triangle method' that interpolates differences between modeled and observed surface temperatures (Carlson, 2007) and then applies ET rates across mapped precipitation data. In contrast, Beddows (2004) measured coastal groundwater flow in major conduits near Tulum and observed average coastal outflow of 0.73 m³/s per km of coastline. The three-fold discrepancy between calculated values and direct discharge data could result from: 1) poorly defined or variable groundwater basin boundaries that do not account for conduits that potentially channel water from adjacent areas; 2) overestimation of ET and therefore underestimation of recharge rates; and/or 3) under-evaluation of MAP. In all cases, these results highlight the need for studies to delineate basins and constrain aquifer properties and groundwater fluxes across a range of scales.

Table 3-1. Discharge estimates from prior work. Each study used different assumptions of ET and precipitation values. All assume a basin 5 km wide extending up to 50 km inland.

	Lesser, 1976	Hanshaw & Back, 1985	Beddows, 2003	Gondwe, 2010
Mean Annual Precipitation (MAP)	1050	1050	1500	1195
Recharge % OF MAP	14	15	30	17
Q m ³ /year	8.09 x 10 ⁶	8.66 x 10 ⁶	2.48 x 10 ⁷	1.11 x 10 ⁷
Q m ³ /s per km	0.26	0.27	0.78	0.35

Accurate discharge calculations require precise measurement of hydraulic gradients, which are challenging to obtain in the Yucatan Peninsula because of dense vegetation that obscures high-precision GPS signals and a near-complete lack of monitoring-well infrastructure, even in major urban centers. Prior work found that regional gradients are extremely low. Regional gradients across the northwestern portion of the Peninsula were as low as 0.01 m/km (Marin, 1990). Approximately 50 km south of the study site near Tulum gradients of 0.05-0.1 m/km were measured in cenotes (Beddows 2004). Approximately 30 km north of the study site near Playa del Carmen gradients were measured at ~0.1 m/km (Moore et al., 1992). Gradients along the northeastern portion of the peninsula were measured at 0.2-0.3 m/km (Moore et al., 1992), but were locally much higher within 1 km of the coast at 1-2 m/km (Tulaczyk, 1993), possibly due to the lower permeability of chemically altered coastal rock.

Geologically young carbonates that have not been buried and are relatively undeformed by tectonic activity are expected to have relatively high primary porosity. Matrix porosity from core samples across the peninsula is 17- 45% (Smart et al., 2006). Hydraulic conductivity of cores samples collected near Merida range from 1×10^{-6} to 5×10^{-3} m/s (Gonzalez-Herrera, 1984), while hydraulic conductivity (K) based on borehole pumping tests in the northwest near Merida resulted in higher values (9×10^{-4} to 10^{-2} m/s) (Gonzalez-Herrera, 1992). It is not unexpected that regional-scale measurements result in higher K values, as pump tests integrate fracture/fissure/conduit flows at the km scale.

Subaerially exposed carbonates can become chemically altered where calcite-saturated water evaporates to produce finely crystalline cement and caliche. This process lowers permeability and results in lower hydraulic conductivity, with related effects on

hydraulic gradients (Rotzoll et al., 2013). Finely crystalline cement and caliche deposits have been documented across the northern Yucatan Peninsula and are indicators of an arid Pleistocene climate, in which intense evapotranspiration induced calcite precipitation (Ward, 1978; Ward et al., 1985). A nearly impermeable calcareous layer of 0.5-1.4 m thick acts as a confining unit along the north Yucatan coast (Perry et al., 1989), and this is potentially related to locally high coastal gradients of 1-2 m/km (Tulaczyk et al., 1993). Sub-horizontal layers of dense caliche cement (“calcrete”) ranging from 2 cm up to 2 m have been documented both at the surface and in the subsurface as far as 12 m below sea level along the northeastern Caribbean Yucatan coast (Rodriguez, 1982).

Permeability in the Yucatan Peninsula is generally very high, as is evidenced by the very low regional gradients despite high recharge volumes (Ward et al., 1985). Zones of high and low permeability were identified by a review of hydraulic conductivity values from literature (Bauer-Gottwein et al., 2011). The nearest zone to the study site, Playa Del Carmen, was evaluated as an area of moderate permeability with a hydraulic conductivity of 0.19-0.65 m/s measured on the scale of 10’s of km (Moore et al., 1992). The Holbox Fracture Zone has been identified as a zone of high permeability, likely related to large shallow depressions (locally called *sabanas*) aligned with faulting that facilitates groundwater flow (Gondwe, 2010). Generally, secondary permeability at depth is expected to remain high due to a lack of surface sediment to infill conduits as they develop.

Groundwater in the Yucatan Peninsula is argued to flow primarily through conduits in a dual porosity aquifer (Bauer-Gottwein et al., 2011), and this has been used for several regional-scale models (Charvet, 2009; Gondwe, 2010; Marin, 1990). A triple

porosity model additionally considers interconnected fracture flow and solution-enlarged bedding planes. The depositional matrix porosity of Pleistocene carbonates along the northern coastline ranges from 29% to 50%, but this has generally been reduced to 14%–23% by cementation (Harris, 1984). Matrix porosity as high as 45% was measured from drill cores near Merida on the northwestern side of the peninsula (Gonzalez-Herrera, 1984), and matrix porosity has been modeled as 35% in Yucatan state (González-Herrera et al., 2002). Worthington et al., (2001) calculated fracture porosity of 0.1% based on pumping tests done near Merida by Gonzalez-Herrera, (1992). Conduit porosity of 0.5% was determined using volume estimates from cave survey data (Worthington et al., 2001).

3.2 Regional Setting and Study Site

3.2.1 Geology

The thick carbonate strata of mixed limestone and dolomite forming the Yucatan peninsula were deposited in shallow to deep marine environments from the Cenozoic through the Holocene (Ward et al., 1985). A Pemex exploratory oil well drilled in Quintana Roo in 1973, Yucatan No. 4, encountered Jurassic-age quartz arenites at ~1,400 m and basement volcanics at 2,425 m (Ward et al., 1985). Near-surface strata are generally flat lying, resulting in a nearly level topography across most of the peninsula. Geologic formations exposed at the surface range in age from Eocene (34-56 ma) limestone at the center of the peninsula to Holocene (<8 ka) beach sediments along the shoreline (**Figure 3-1**). Pleistocene reef corals exposed on the surface near Xel-Há were dated to 125,000 years before present and have been interpreted as correlating with the last high stand at 6 m above modern sea level (Szabo et al., 1978).



Figure 3-1. Geologic map of the Yucatan Peninsula. The study area is located in 5.3 million year old (Ma) Pliocene to modern Holocene limestones formed in a variety of depositional environments including reefs, shallow marine deposits, and ancient to modern beaches (data from Padilla-Sanchez, 2013; imagery from ESRI 2019).

3.2.2 Climate

Regional climate is subtropical with average annual rainfall ranging from near arid at 550 mm on the north-west coast of the peninsula to 1,500 mm along the eastern coast (Ward et al., 1985) and most rainfall occurs during the June-October rainy season. Hurricanes hit the eastern Yucatan coast on average of about 1 per year based on available records from 1917 to 2017 (NOAA, 2019). Average temperatures since 1982 range from 28.1° C in May to 22.6° C in January (Climate-Data.org, 2019).

3.2.3 Study site

The study area extends 10 km inland from the Caribbean coastline near the towns of Paamul and Puerto Aventuras at ~ 70 km south of Cancun, Mexico (**Figure 3-2**). Surface geology is mapped as Pliocene limestone and coquina consisting of bivalve and gastropod fragments (2.6 to 5.3 Ma), with Quaternary littoral deposits extending up to 2.5 km inland (INEGI, 1997). Exposed carbonates consist of shallow marine, reef, shoreline, and eolianite limestones, with patchy layers of calcrete up to 1 m thick over much of the surface (Richards & Richards, 2007). The coastline itself consists of Holocene deposits overlying Pleistocene beach-plain grainstones and reef limestone (Lauderdale et al., 1979).

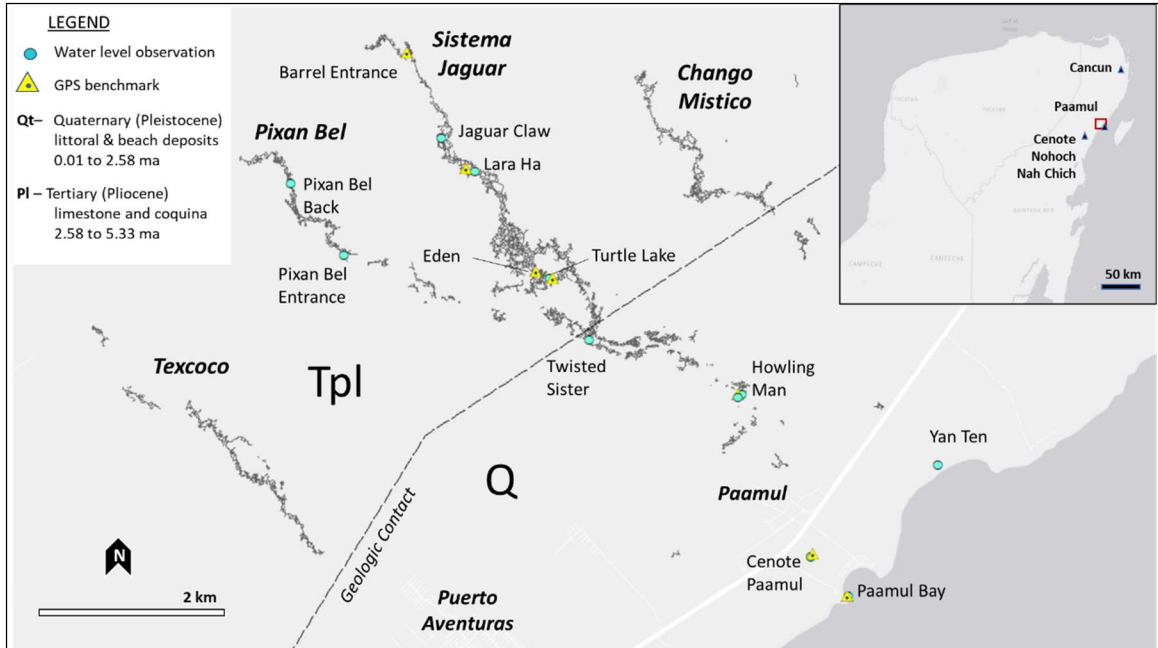


Figure 3-2. Geologic map of the study area with mapped cave passage. Documented caves in the study area include >130 km of mapped passage (QRSS, 2019), shown by solid black lines. The geological contact shown by the dashed line is approximately 4 km inland and parallel to the coast (Padilla-Sanchez, 2013). Most caves explored in the study area are in the Pliocene limestones (Tpl), with Quaternary (Q) shallow marine (littoral) and beach deposits overlying it approximately 2 km inland. The shoreline consists of Holocene (10 ka) reef rock and modern beach of calcareous sand.

The study site includes Sistema Jaguar, an epiphreatic cave system with more than 45 km of surveyed passage (Sprouse, unpublished) that extends 7 km inland perpendicular to the coastline from the Paamul area, and a related series of dissected caves extending coastward. The caves of this study lie almost entirely at or above the water table and provide easy access for observing aquifer hydrology and morphology, without the need for SCUBA equipment. The northern end of Sistema Jaguar consists of a mostly singular passage that converges with the remnants of collapsed passages to the west of the cave at about 5 km from the coast. The remnant passages appear to have once been connected with Pixan Bel but collapsed as a result of surface erosion and loss of

buoyant support when sea level dropped. The cave widens and becomes maze-like at this convergence, with a 1-3 m thin ceiling that contains over 200 collapsed entrances toward the southern end.

Shallow isolated epiphreatic pools (<1 m deep) are common near the coast, but passages beyond 2 km from the coast feature 2 to 5 m deep water pool networks up to several kilometers in length. The most-inland passage known in Sistema Jaguar terminates 7.4 km from the coast in collapse and possible underwater passages that remain unexplored. Neighboring caves to the north and south of the study area are known to contain unexplored water-filled passages that potentially connect to deeper phreatic conduit networks, and there is no reason to expect that passages in Sistema Jaguar are any different. Nearly all cave passage in the study area was mapped by a dedicated team of volunteer explorers since 2008; prior to which it was assumed that caves at or near the water table were generally small and not well connected. Exploration below the water table in this area has only recently been attempted in a limited number of sites, in contrast to areas ~30 km to the south around Tulum where cave diving has been the primary mode of exploration and has attracted explorers from around the world since the early 1970's.

The groundwater basin that includes Sistema Jaguar is assumed to be approximately 5 km in width along the coastline based on consistent spacing observed between parallel coastal caves throughout the Riviera Maya (Kambesis, 2014). Sistema Jaguar lies between two parallel epiphreatic cave systems: Chango Mistico to the northeast, and Texcoco to the southwest. Survey data and field observations suggest that Sistema Jaguar and nearby Pixan Bel (~12km of mapped passages) were at one time joined by passages that are now mostly collapsed, though these caves may remain

hydrologically connected. Many smaller caves that lie along obvious trends appear to be remnants of a larger system that collapsed as a result of erosional thinning of the roof and loss of buoyant support with a drop in sea level.

The spacing of parallel epiphreatic systems in the study area is consistent with prior work that documented 6 km spacing between major active phreatic conduits along 150 km of the northeastern coastline of Quintana Roo (Kambesis, 2014). Focused groundwater discharge from phreatic conduits forms a series of large springs in small coastal bays known as caletas; each of which is associated with an underwater cave system. Such caletas occur 2-3 km south of Sistema Jaguar at Puerto Aventuras, and 2-3 km north along the coast between Paamul and Xplor Ecopark. The study area also contains a sandy cusped beach called Paamul Bay where many freshwater seeps can be observed discharging along the shoreline, and temperature and salinity variations are detectable in the bay. These observations suggest that, in addition to point discharge at caletas, groundwater also discharges via fractures and/or buried and collapsed conduits.

3.3 Materials and Methods

3.3.1 Instrumentation and data collection

Instrumentation was installed to collect high-temporal resolution water level data at ten sites for different durations from August 2015 through to August 2018, including two years of 30-min resolution water level data from Sistema Jaguar. Additionally, 1-min resolution data was collected for two to five days at selected sites up to 5 km inland (**Figure 3-3**). Tidal amplitude and attenuation with distance inland were determined, as well as seasonal differences where possible. Analysis of recession curves following the

transit of tropical storms also provided insight into the relative importance of conduit, fracture, and matrix flow, respectively.

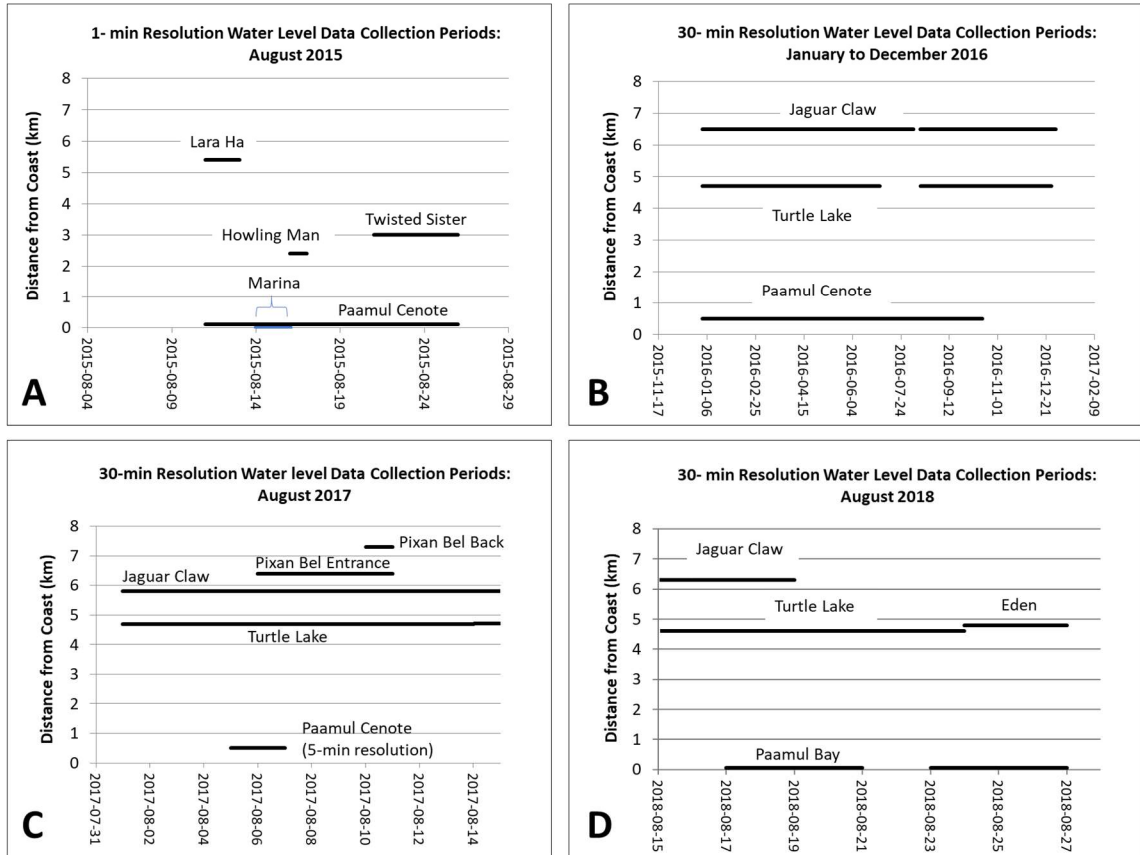


Figure 3-3. Summary of water level data collection periods. Both short term (days to weeks) and long term (months to years) water level data were collected from August 2015 to August 2018. Observations overlap across sites and data intervals. Measurements of 1-min resolution were taken at five sites in August 2015 (A). Data loggers were left at three sites taking 30-min interval readings in January 2016, and some data were lost due to instrument drift (B). Short-term observations were made at five sites in August of 2017, and loggers were left in place at two sites (Jaguar Claw and Turtle Lake), taking readings at 30-min intervals (C). The two long-term loggers were retrieved in August of 2018, and additional short-term data were collected in Paamul Bay and Eden.

Water level data were recorded using Schlumberger CTD Diver logging sensors with ± 0.1 cm/H₂O water level resolution set to log at 30 min intervals. Each Schlumberger logger was paired with a Schlumberger barometric data logger

(± 0.03 cm/H₂O) set above the water table. All sensors were corrected for inter-instrument off-sets relative to each other for a minimum of 12 hours on-site prior to each deployment in the field. Elevations of the placement of barometric loggers in the caves was determined by survey with a DistoX2 handheld laser (± 0.2 cm, $\pm 0.5^\circ$) from the instruments to the existing cave survey, and tied to benchmarks on the surface and/or from 0.5 m LiDAR derived contours (interpolated from a 5 m DEM obtained from INEGI).

Benchmarks were marked with hand-drilled 3/8" bolts and yellow-painted washers and established using a high-precision Trimble Geo7x-cm with Tornado antenna differential GPS (up to ± 0.01 m horizontal, ± 0.02 m vertical). Benchmarks were set on the surface near entrances at Turtle Lake, Eden, Lara Ha, and Barrel Entrance, and tied to the existing cave survey by handheld laser survey with maximum survey loop closure of 0.13 m horizontal and 0.01 m vertical. Additional benchmarks were set at sites between the coast and Sistema Jaguar (Howling Man and Paamul Cenote) where the water table is easily accessible. A final benchmark was set near sea level at a rocky point on Paamul Beach and surveyed to an Arduino sensor set in the ocean. GPS files were differentially corrected using 15-second interval RINEX files from a UNAVCO base station in Puerto Morelos (TGMX; 16N 20.879N, -86.862W in UTM NAD83; UNAVCO Data Archive Interface 2018) with elevation referenced to global mean sea level (msl). Distances of sites from the coast were obtained using GPS locations, georeferenced cave survey data, and satellite imagery in ArcMap 10.6.

Hydraulic head was calculated by subtracting the vertical distance between the sensors and adding the barometric-corrected water depth from the submerged logger (Figure 3-4). At the time of placement and each download (approximately 4, 8, or 12 months apart), direct measurements of water depth above the loggers were made to check for instrumental drift. In August 2017, two Arduino based loggers (Beddows & Mallon, 2018) were used in Pixan Bel, a large cave southwest of and roughly parallel to Sistema Jaguar, with the same placement and calibration methods. All pressure measurements were recorded in cm/H₂O.

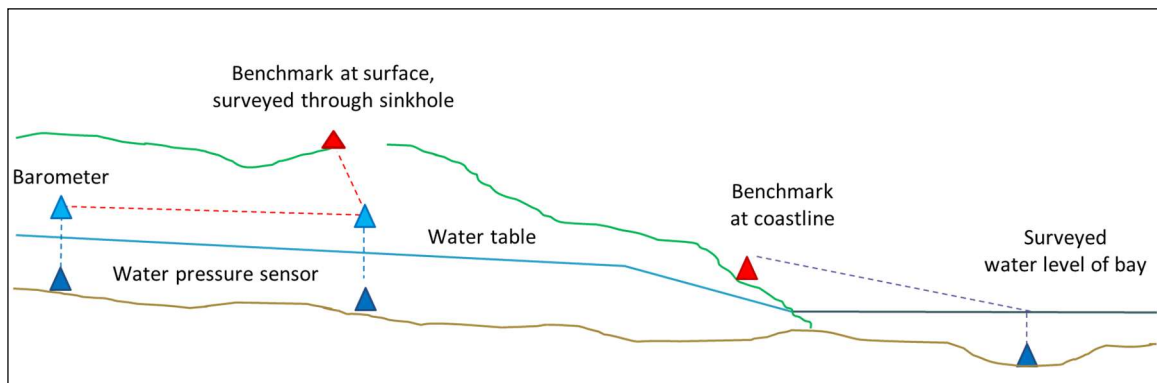


Figure 3-4. Diagram of water table observation methods. Pairs of submerged pressure sensors (dark blue triangles) and barometers (light blue triangles) were used to measure relative changes in water levels. Elevations were determined by surveying the observation stations to benchmarks at the surface (red triangles) that were established using differentially corrected GPS.

Sites for data collection were selected between the coast and 7 km inland (Figure 3-2), with those at ~2, 4, and 6 km selected to provide comparison with work previous work in Nohoch Nah Chich (Worthington et al., 2001). In August 2015, a cenote just northeast of Paamul and ~70 m from the coastline, known locally as “Yan Ten”, was used as a point of reference for tidal signals and relative water level measurements. This location was later changed due to its popularity as a swimming hole and instrument theft.

The Paamul Cenote, located ~0.5 km from the coastline, was used instead from January 2016 to August 2017.

Porosity of rock exposed in cave walls (n= 11) and on the land surface (n= 3) and was assessed with hand samples. Samples were dried at 80° C for 36 hours until mass was no longer decreasing and were then vacuum pumped at 0.25 atm for 15-30 min in deionized water until air no longer bubbled out. The samples were weighed again for mass increase, and their volume measured by displacement to obtain porosity values.

3.3.2 Quantitative analysis

Time-series hydraulic head data were analyzed as a foundation for calculating aquifer properties and to constrain a water budget. The mathematical framework allows matrix discharge estimates across a range of values for gradient, thickness of the water table, and passage dimensions. The resulting Q-matrix represents flow through a porous media, similar to the problem of a leaky earthen dam, where matrix discharge is the volume of water that flows through the dam (Remson et al., 1971), or in this case, though less permeable coastal rock (**Figure 3-5**). Hydrogeologic parameters are described and related by equations in **Figure 3-6**. Total discharge was calculated across a range of recharge values (30%, 50%, and 70%) based on 20-year precipitation records in Cozumel (Weather Underground station IQROOCOZ2) and a 5 x 50 km or 250 km² basin area to provide comparison with previous work.

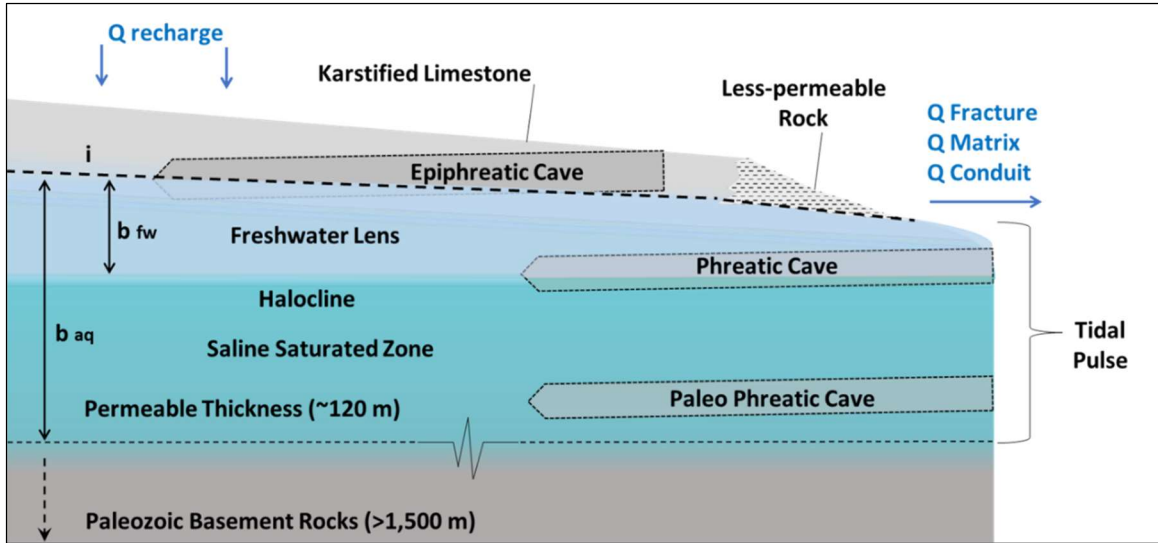


Figure 3-5. Conceptual diagram of the coastal karst system. The current understanding of the aquifer structure assumes that levels of horizontal cave development correspond to past positions of the mixing zone, where the most aggressive dissolution occurs, as sea level has moved over time (Kambesis, 2014; Smart et al., 2006). A relatively thin freshwater lens (b_{fw}) lies above denser saline water and intercepts most known cave systems. Discharge along the coastline occurs via coastal springs fed by conduit flow, with additional poorly constrained discharge via fractures and bedding planes, and many diffuse seeps. Tidal pulse signals propagate through the permeable thickness of the saturated zone (b_{aq}), which could be up to 120 m deep where sea level has moved throughout the Quaternary and resulted in dissolution of carbonate rocks.

Diffusivity (D) is a measure of how strongly and quickly a pressure wave (e.g., a tidal signal) propagates through an aquifer. Diffusivity of a coastal aquifer may be estimated using measurements of tidally driven head variations at the shoreline by:

$$[3.1] \quad D = \frac{\pi x^2}{(\ln E)^2 P}$$

where x is the distance inland, E is the tidal efficiency (tidal amplitude inland/tidal amplitude coastal), and P is the tidal period (Ferris, 1951). The Jacob-Ferris model applies to unconfined aquifers in which tidal range is low relative to thickness of the aquifer (Erskine, 1991). The Yucatan peninsula satisfies this condition, as the average tidal amplitude is about 30 cm, but the thickness of the freshwater lens is 10's of m thick

and the total thickness of permeable limestone is up to 120 m where sea level has been in the past.

Diffusivity in a triple-porosity aquifer reflects the relative contributions of conduits, fractures, and the matrix. The rate at which water recedes in a well can provide an index of the relative importance of each component in a karst system, where distinguishable slope breaks in a recession curve represent changing dominance between these three types of porosity (Shevenell, 1996). Analysis of recession curves is normally applied to discharge volume, but equivalence to head drop was demonstrated by Moore (1992) in the following equation:

$$[3.2] \quad \ln\left(\frac{Y_1}{Y_2}\right) \times \frac{1}{\Delta t} = \ln\left(\frac{Q_1}{Q_2}\right) \times \frac{1}{\Delta t} = \lambda$$

Where, Y1 and Y2 are water levels and Q1 and Q2 are discharge, corresponding to the start and ending values during time interval Δt . λ is the slope of a line tangent to the recession curve. With this equivalence, it is possible to substitute Y for Q in the expression presented by Atkinson (1977) relating discharge to transmissivity (T) and storativity (S), over time t in a groundwater basin with a flow distance of L:

$$[3.3] \quad \log\left(\frac{Q_1}{Q_2}\right) = \frac{T}{S} (t_1 - t_2) \frac{1.071}{L^2}$$

Recognizing that $D = T/S$, this can also be rearranged to solve for D at each slope break:

$$[3.4] \quad D = \log\left(\frac{Y_1}{Y_2}\right) \times \frac{L^2}{1.071} \times \frac{1}{\Delta t}$$

We used a basin area of 5 km x 50 km centered on Sistema Jaguar to permit comparison to previous work in Nohoch Nah Chich (Beddows, 2004). Consequently, L is equal to 50 km minus the inland distance of each site.

Values of diffusivity from recession curves observed in water level data were compared to values obtained from analysis of tidal signals to further constrain spatial distribution of D , and to determine the main pathway of propagation through the aquifer. Transmissivity is given by:

$$[3.5] \quad T = DS$$

Storativity (S) is approximately equal to specific yield in unconfined aquifers, and in limestone this is generally between 0.1 to 0.3 (Lohman, 1972). In fractured limestone, specific yield is approximately 80% of effective porosity (Younger, 1993). Core samples collected in the northern Yucatan show wide range in porosity (5 to 40%) and averaged 22% ($n=71$) (Gonzalez-Herrera, 1984). Assuming that rock in the northeastern area of Quintana Roo is on the high end of this porosity range, storativity is at most 0.3, but may be closer to 0.2 if the estimated relationships between porosity and specific yield hold true.

Hydraulic conductivity (K) is related to transmissivity and aquifer thickness:

$$[3.6] \quad K = \frac{T}{b}$$

where b is the thickness of the aquifer. The total thickness of saturated limestone in the Northeastern Yucatan extends to depths of approximately 1,500 m to volcanic bedrock

(Rodriguez, 1982), but the permeable depth may only be 120 m where the mixing zone has passed with changing sea levels. Prior work has assumed that the effective permeable thickness is restricted to the freshwater lens where the majority of flow occurs via conduits (Beddows, 2004; Martin et al., 2012).

In an ideal coastal system with assumed homogeneity, the thickness of the freshwater lens b_{fw} is proportional to the density difference of fresh and saltwater and is theoretically approximated from the Ghyben-Herzberg relation as:

$$[3.7] \quad b_{fw} = 40i \times x$$

Where i is the hydraulic gradient and x is the distance inland from the coastline. The Ghyben-Herzberg relationship may be broadly applicable to modeling at a regional scale (Gondwe, 2010), but it is of little use at smaller scales due to heterogeneities such as conduits and lithologic or facies changes; the actual thickness of the freshwater lens in eastern Quintana Roo can be up to 50% less than predicted. Beddows (2004) compiled halocline depths in 80 cenotes from field observations and published work to define a strong relationship ($r^2= 0.97$) between distance inland (x in km) and b (m) in eastern Quintana Roo, covering a 100 km stretch of coastline from Puerto Morelos to Tulum and 80 km inland, and roughly centered around Paamul:

$$[3.8] \quad b_{fw} = 1.45x + 9.36$$

Discharge through the matrix (Q_m) was estimated across a range of gradients (0.00005, 0.0001, 0.0005, and 0.001), using Darcy's Law:

$$[3.9] \quad Q_m = Kia$$

Where a is the cross-section area of the porous media portion of the aquifer. A cross sectional area of 100 m^2 was used for purpose of comparison to conduit discharge in Nohoch Nah Chich, where Beddows (2004) directly measured discharge and flow velocities in cross sections ranging from 50 to 210 m^2 .

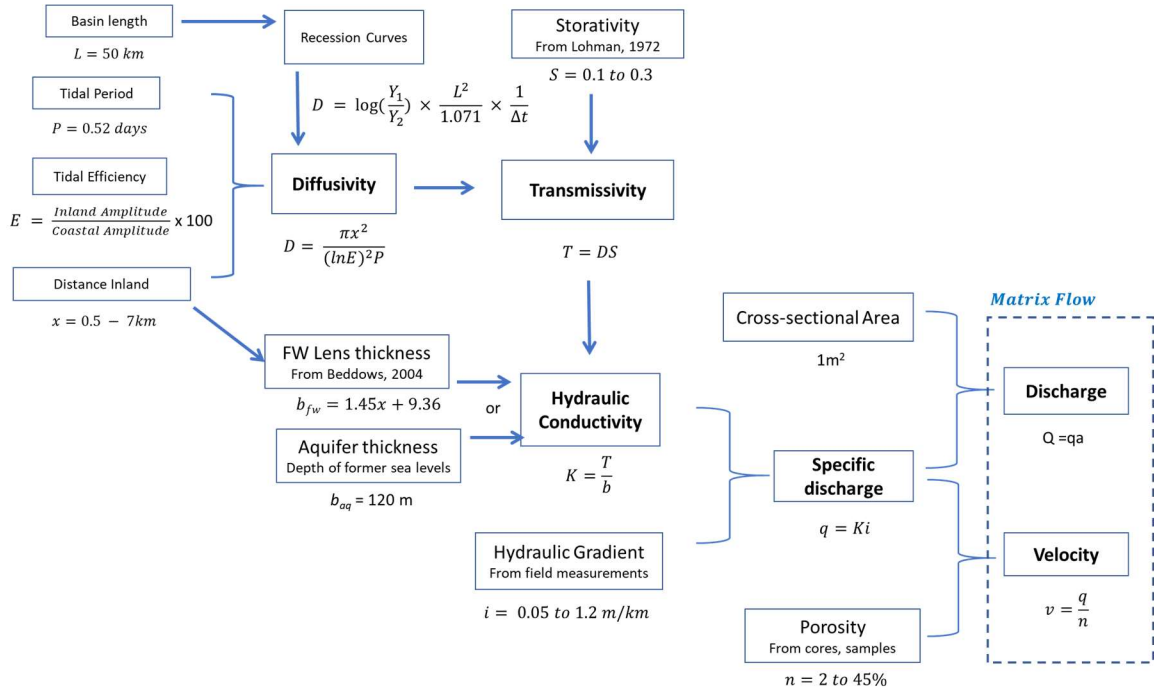


Figure 3-6. Workflow used to calculate hydrogeologic properties. Parameters in bold are calculated across ranges from data collected for this study across and using some assumptions from literature. Except where otherwise noted, equations are standard to hydrology and civil engineering as referenced in Fetter (2001).

3.4 Results

3.4.1 Aquifer properties: D , T , and K

Water level data were analyzed between three coastal reference sites and six inland sites to obtain tidal period (peak to peak or trough to trough time difference) and tidal efficiency (% amplitude attenuation) (**Figure 3-7**). Tidal periods ranged from 0.46 to 0.58 days, averaging 0.50 days. Water level data from Turtle Lake and Jaguar Claw

sites had an average tidal period 0.52 days, which is consistent with the principal lunar component of Caribbean tides (Kjerfve, 1981). Tidal oscillations decreased from 40% at 2.2 km inland, to 31% at 4.7 km, and decreased to <10 % of the coastal signal at >6 km inland, approaching the precision limits of the data loggers (**Figure 3-8**).

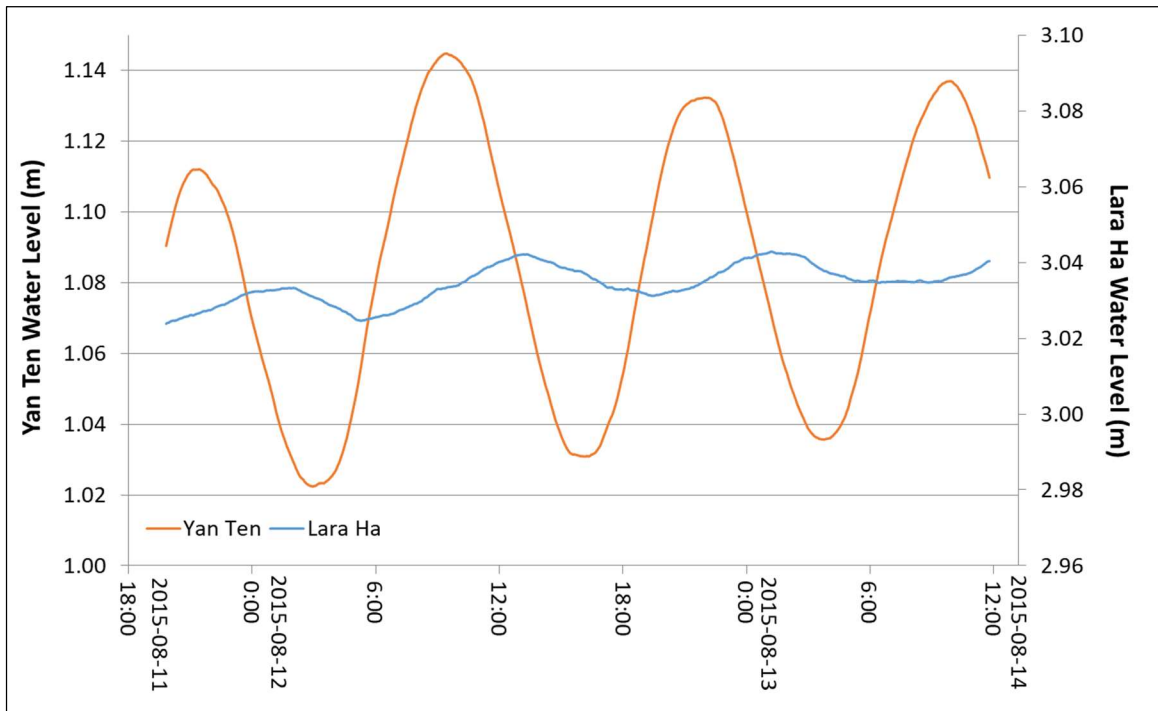


Figure 3-7. Water level data recorded at 1 min intervals on 11-14 August, 2015. Yan Ten (orange line) is a cenote located 70 m from the coastline, and Lara Ha (blue line) is a water level monitoring station in cave passage 5.9 km inland. Tidal period is measured from peak to peak and amplitude attenuation is the difference in peak height between signals at each site.

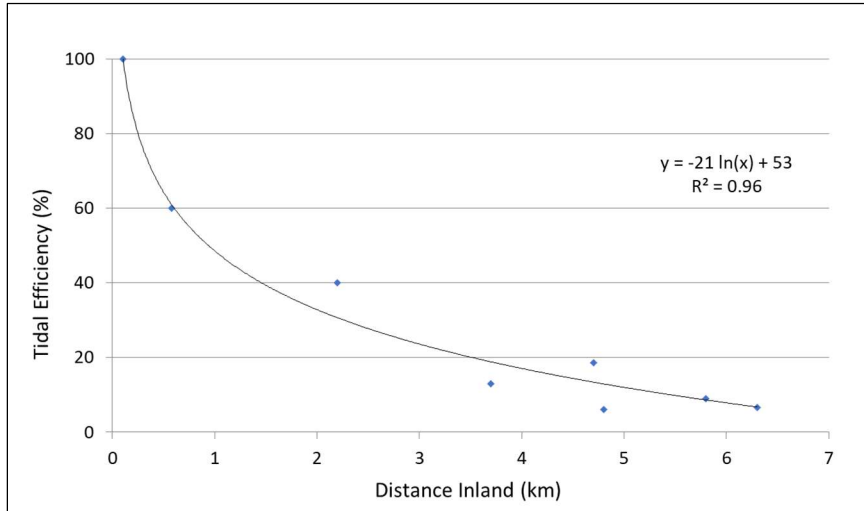


Figure 3-8. Tidal efficiency with distance inland. Amplitude attenuation was calculated relative to a coastal signal measured at Paamul Bay.

Porosity of rock samples from cave passages was generally very high, between 30 and 60%. Rock collected from the surface had very low porosity, from 2 to 7%. **(Appendix B)**. If these values are reflective of variation in regional porosity, then storativity could range from 0.1 to 0.3 across geologic units.

Table 3-2. Summary of diffusivity values by site. Diffusivity was calculated between inland and near-coast sites (rows 1 to 6) and between sites in the same cave system (rows 7 & 8).

Reference Site	Observation Site	Site Distance (km)	Tidal Efficiency (%)	Lens Thickness (m)	D (m ² /day)
Yan Ten	Howling man	2.24	40	11	3.59E+07
Yan Ten	Twisted Sister	3.97	15	12	2.64E+07
Paamul Cenote	Turtle Lake	4.05	31	12	7.22E+07
Paamul Bay	Eden	4.78	6	13	1.74E+07
Yan Ten	Lara Ha	5.85	9	14	3.56E+07
Paamul Cenote	Jagaur Claw	5.92	11	14	4.35E+07
Turtle Lake	Jaguar Claw	5.77	69	13	1.55E+08
Pixan Bel Ent	Pixan Bel Back	6.66	93	17	1.02E+09

Calculated diffusivity between inland sites and coastal reference points was within the same order of magnitude, ranging from 1.74×10^7 m²/day to 7.22×10^7 m²/day. Diffusivity between Turtle Lake and Jaguar Claw in Sistema Jaguar was an order of magnitude higher at 1.55×10^8 m²/day, and diffusivity in Pixan Bel (measured between sensors placed near the entrance and ~1 km farther inland) was the highest at 1.02×10^9 m²/day. Across storativity values from 0.1 to 0.3, transmissivity was proportional to diffusivity, and reflects the same relative differences across sites. Using calculated transmissivity values and estimated aquifer thicknesses, hydraulic conductivity was between 1×10^5 m/day and 1×10^6 m/day for most sites (**Figure 3-9**), with Pixan Bel being the only site where a value of 1×10^7 m/d was calculated.

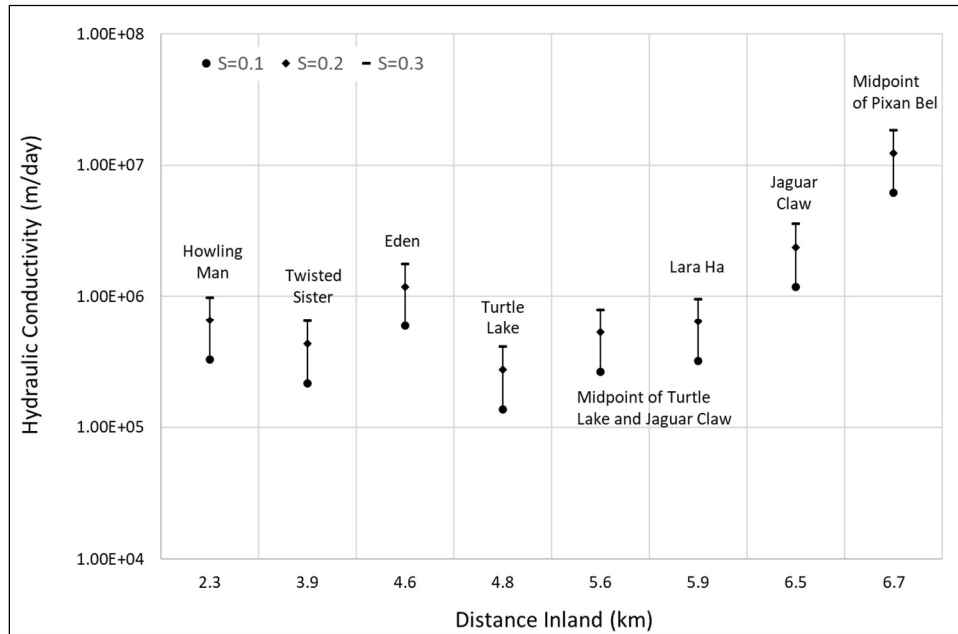


Figure 3-9. Hydraulic conductivity vs distance inland in Sistema Jaguar. Vertical bars show the range of hydraulic conductivity at each site as it varies across assumed storativity values from 0.1 to 0.3.

3.4.2 Hydraulic gradient

Averaged hydraulic head data of similar resolution and duration were used to calculate the hydraulic gradient between sites (**Figure 3-10**). Sites nearer to the coast—Yan Ten and Paamul Cenote— were less than 1 m amsl. Hydraulic head at Howling Man, located 2.2 km inland, was 1.75 m amsl. An increase in head to approximately 3 m amsl was observed at all sites >4 km inland. The gradient flattened out beyond Turtle Lake, with head remaining >3 m amsl.

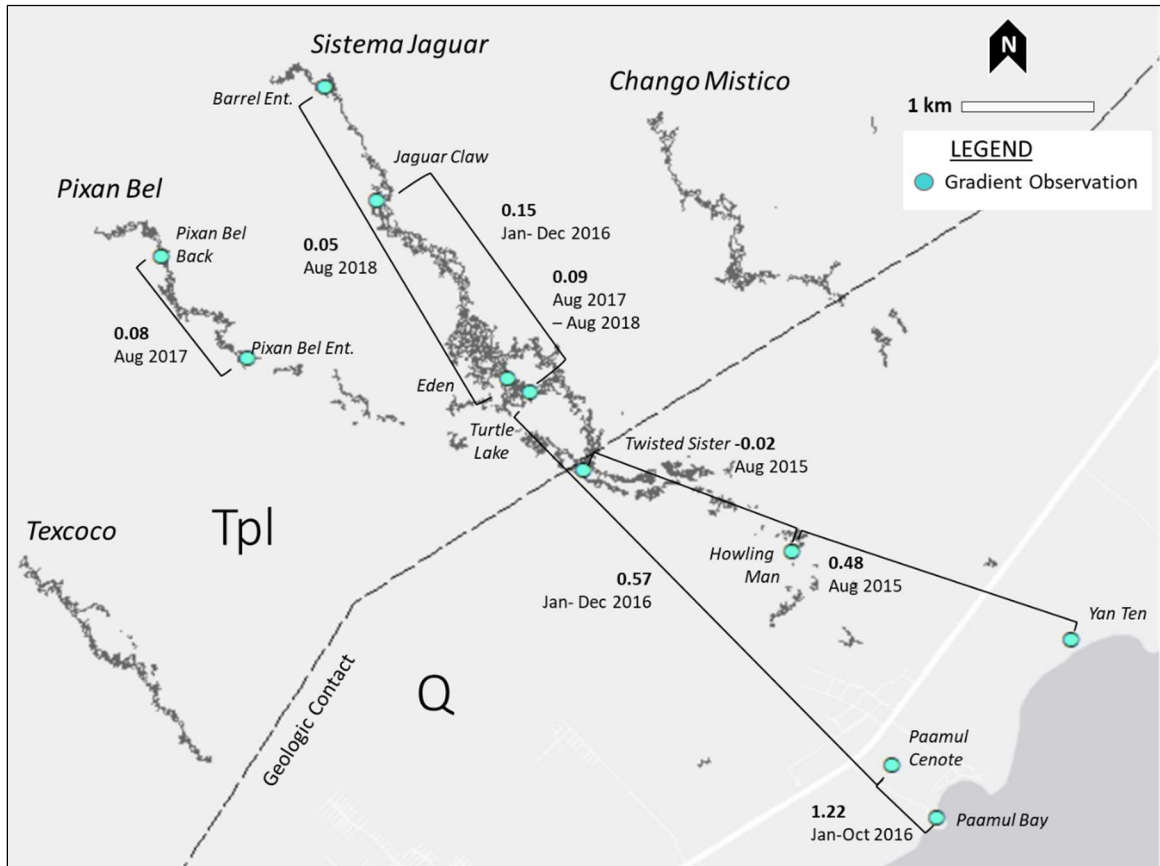


Figure 3-10. Map of the measured coastal hydraulic gradient. Hydraulic gradient was highest near the coastline (>0.5 m/km) and leveled out further inland to 0.05 m/km. Geologic contact data from (Padilla-Sanchez, 2013).

Hydraulic head data indicates that the gradient is steepest closer to the coastline and decreases inland (**Figure 3-11**). The steepest gradient was observed between Paamul Cenote and Paamul Bay (1.22 m/km). Between 0.5 km inland and 4.6 km inland gradients were 0.48 m/km to 0.57 m/km. The gradient flattens to 0.09 to 0.15 m/km up to 6 km inland. Gradients were 0.05 to 0.08 m/km beyond 6 km inland in Sistema Jaguar and Pixan Bel, respectively, both of which contain many km of nearly continuous partially water-filled passages.

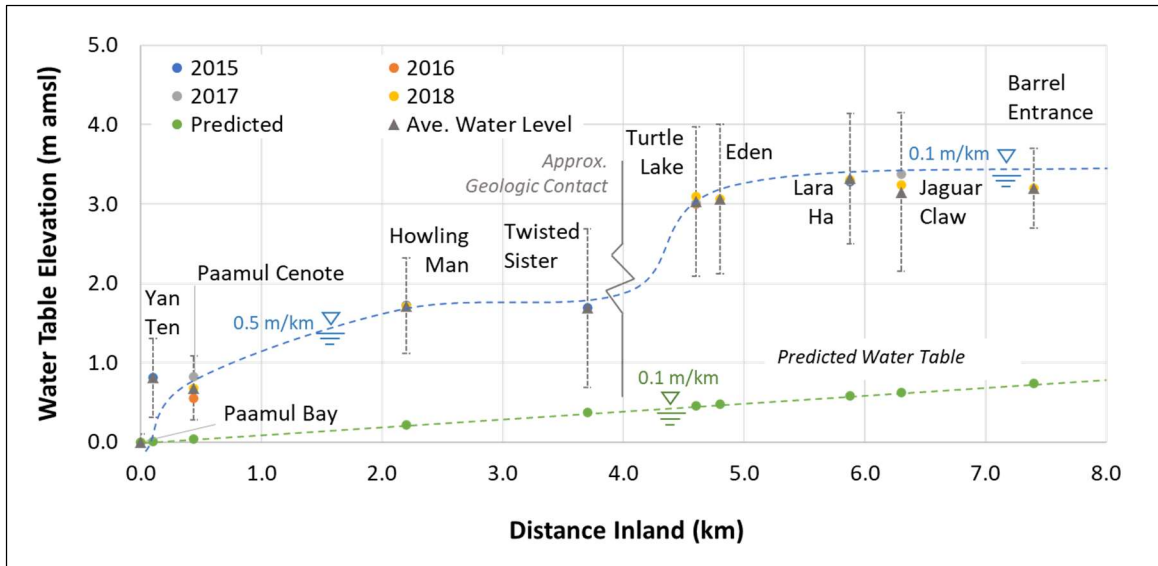


Figure 3-11. Water level elevations from caves and cenotes in the Paamul area. Water elevations close to the coast approach 1 m amsl and rise to over 3 m amsl within cave passage beyond 4 km inland. The points represent GPS-derived elevations at each site. Error bars show the 68% (1σ) vertical radius of the GPS signals at the benchmark to which the observation site was surveyed. The dashed blue line shows the approximate water level elevation from the coast inland. The green dashed line illustrates predicted water table elevations assuming low gradients measured at inland sites (Bauer-Gottwein et al., 2011; Gondwe, 2010; Marin, 1990) do not increase near the coast.

Long-term water level data at three sites (Paamul Cenote, Turtle Lake, and Jaguar Claw) were analyzed for tidal and seasonal variation of the hydraulic gradient (**Figure 3-12** and **Appendix B**). Diurnal signals were consistent with a tidal pulse resulting in gradient fluctuations of ± 2 cm/km (**Figure 3-13**). Gradients between these long-term monitoring sites generally decreased immediately after large rain events, and then rapidly increased, with a total fluctuation of ± 2 to 7 cm/km. The magnitude of response was similar between sites and proportional to the amount of precipitation. Increases in gradients were often observable for several weeks to months following a significant rain event. Between Turtle Lake and Jaguar Claw, the gradient was 0.01 m/km higher during

the wet season. No seasonal difference was detected in the gradient between Turtle Lake and Paamul Cenote.

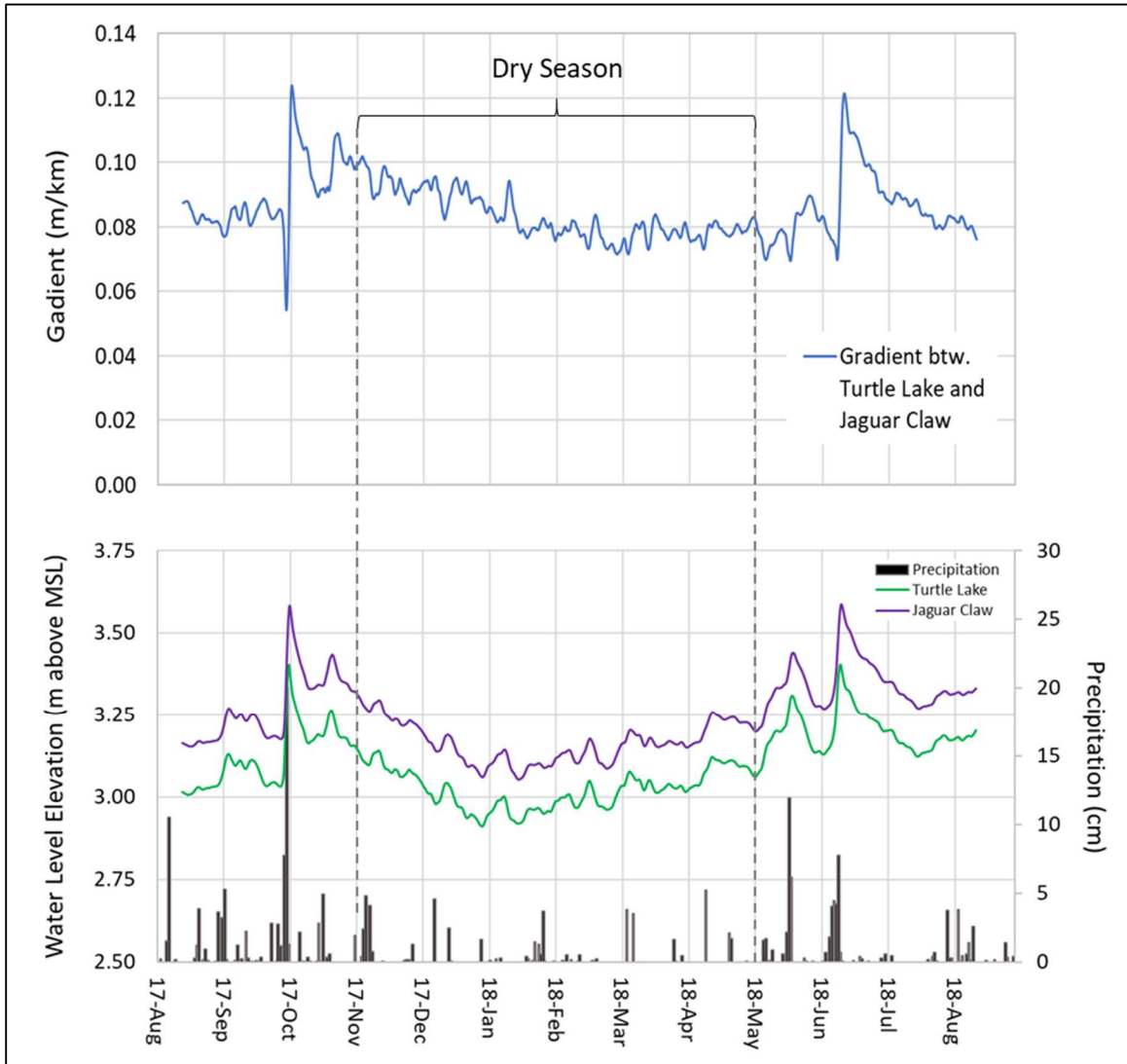


Figure 3-12. Water level and hydraulic gradient response to precipitation. Precipitation data is from a private monitoring station at Under the Jungle dive shop in Puerto Aventuras. The water level peak at 2 October 2017 was a response to Hurricane Nate, and the other peaks in water level were associated with unnamed tropical depressions. Water levels between Turtle Lake and Jaguar Claw show strong responses to precipitation (A) that influenced the hydraulic gradient (B).

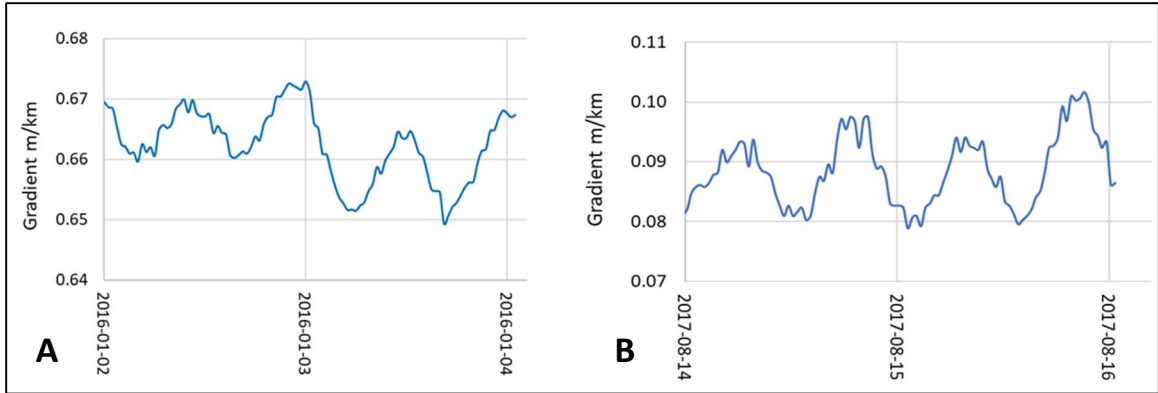
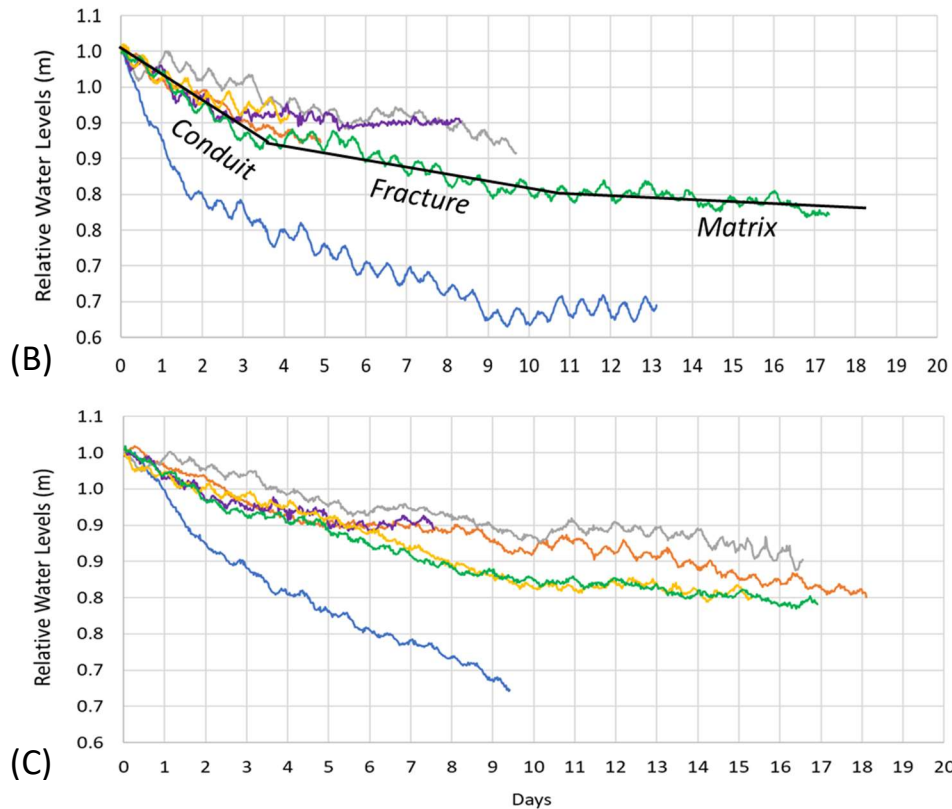
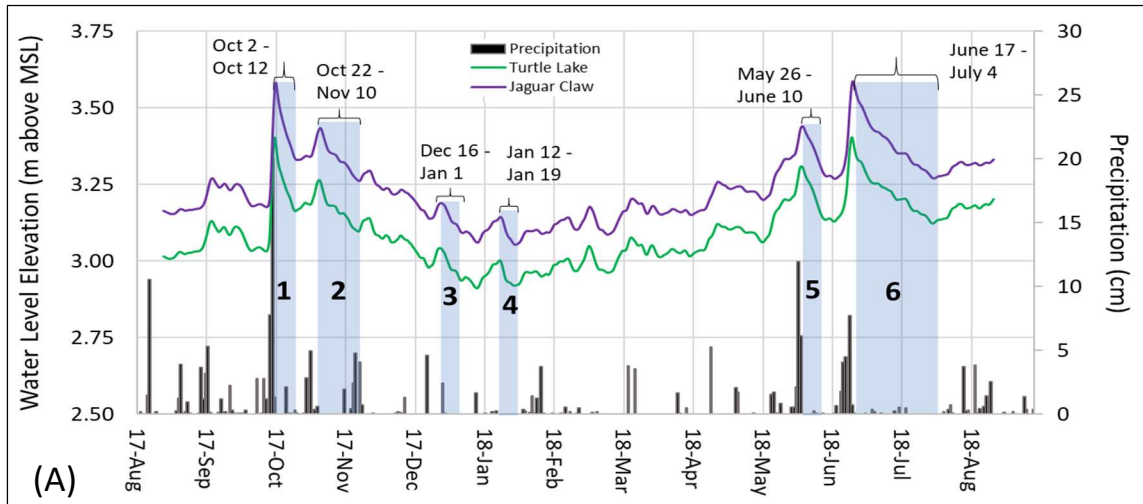


Figure 3-13. Gradient response to tidal signal. Changes in gradient related to tidal periodicity were detectable between sites: Paamul Cenote and Turtle Lake (**A**), and Turtle Lake and Jaguar Claw (**B**).

3.4.3 Recession curve analysis

Six recession curves from rain events in 2017 and 2018 were evaluated for potential diffusivity values representative of conduit, fracture, and matrix components of the aquifer using the method of Shevenell (1996) (**Figure 3-14**). Each event was observed at both Turtle Lake and Jaguar Claw water level monitoring stations 4.6 and 6.3 km from the coast respectively. Larger storm events were reflected by steeper increases and subsequent recessions in water level, more distinct slope breaks, and longer times to return to base flow level. Generally, three slopes were visually distinguishable except where otherwise influenced by additional precipitation. Tidal pulse signals were superimposed on the recession curves but did not obscure the overall trend of each limb.



- Event 1
- Event 2
- Event 3
- Event 4
- Event 5
- Event 6

Figure 3-14. Analysis of stormwater recession curves. Recession curves from six rain events (A) were analyzed to obtain diffusivity values of aquifer components observed ~4.6 km inland at Turtle Lake (B) and ~6.3 km inland at Jaguar Claw (C). The change in slope shown by the heavy black line is interpreted to represent drainage from conduit, fracture, and matrix storage.

Twelve recession limb segments with clearly defined slope transitions were analyzed to obtain diffusivity values. Diffusivity ranged from 1×10^6 m/day to 1×10^8 m/day and varied across one order of magnitude in each of the three assumed storage components (**Figure 3-15**). Hydraulic Conductivity as a function of diffusivity ranges across two orders of magnitude at each site using a range of storativity values from 0.1 to 0.3 (**Figure 3-16**).

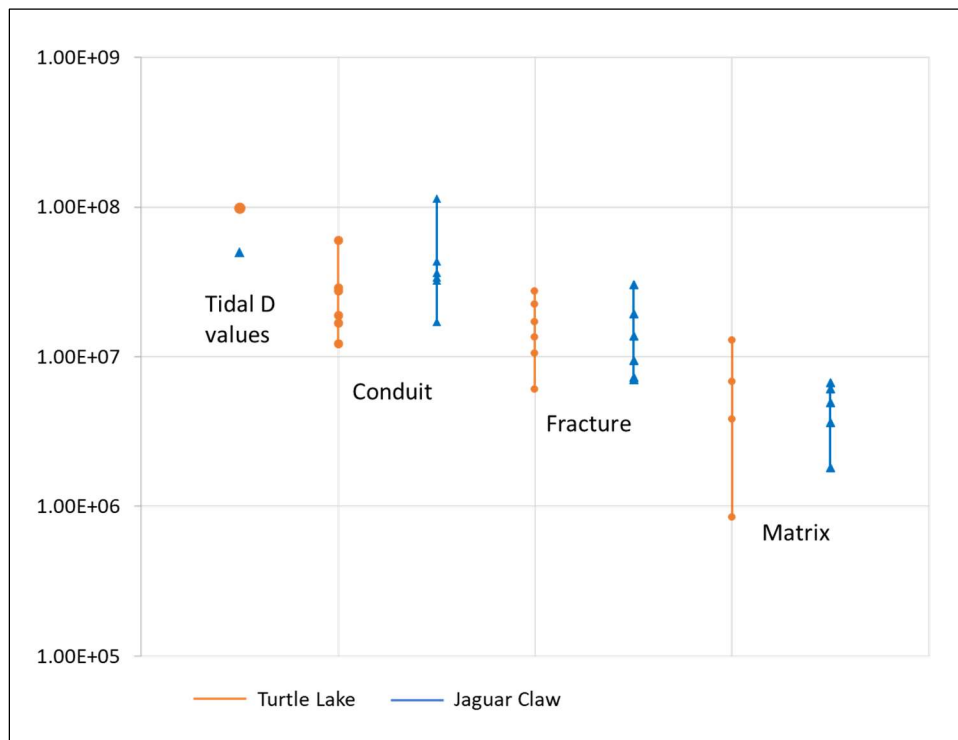


Figure 3-15. Diffusivity values plotted by component type. Diffusivity of components derived from recession limbs at Jaguar Claw and shown in blue, and component values from Turtle Lake are shown in orange. The tidal derived values from long-term water level observations at each site are shown for comparison.

Average diffusivity values derived from the slopes of recession curves were applied to a hypothetical 1 m^2 aquifer cross section with a storativity of 0.3 and a gradient of 0.0001 (10 cm/km) (**Table 3-3**). Results suggest that total discharge was 61% through

conduits, 30% through fractures, and 9% through the matrix. Under these conditions, conduit and fracture flow velocities would be about 250 and 120 m/day respectively, and matrix flow velocities would be less than 40 m/day.

Table 3-3. Diffusivity calculated using storm event recession curves. Transition in slope are interpreted to represent conduit, fracture, and matrix components of the aquifer. Calculations for T, K, and Q use constant storativity (0.3) and gradient (.0001) values.

	D (m ² /day)	T (m ² /day)	K (m/day)	Q (%)
Conduit	3.67E+07	1.10E+07	3.67E+05	61
Fracture	1.76E+07	5.28E+06	1.76E+05	30
Matrix	5.35E+06	1.60E+06	5.35E+04	9

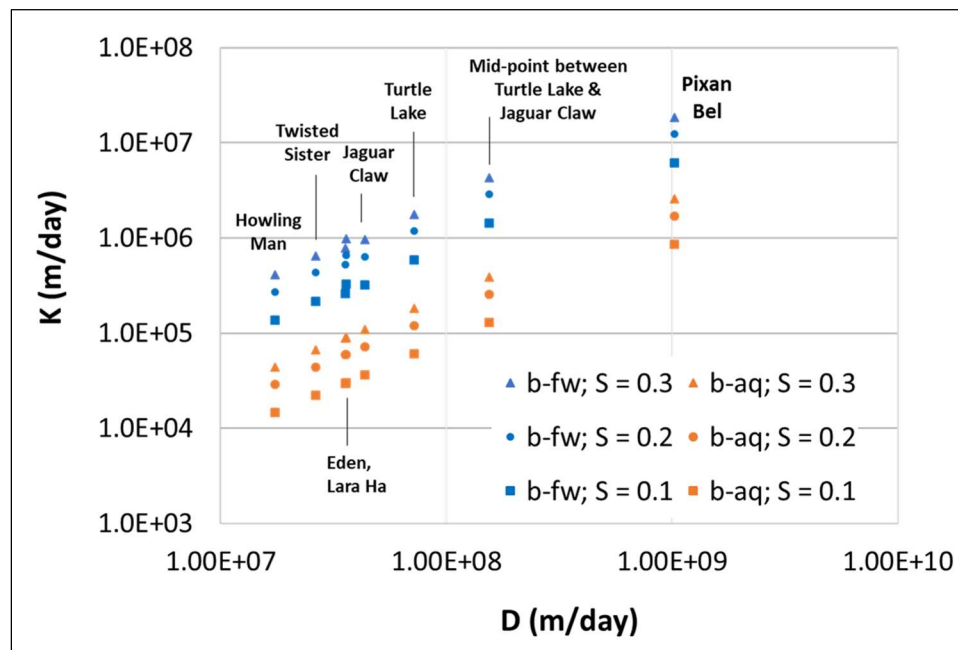


Figure 3-16. A comparison of K and D values across sites. Hydraulic conductivity (K) as a function of diffusivity (D) and aquifer thickness. Comparison of calculated K values at each site using storativity (S)= 0.1 to 0.3 and using aquifer thicknesses equivalent to the freshwater lens (b-fw) and equivalent to the permeable depth of saturated bedrock (b-aq).

3.4.4 Estimated discharge and velocity using tidal-derived D

Discharge was normalized to a 1 m² cross section of rock using previously calculated hydraulic conductivity values, observed gradients, and estimated storativity values based on observations of rock porosity at each site (**Table 3-4**). Calculated discharge at all sites was within the same order of magnitude, ranging from 1.26 x 10² m³/day between Howling Man and Yan Ten, to 6.87 x 10² m³/day between Paamul Cenote and Turtle Lake. Estimated flow velocities ranged from 0.5 km/day between Paamul Bay and Eden to nearly 2.5 km/day in Pixan Bel. Results at most sites were consistent with flow velocities between 1.0 and 1.3 km/day.

Table 3-4. Parameters used to calculate discharge and mean linear velocity. Discharge (Q) was calculated per 1 m² cross sectional area. Velocity (v) was calculated using site-specific values of S, K, and hydraulic gradients between sites.

From	To	Storativity	Gradient (m/km)	K (m/day)	Q (m ³ /day)	v (m/day)
Yan Ten	Howling man	0.10	0.5	3.40E+05	1.26E+02	1256
Yan Ten	Twisted Sister	0.20	0.5	4.32E+05	1.66E+02	864
Yan Ten	Lara Ha	0.30	0.5	7.97E+05	3.07E+02	1048
Paamul Cenote	Turtle Lake	0.30	0.5	1.79E+06	6.87E+02	2349
Paamul Cenote	Jagaur Claw	0.30	0.5	9.68E+05	3.72E+02	1273
Turtle Lake	Jaguar Claw	0.30	0.01	4.38E+06	3.37E+02	1153
Paamul Bay	Eden	0.30	0.50	4.13E+05	1.59E+02	544
Pixan Bel Ent	Pixan Bel Back	0.10	0.01	6.40E+06	2.46E+02	2461

3.5 Discussion

3.5.1 Aquifer properties

Tidal signal amplitude attenuation in Sistema Jaguar was greater than was observed at Nohoch Nah Chich by Beddows (2004). Signal attenuation >5 km inland in Sistema Jaguar approached 90% compared to only about 60% in Nohoch Nah Chich. This suggests that tidal signals in Sistema Jaguar are controlled relatively less by propagation through conduits and more through secondary permeability such as fractures and bedding planes. This is consistent with higher hydraulic heads observed in Sistema Jaguar than in the phreatic conduit systems like Nohoch Nah Chich that are directly connected to large coastal springs.

Highest diffusivity values were observed in Pixan Bel, between sites with nearly continuous partly water-filled cave passage, and the highest diffusivity values in Sistema Jaguar were observed between Turtle Lake and Jaguar Claw, which are also connected by a significant amount of passages that are partly water-filled.

Maximum and minimum calculated K values were constrained by the range of S values used (0.1 to 0.3) (**Table 3-5**). Freshwater lens thicknesses may be underestimates as they are based on observations from the Tulum area where conduit flow is apparently more significant. Lens thickness estimates, arrived at using the formula developed from Tulum-area cenotes, ranged between 12 and 20 m. However, it must be greater in at least one site given our field observation of a completely homogeneous (with respect to T and SC) 30+ m of freshwater vertical profile in an underwater shaft in Chango Mistico. K remained in the same order of magnitude when evaluated across $\pm 30\%$ lens thickness

estimates at each site. Using a permeable depth of 120 m instead of freshwater lens thickness reduced K values by about one order of magnitude.

Calculated D, T, and K values in this study are generally 1-2 orders of magnitude lower than those measured in Nohoch Nah Chich by Beddows (2004). The exceptions are in Pixan Bel and between Turtle Lake and Jaguar Claw, which are more similar to Nohoch Nah Chich, and suggests that signal propagation and flow at these sites are dominated by conduits. Lower values estimated at our other sites are more similar to those calculated for sites in the Bahamas (Martin et al., 2012), which may reflect similarities in rock properties nearer to the coast and/or be more representative of secondary porosity. Similar K values to ours were measured in a geologically young coastal carbonate aquifer in Guam (Rotzoll *et al.* 2013), where aquifer thickness was measured using carbonate thickness above the volcanic basement rock, rather than using the freshwater lens. The lowest K value measured in Guam was in a coastal limestone that has reduced permeability as a result of re-cementation (or “case hardening”).

Table 3-5. Comparison of coastal karst aquifer properties from other studies. Shaded values were calculated using data in original publications for the purpose of comparison.

Source	Site	FW lens (m)	Permeable Aquifer (m)	Diffusivity (m ² /d)	Transmissivity (m ² /d)	K- FW lens (m/day)	K-perm (m/day)
Beddows, 2003	YP region					3.00E+07	
	Balam Kan Chee	4	120	3.68E+08	1.10E+08	2.76E+07	9.17E+05
	Heaven's Gate	9	120	1.82E+08	5.46E+07	6.35E+06	4.55E+05
	Far Point station	10	120	1.77E+08	5.31E+07	5.31E+06	4.43E+05
Martin et al., 2012	Bahamas	10	120	3.00E+05	1.30E+06	3.00E+06	1.08E+04
	Blue holes Bahamas	10	120	7.60E+05	7.69E+07	2.94E+06	6.41E+05
Rotzoll et al., 2013	Mariana	10	180	3.80E+05	1.14E+05	1.14E+04	6.33E+02
	Barrigada	10	140	3.30E+07	9.90E+06	9.90E+05	7.07E+04
	Argillaceous	10	130	4.50E+06	1.35E+06	1.35E+05	1.04E+04
This Study	Howling man	11	120	3.59E+07	1.08E+07	9.82E+05	8.98E+04
	Twisted Sister	12	120	2.64E+07	7.93E+06	6.48E+05	6.61E+04
	Turtle Lake	12	120	7.22E+07	2.17E+07	1.76E+06	1.81E+05
	Eden	13	120	1.74E+07	5.23E+06	4.08E+05	4.36E+04
	Lara Ha	14	120	3.56E+07	1.07E+07	7.86E+05	8.91E+04
	Jagaur Claw	14	120	4.35E+07	1.30E+07	9.55E+05	1.09E+05
	TL to JC mid pt	13	120	1.55E+08	4.64E+07	3.57E+06	3.86E+05
	Pixan Bel mid pt	17	120	1.02E+09	3.07E+08	1.85E+07	2.55E+06

Storativity in the Yucatan aquifer is not well constrained, but estimates fall within the range of values measured in other highly porous and permeable karst systems. In the Biscayne Aquifer of southeast Florida, which is within a Pleistocene to Pliocene aged reef limestone, storativity was calculated using regional-scale drawdown of a canal ranged from 0.05 to 0.57, with an average value of 0.15 (Bolster et al., 2001). Porosity of laboratory tested samples of the Edwards Limestone ranged from 0.06 to 0.15, which would be consistent with storativity values ranging from 0.05 to 0.12.

3.5.2 Hydraulic gradient

The greatest uncertainty in this study derives from difficulties related to obtaining precise measurements of water table elevations. Barometric pressure differences were too small and variable to be reliable, and a high-quality GPS signal was difficult to obtain through thick jungle vegetation cover. USGS global elevation data (GMTED 2010)

available from ESRI (Danielson & Gesch, 2011) and a LiDAR-derived DEM (INEGI, 2017) with inferred 0.5 m contours were used for cross-comparison to identify elevation values that were reasonably in agreement across sources. Elevations obtained using GPS at Paamul Bay, Paamul Cenote, and Howling Man agree with these other available data sources. The elevations of Yan Ten and Barrel Entrance were inferred from the LiDAR DEM. The elevations of Eden and Lara Ha were determined by high-precision GPS allowed to log for more than 2 hours. The benchmark elevation at Eden was also used to establish water level elevation Turtle Lake, via in-cave survey, because the sites are close to one another. Jaguar Claw and Twisted Sister were not close to an entrance where GPS could be used, and therefore cave survey data was also used to connect them with the nearest reference point.

We established water table elevations of over 3 m amsl within 5 km of the coastline, which is significantly higher than was expected from reported regional measurements of the hydraulic gradient in the Yucatan Peninsula (Bauer-Gottwein et al., 2011; Gondwe, 2010; Marin, 1990). Maximum water table elevation for the peninsula has been argued to be only 4 m amsl in Lake Esmeralda, ~30 km inland near the Sian Ka'an Biosphere Reserve, using a first-order INEGI survey line (Perry et al., 2002).

The extremely low gradients of <10 cm/km measured at several sites across the Yucatan Peninsula suggest that the water table should be less than 1 m amsl within 1 km of the coastline. However, these measurements were either along known phreatic conduit flow paths (Beddows, 2004) or were inland and did not extend to reach the coast (Gondwe, 2010; Marin, 1990; Moore et al., 1992). In all cases, a coastal outflow face is required where the bottom of the freshwater lens must be below sea level to allow for

discharge (Palmer, 2007), and a steepening of the gradient must occur in order to allow discharge rates to be maintained through a smaller cross-sectional area of freshwater lens. Our determination of relatively steep gradients of ~ 1 m/km within ~ 0.5 km from the coast is therefore reasonable in the absence of known phreatic conduits and coastal springs in the study area, and the lower gradients of <10 cm/km at distances beyond 4 km inland are comparable to previous studies (Back & Hanshaw, 1970; Beddows, 2004; Gondwe et al., 2010; Marin, 1990; Moore et al., 1992) (**Table 3-6**).

Table 3-6. Gradient measurements from prior work.

Source	Site	Gradient (m/km)
Gondwe, 2010	Sian Ka'an	0.03 to 0.07
Beddows, 2004	regional	0.06
	Ponderosa	0.04 to 0.05
	Naranjal	0.06 to 0.09
Moore, 1992	Quintana Roo	0.15 to 0.2
Marin, 1990	Quintana Roo	0.07 to 0.01
Back & Hanshaw, 1970	Yucatan	0.02

Relatively high gradients measured near the coast in this study suggest that local differences in geology can exert considerable influence on flow dynamics. A change in gradient occurs between 2 and 5 km from the coast, which appears to coincide with a geologic contact mapped by INEGI at ~ 4 km inland, which is near the Twisted Sister site. Rock samples from closer to the coastline have lower porosity, and it is probable that a change in facies to younger and less permeable rock acts as a hydrogeologic dam, which contributes to steeper gradients, except in locations where phreatic conduits lowers the gradient.

3.5.3 Recession curve analysis

Diffusivity values calculated from recession curves include assumptions about aquifer geometry that are not well-constrained, including an assumed basin boundary that lies 50 km inland. Because of this, direct comparisons with diffusivity values determined from tidal pulses propagating from the coast inland need to be made cautiously as they may not represent the same types of flow. Tidal-derived diffusivity values at Turtle Lake and Jaguar Claw were both relatively high and plotted within the range of the conduit flow diffusivity values that were calculated from recession curves. This suggests that tidal pulses may preferentially follow conduit flow paths into the interior of the aquifer, where they are then secondarily transmitted to the measurement sites via fractures and the matrix. Nevertheless, all of these values are an order of magnitude lower than what was measured in Nohoch Nah Chich (Worthington et al., 2001), which is consistent with less conduit connectivity in Sistema Jaguar.

Analysis of recession curves allows us to investigate differences between what we interpret as being conduit, fracture, and matrix effects. The relative proportion of conduit (61%), fracture (30%), and matrix (9%) flow contrasts with previously reported proportions of 99% conduit and 1% matrix (Worthington et al., 2001). The fracture and conduit flow velocities of 119 and 247 m/day respectively, calculated with a storativity of 0.3 and a gradient of 10 cm/km, are on the lower end of the 200 to 2,700 m/day that was measured using dry traces in Nohoch Nah Chich (Beddows, 2003). Hydraulic conductivity values of fracture and matrix components, 1.76×10^5 and 5.35×10^4 m/day respectively, are four orders of magnitude higher than what was calculated by Worthington, Ford, and Beddows (2000) using well data from Yucatan State. These large

differences suggest that the aquifer components interpreted from the recession curves may in fact reflect three scales of conduits and fractures, rather than true fracture or matrix components. Pump tests in monitoring wells near the study site are warranted to be certain of the hydrogeological interpretation of changes in recession curve slope.

3.5.4 Implications for the water budget

Applying site-specific storativity and gradient values per 1 m^2 cross sectional area resulted in an average discharge of $2.96 \times 10^2 \text{ m}^3/\text{day}$ (excluding Pixan Bel and Jaguar Claw as conduit-dominated sites), or $1.08 \times 10^7 \text{ m}^3/\text{year}$. For comparison to previous work (**Table 3-1**), a maximum potential discharge assuming a groundwater basin 5 km wide and 50 km inland, with annual precipitation of 1293 mm/yr and a recharge rate of 17% (Gondwe et al., 2010) would be $1.21 \times 10^7 \text{ m}^3/\text{year}$, or $0.38 \text{ m}^3/\text{s}$ per km of coastline.

A central question that remains to be answered in the Yucatan Peninsula is the contribution of matrix and fracture and bedding plane flows to total coastal discharge, in contrast to the more obvious coastal conduit discharge. Previous work in Nohoch Nah Chich indicated that groundwater flow rates through the conduit system were at least 1, but approaching 2 orders of magnitude greater than the matrix flow rates, with matrix flux being $\sim 1\%$ of the total, even though 97% of the groundwater volume is stored in the matrix porosity (Worthington et al., 2001). Notably, a substantial portion of coastal groundwater discharge has been shown to be entrained seawater or water exchanging from the ocean as hydraulic gradients reverse during large recharge events; some coastal springs reportedly discharge water with up to 75% marine salinity (Worthington et al., 2001). Water exchange between epiphreatic cave pools and the larger groundwater

system, where there are no direct connections to underwater conduits, is assumed to represent flow through the matrix. This exchange could be vertical or horizontal movement between water table pools in caves and either a regional matrix flow system, or an as-yet undiscovered underlying and hydrologically active conduit network.

3.6 Conclusions

Applied studies tend to describe aquifers as either 1) poorly developed karst systems with large amounts of matrix storage, or 2) well-developed karst aquifers with large conduits and low matrix storage (Atkinson 1977; Bonacci 1993; Padilla *et al.* 1994; Panagopoulos & Lambrakis 2006); large storage capacity phreatic reservoirs in highly karstified limestones, such as those of the Yucatan, are understudied and not classified (Stevanović, 2015). A more realistic model considers that aquifers exist along a continuum and may exhibit a mix of conduit, fracture, and matrix flow (Worthington *et al.*, 2001). The descriptive and quantitative work presented in this study provides insights that will support future modeling of heterogeneous coastal karst aquifers that are both high in storage and have large and extensive conduit systems.

The results of this research suggest that region-scale models are inadequate to describe geologic and hydrologic heterogeneity at a sub-basin scale. The conceptual model of flow primarily occurring through conduits needs to be revised to accommodate a triple porosity aquifer with approximately 60% conduit, 30% fracture, and 10% matrix flow. Geologic properties influence the rate of groundwater flow, and this becomes apparent where the hydraulic gradient steepens at the coastline. Additional work is needed to more accurately measure the hydraulic gradient, which will require precise surveys from a benchmark at sea level to cenotes and cave pools.

4. EVIDENCE OF UPLIFT IN THE YUCATAN PENINSULA USING EPIPHREATIC INTERFACE DEPOSITS (EID) AS SEA LEVEL PROXIES: QUINTANA ROO, MEXICO

Abstract

Epiphreatic Interface Deposits (EID) in caves are thought to form where CO₂ outgasses at the water table and calcite precipitates in a band representing seasonal and tidal water level ranges. In low-gradient coastal karst systems, EID elevations provide a proxy for sea level at the time of deposition, which can be established using Uranium-Thorium (U-Th) dating methods. Stalactites within EID provide evidence of vadose conditions during the time of their deposition and therefore constrain the age of the cave passage. We obtained U-Th ages of 26 EID and 32 internal stalactites from three caves in the northeastern Yucatan Peninsula, a region assumed to have remained tectonically stable since the late Pleistocene (Szabo et al., 1978). The caves are thought to have formed at their present elevations during late Pleistocene high stands that occurred 120-125 ka, 325- 330 ka, and 405- 415 ka BP (Kambesis & Coke, 2013). Samples were collected from 2.8 to 7.5 km inland at approximately 1 to 12 m above modern sea level. EID dates ranged from 4.24 ± 0.03 ka to 397 ± 19 ka BP. Calcite coatings on stalactites below the water table ranged from 1.51 ± 0.19 ka to 2.36 ± 0.09 ka BP. Interior stalactite ages range from 0.19 ± 0.01 ka to 646 ± 125 ka BP. All sample ages correspond to times of lower sea level. Differences between modern sample elevations and former sea-levels provide evidence of cumulative uplift. Our data indicate that these caves formed >600 ka BP and therefore formed ~100 m lower than their present elevation, and that this portion of the Yucatan Platform has uplifted at rates of ~329 mm/ka since at least 250 ka BP.

4.1 Introduction

The Caribbean coastline of Quintana Roo is known for its extensive underwater (phreatic) cave systems, typically with near-horizontal conduits and abundant speleothems that formed during lower sea levels. Nearly 1,500 km of phreatic passage has been mapped since exploration by cave divers began in the 1970's (QRSS, 2019), and this likely represents only a small fraction of the total existing conduit length. Most scientific work has focused on phreatic caves because of the abundance of data provided by explorers and neglected similarly extensive caves that exist at or above the water table (epiphreatic and vadose caves, respectively). However, since 2010 speleologists have now mapped >330 km of epiphreatic and vadose cave systems within 10 km of the coastline— sometimes connected with phreatic conduits— and much more remains to be surveyed (QRSS, 2019). Access to caves across a range of elevations and hydrogeologic settings provides an opportunity to obtain new data to refine sea level records and test hypotheses of speleogenesis.

Caves in the Yucatan Peninsula are thought to develop via mixing dissolution at the halocline (Back et al., 1986; Smart et al., 2006) that is presently observed at 10 to 30 m below sea level within 10 km of the coastline. Cave elevation should therefore reflect the position of past mixing zones, which will correlate with past sea levels (Kambesis, 2014). A review of Quaternary sea level records indicates that sea level has been 80 to 120 m lower than most known caves and has been an average of 40 m lower during the late Pleistocene when the known conduits are assumed to have formed. If the current understanding of speleogenesis in carbonate platforms is correct, and bedrock solubility is similar throughout the strata, then this suggests that extensive caves should also exist at

depths similar to average Quaternary sea levels. Deep cave exploration is limited by the challenges of technical SCUBA diving; however, there is little evidence of extensive deep cave development equivalent to that found at shallower depths, and the few known deep caves terminate in collapsed passage (Fred Devos, pers. Communication).

4.1.1 **Geologic setting**

The Yucatan Peninsula is the emergent portion of a larger carbonate platform that extends northwest into the Gulf of Mexico, where it is known as the Campeche Bank (**Figure 4-1**). The eastern submerged margin of the platform extends less than 10 km from the coastline before dropping to depths of >400 m in the Yucatan Basin east of Cozumel (Ward et al., 1985). The entire platform is part of the Maya Block of the North American Plate, located to the north of the Motagua and Polochic Fault Zones, which separates it from the Chortis block that collided with it during the late Cretaceous, 100 to 66 Ma (Lodolo et al., 2009; Marroni et al., 2009). Associated regional scale faults and structural features align northeast-southwest across the peninsula and extend into the submerged platform margins. Fractures parallel to the Caribbean coast are understood to be related to a horst-and-graben block fault system, of which the island of Cozumel is thought to be a part, although no field data have yet confirmed this (Ward et al., 1985). The portion of the Yucatan Peninsula north of the Ticul Fault, a north-dipping normal fault, is considered a subunit of the Mayan tectonic block and is thought to have been stable since at least the late Pleistocene (Mann, 2007).

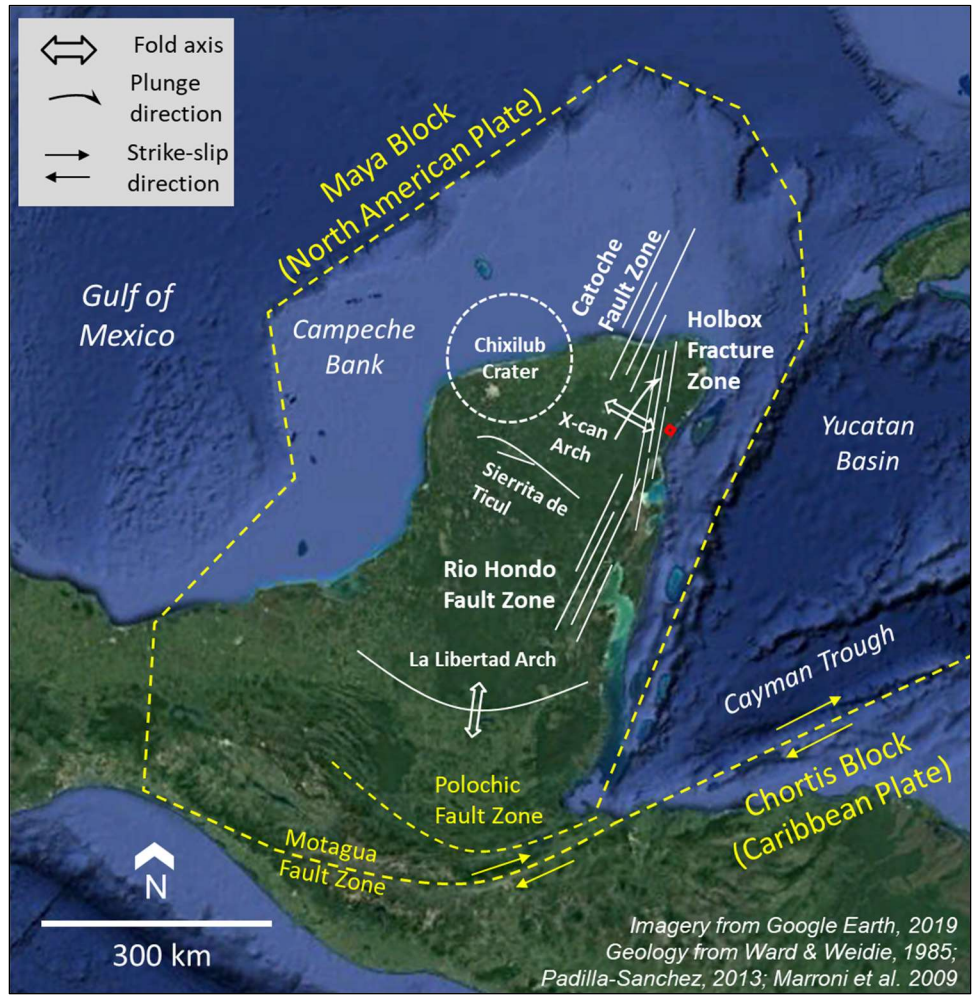


Figure 4-1. Structural features of the Yucatan Peninsula. The study area is outlined in red. The north eastern coastline contains three zones of normal faults that continue offshore. The Chicxulub crater is shown by the dotted white line. The extent of the carbonate platform comprising the Maya block, part of the North American Plate is outlined by the yellow dashed line. The Maya block borders the Chortis block, part of the Caribbean plate, along a strike slip fault in the Cayman Trough.

4.1.2 Karst landscape evolution

Mixing dissolution is well established as the dominant mode of speleogenesis in coastal karst settings (Back et al., 1986; Ford & Williams, 2007; Mylroie & Carew, 1990; Smart et al., 1988), and it is thought to be the means by which the large, maze-like phreatic conduits in Quintana Roo, Mexico have formed (Smart et al., 2006). There is

recent work that emphasizes the role of CO₂ generated by microbial activity, but this also appears to occur coincidentally with the halocline where organic material accumulates at the density boundary (Gulley et al., 2016a; Haukebo, 2014; McGee, 2010). Epiphreatic, and most vadose caves, in the study area are thought to have developed under phreatic conditions during times of higher sea level and subsequently drained (Smart et al. 2006). The result is a multi-level complex of overlapping conduits that should reflect elevations of former halocline positions relative to past sea levels (**Figure 4-2**).

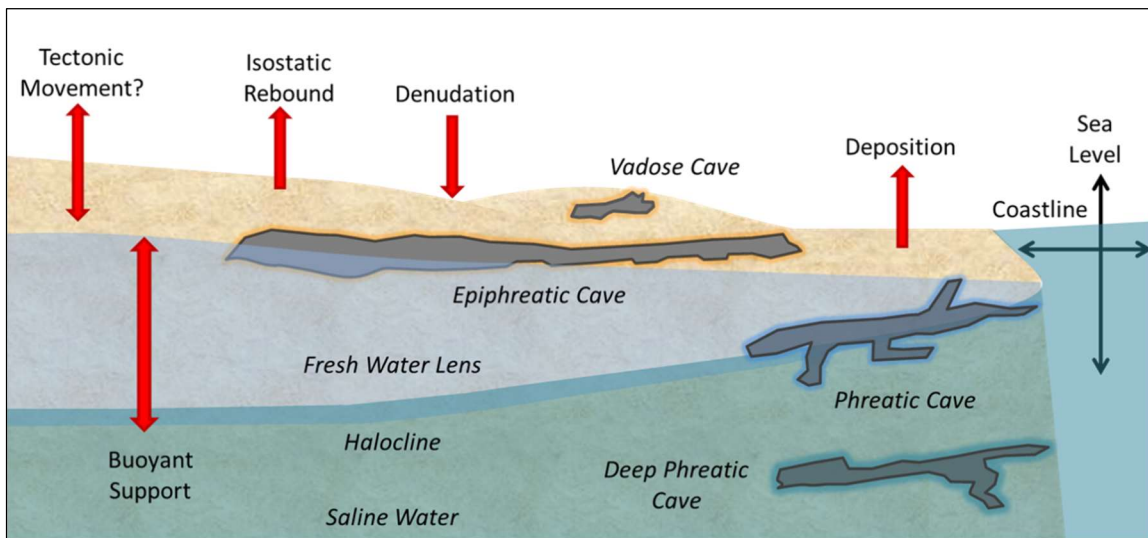


Figure 4-2. Conceptual cross-section of coastal karst in Quintana Roo, Mexico. Cave formation is understood to occur most readily along the halocline, where fresh and saline water mix. This zone moves vertically with changing sea level and laterally with coastal deposition, resulting in levels of cave development. The red arrows represent geologic processes that potentially contribute to vertical displacement.

In addition to a rise or fall in sea level, exposed land surface elevation reflects the cumulative effects of tectonic forces, buoyant support, denudation, rebound from mass loss, and deposition. Generally, these additional factors are not considered in coastal karst conceptual models either because of complexity, lack of data, or oversight. Tectonic forces are assumed to be negligible in the Yucatan Peninsula as the platform is thought to

have remained stable since at least the last Pleistocene. This assumption is based on the U-Th ages (120-125 ka) of six fossil coral samples collected at 2 to 4 m amsl that were in general agreement with the elevations of fossil coral of similar age elsewhere in the Caribbean, and interpreted to represent a reef crest during the last glacial high-stand (Szabo et al., 1978). The role of buoyant support has been considered for cave passage collapse (Smart et al., 2006), but not necessarily for vertical displacement of the land mass. Isostatic rebound is often discussed in relation to the melting of continental glaciers but it can also result from erosion and mass loss via dissolution both within the rock and at the land surface (Woo et al., 2017). Flank margin caves, which develop at sea level along carbonate island coastlines, have been used reliably as sea level indicators (Myroie & Carew, 1988; Myroie & Myroie, 2009), but recent work indicates that denudation and uplift can produce misleading vertical relationships (Myroie et al., 2018).

4.1.3 Uncertainties in sea level history

Global sea level records derived primarily from ice and ocean sediment cores (Miller et al., 2005) indicate that sea level has been an average of 40 m lower than present during much of the Pleistocene, which is the approximate age of the limestone in which caves in the study area formed (Padilla-Sanchez, 2013). Sea level has also been higher than present, but only for brief periods from 115 to 125 ka ago. For about 50% of the past 2 Ma, sea level has been between 20 and 50 m lower than present (**Figure 4-3A**). If caves are assumed to be a reliable indicator of sea level history, this presents a conflict because most explored conduits are within 20 m of modern sea level (**Figure 4-3B**) (Kambesis, 2014), rather than at lower elevations where sea level has been for the majority of the platform's geologic history. The expected depth of conduits would

actually be lower than former sea levels because the greatest dissolutional enlargement occurs in the fresh water- saline mixing zone, which is presently observed at depths 1:20 ratio to the thickness of the freshwater lens, or 10-20 m near the coastline and >80 m in the platform interior (Marin et al., 2016). Even though observations may be biased by physical limitations of cave diving, significant conduit networks have not been documented at greater depths despite decades of effort searching for them.

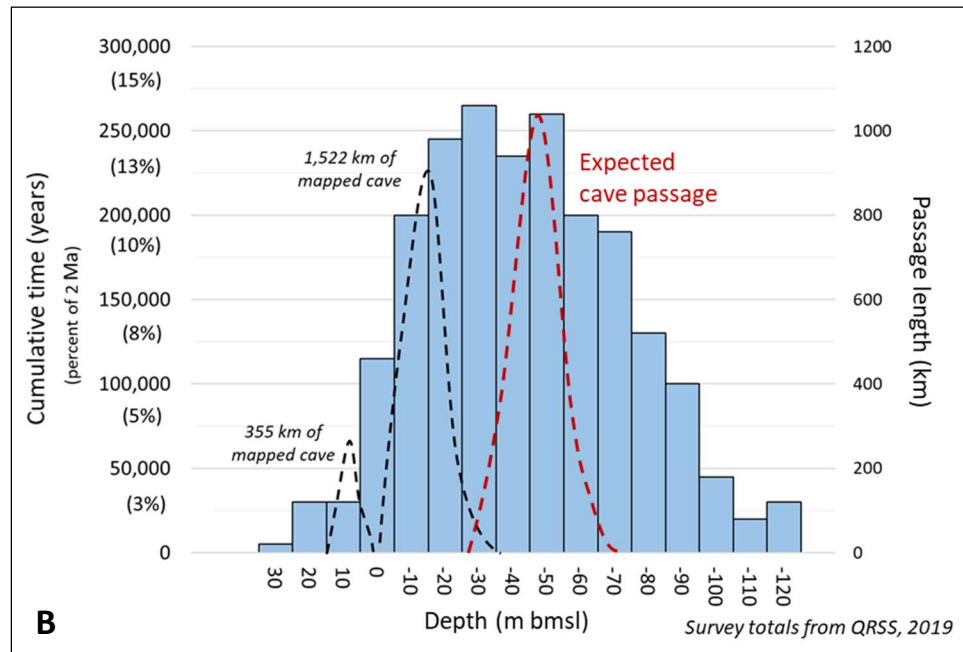
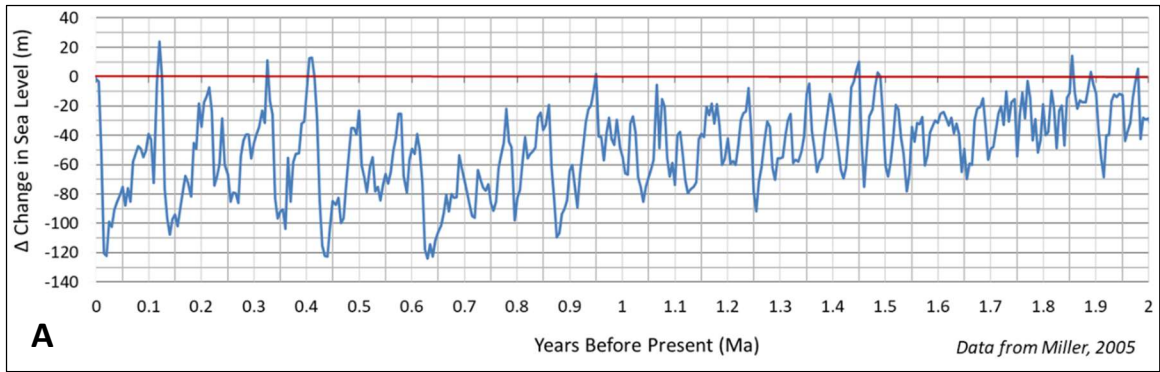


Figure 4-3. A comparison of past sea levels and observed cave elevations. **(A)** Sea level curve (Miller, 2005) for the past 2 Ma. Sea level has been much lower than present for most of the past 2 Ma, with the exception of a few relatively brief high stands. Most cave development would be expected to occur between 40 and 60 m below modern sea level, based on the position of past mixing zones relative to changing sea level. **(B)** A histogram of the depth distribution of former sea levels and mapped cave passage. The dashed black curves highlight the range of depth where nearly all known cave passage lie in the phreatic and vadose zones. The greatest volume of phreatic cave passage occurs at 8 to 12 m below modern sea level, and the greatest volume of vadose and epiphreatic cave passage occurs at 3 to 12 m above sea level (Kambesis, 2014). Expected cave passage, shown by the red dashed curve, is approximated as corresponding to the depth of the mixing zone at former sea levels.

Sea level reconstructions from ocean sediment cores use $\delta^{18}\text{O}$ values as temperature proxies to remove the temperature dependent fractionation effect from $\delta^{18}\text{O}_c$ in order to solve for the $\delta^{18}\text{O}$ of seawater ($\delta^{18}\text{O}_{sw}$) (Spratt & Lisiecki, 2016). Similarly, ice core $\delta^{18}\text{O}$ values serve as a proxy for temperature and snow accumulation that can be linked to global climate patterns using inverse ice volume models; however, the spatial range of this information is limited and depends on skillful modeling of the proxy data within the reconstruction process (Steig, 2008; Steiger et al., 2017). Both sea sediment and ice cores are sensitive to local conditions that vary with the distribution of sea ice, ocean currents, and precipitation. Sources of uncertainty in models include: the input oxygen isotope record, seasonality of temperature forcing, the temperature– $\delta^{18}\text{O}$ relationship in precipitation, the atmosphere–deep-water temperature relationship, and the isotopic contributions from Antarctica and Greenland (Bintanja et al., 2005). Elevation uncertainties in records derived from ice and ocean sediment cores can be as great as ± 20 m (Miller et al., 2005). Bintanja et al., (2005) reports sea level uncertainty of ± 12 m for their inverse ice model based on data from 57 global sampling sites. Due to a time lag between isotope signatures and global changes in climate, millennial-scale fluctuations may be obscured in the record (Arz et al., 2007).

Precise radiometric dates of coral provide an important control on sea level because their relatively rapid growth rates constrain the timing of sea level change, and their sensitivity to water depth can constrain the amplitude of fluctuations. However, there are a number of factors to consider in the interpretation of coral data: 1) pristine, *in-situ* samples are difficult to find prior to ~ 120 ka BP, particularly during low stands (Medina-Elizalde, 2013; Spratt & Lisiecki, 2016); 2) coral is susceptible to “open-

system” incorporation of U from seawater while submerged (Thompson et al., 2003); 3) only a reef crest species with a very limited depth range can be used as a precise proxy for relative sea level elevation (Blanchon & Shaw, 1995); and, 4) vertical displacement from tectonic and/or isostatic movement are often not known (Blanchon et al., 2009).

Uncertainties in coral-based records are also related to paleo-depth of growth of corals, and possible diagenesis of the fossil corals since their deposition (Scholz & Mangini, 2007). For example, shallow coral species used as indexes can tolerate depths of up to 40 m, creating a wide margin of error for short-duration high stands (Fricke & Meischner, 1985). A coral record preserved at or near modern sea level may have actually been deposited as much as 40 m below modern sea level and since uplifted. Further bias derives from the use of different decay constants, selection criteria for suitable and unsuitable corals, and the unknown U-isotopic composition of past seawater (De Waele et al., 2018).

4.1.4 **Speleothems as age records and sea level proxies**

Most isotopic work has focused on stalagmites because they are slow-growing and provide a more robust and consistent record of age or climate. Stalactites, in contrast, are often small, fragile, and are more likely to fall and break under their own weight. Stalactites also begin their growth as a hollow “soda straw”, which results in the oldest ages in the rim of the stalactite and the youngest where calcite deposits eventually filled the center. This does not mean that stalactites cannot be used for age records, but rather that one must be cautious to sample in the calcified rim of the stalactite away from the hollow center to measure the oldest age. Stalagmites and stalactites both provide proxies

for times when a cave passage was filled with air and able to permit CO₂ to outgas from water, but their elevations are not directly related to sea level.

Other formations that are deposited at the water table can be used as proxies for sea level elevation. For example, Phreatic Overgrowths of Speleothems (POS) are “lion-tail” shaped calcite deposits on cave formations—usually stalactites—occurring in caves located within the tidal zone. The vertical extent of these deposits corresponds to the tidal amplitude in their depositional environment. Assuming no tectonic activity, their elevation relative to sea level in a modern setting therefore provides a precise indicator of former sea levels. U-Th dating of POS has been used to evaluate sea level history in the tectonically stable island of Mallorca, Spain (Dorale et al., 2010; Polyak et al., 2018; Tuccimei et al., 2006; Vesica et al., 2000), and also in Cuba to estimate uplift rates (De Waele et al., 2018).

Similarly, secondary calcite deposits can accumulate on speleothems, walls or other hard surfaces in epiphreatic cave pools farther inland. These develop a characteristic bell-shape as layers of calcite accumulate outward along the surface within the seasonal and tidal ranges of the water table. We use the acronym Epiphreatic Interface Deposits (EID) as a descriptive term for calcite crusts deposited over speleothems at the water table (**Figure 4-4**). These are distinguished from POS by their morphology, geochemical conditions of their depositional environment, and higher elevation related to hydraulic gradients. While not equivalent to sea level, EID formations at the precise elevation of the water table provide a proxy for sea level in low-gradient systems.

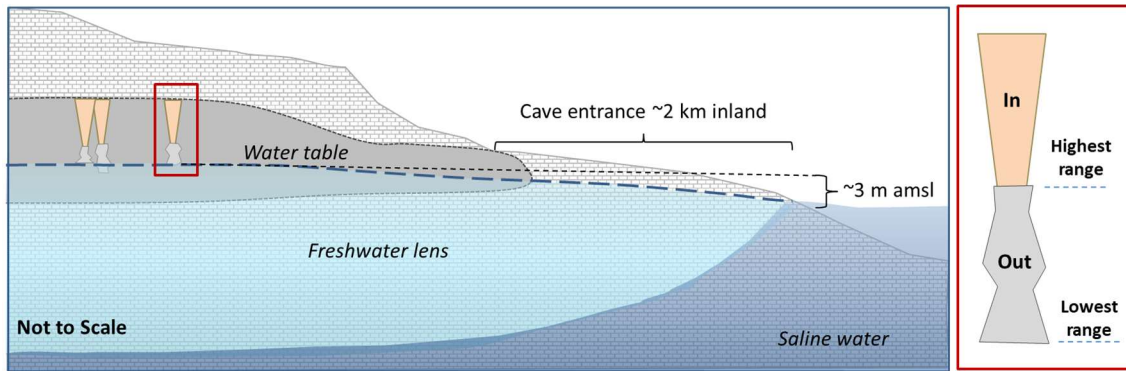


Figure 4-4. A conceptual diagram of Epiphreatic Interface Deposits (EID). Inset outlined in red depicts secondary calcite deposition over a stalactite occurring within the seasonal and tidal range of the water table.

Research Objectives

This research provides insight into both speleogenesis and tectonic history of the Yucatan Peninsula. We tested the hypothesis of rapid and recent speleogenesis in a tectonically stable platform by using U-Th ages of cave formations to constrain the age of conduits, and by comparing the ages and elevation of Epiphreatic Interface Deposits to Atlantic Sea Level records (**Figure 4-5**).

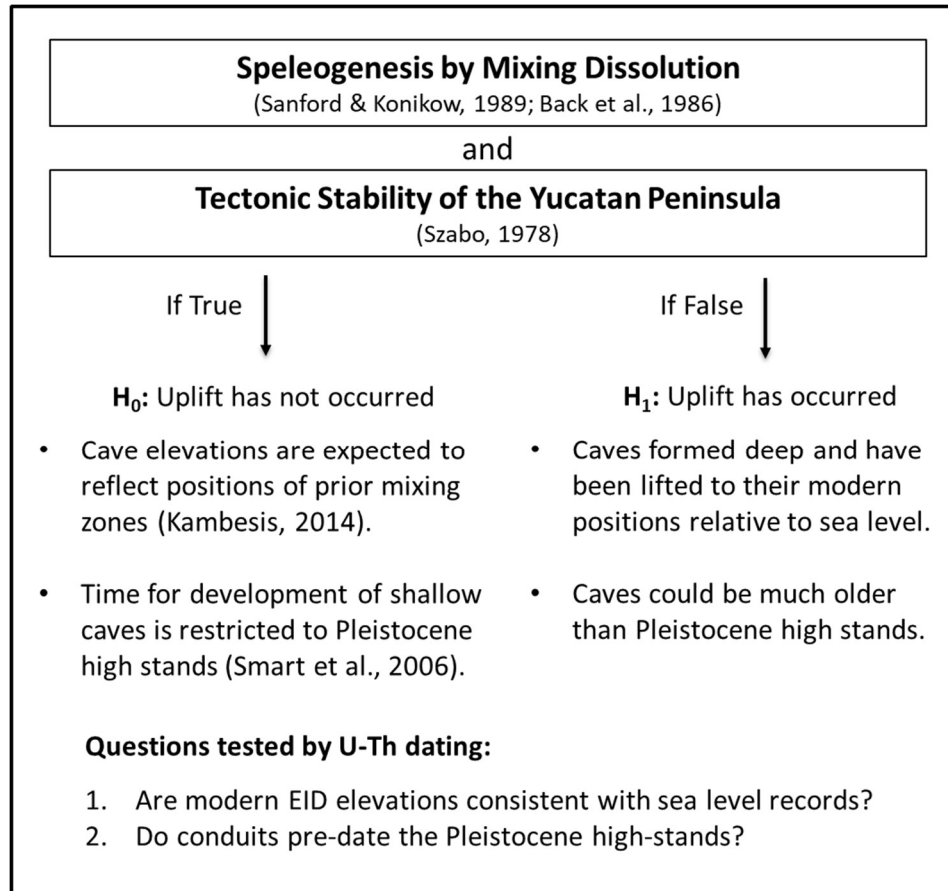


Figure 4-5. Assumptions examined in this research. Competing hypotheses are addressed by research questions and tested by U-Th dating of speleothems.

4.2 Methods

4.2.1 Study site

The study site is located near Paamul approximately 70 km south of Cancun, Mexico. This area contains large and extensive shallow epiphreatic and vadose cave systems perpendicular to the coastline and extending from about 2 to 10 km inland. More than 300 km of these passages have been mapped in the study area since 2008 and much more remains to be surveyed. Cave passages generally consist of maze-like networks

near the coast, but farther inland they coalesce into very large (>40m wide by 10 m high) conduits, often containing extensive pools of water 1 to 5 m deep (**Figure 4-6**).



Figure 4-6. Examples of cave passage in Sistema Jaguar. Maze-like passage with a few shallow pools and many collapsed entrances occur at the southern end of the cave closer to the coastline (**A**) (photo: Lorena Martinez), and converge to wide, singular passage with nearly continuous pools of water from ~5 to 7 km inland (**B**) (photo: Benjamin Schwartz).

Surface geology in the study area is mapped as Pliocene limestone and coquina with Pleistocene to Holocene reef rock and shallow marine deposits within 4 km of the coastline (INEGI, 1997). Coral heads in the upper Pleistocene formation have been dated to 125 ka BP (Szabo et al., 1978), which correlates to the last high stand at 6 m above modern sea level. However, very limited detailed geological mapping has been done at the surface in this region, and uncertainty remains regarding where and how facies change, vertical extents of formations, and exact locations of contacts between these presumed formations. No roads exist 5 to 40 km inland of the study site, and access to subsurface geology is almost entirely limited to exposures in caves and a few quarries ~2 km from the coast. Although caves provide access to the subsurface, the geology exposed in them may not be regionally representative due to the fact that conduit locations are usually controlled by geologic heterogeneities and form along the most hydraulically efficient flow path.

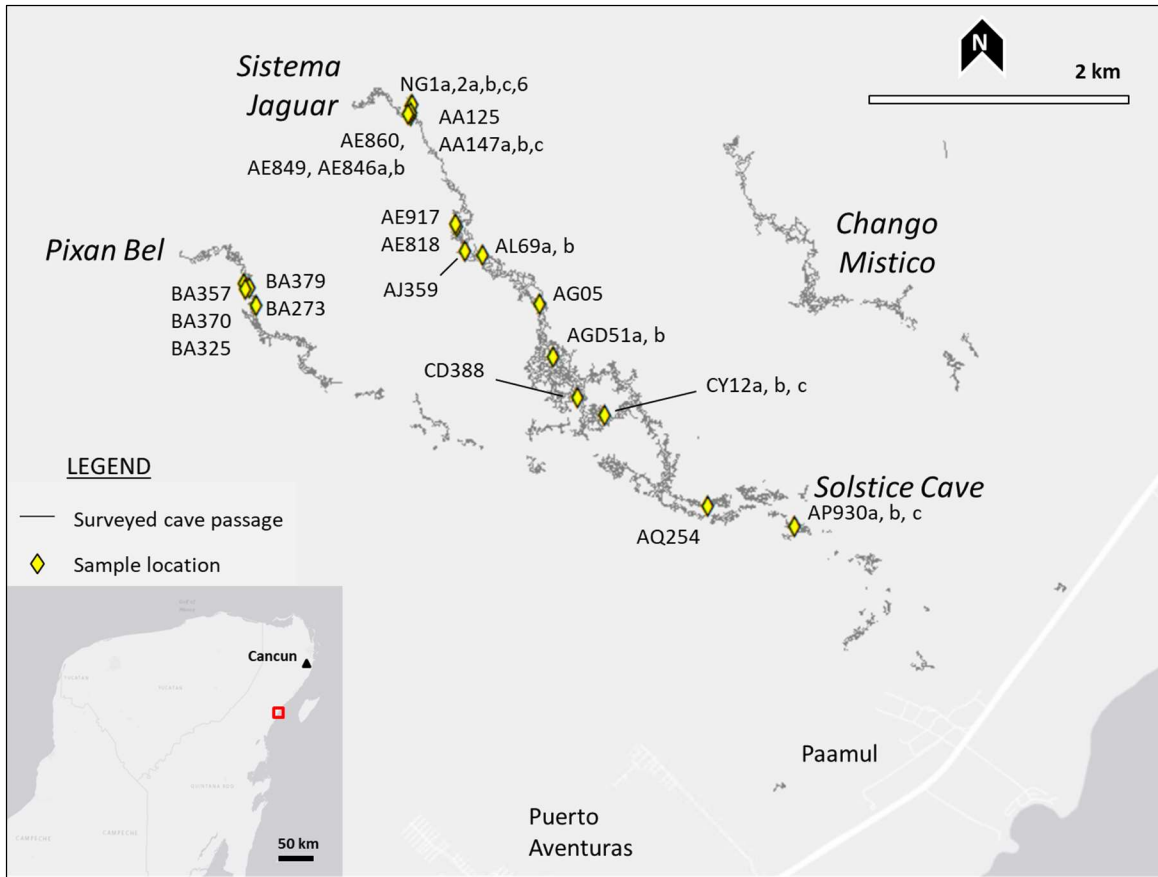


Figure 4-7. Map of the study area. The study area is near Paamul, approximately 70 km south of Cancun (inset). Surveyed cave passage is shown by the gray lines. Thirty-two samples were obtained from eighteen sampling sites (yellow diamonds) in Sistema Jaguar, Pixan Bel, and Solstice Cave. Pools of water occur at approximately 3 km inland, and continuous water begins just south of sample AL69.

4.2.2 Sample collection

Samples of EID on stalactites were collected in three related caves at sites ranging from 2.8 km to 7.5 km from the coastline (**Figure 4-7**). Samples were packaged individually in plastic bags to avoid cross-contamination. Each sample site was located by a survey that tied into the main cave survey line using handheld Suunto survey instruments ($\pm 0.5^\circ$ azimuth and $\pm 0.5^\circ$ inclination) and/or a Leica DistoX laser tool (± 0.2 cm, $\pm 0.5^\circ$). Direct measurements to determine elevation above the water table were also

taken at sample locations where samples were above the water table (**Figure 4-8** and **Figure 4-9**). Cave survey data were georeferenced by surveying to benchmarks on the surface near four entrances. Benchmark locations and elevations were established using high-precision GPS (Trimble Geo7x with Tornado antenna, capable of ± 1.5 cm horizontal and ± 2 cm vertical accuracy), post-processed with 15 sec differential correction referenced to a UNAVCO Station in Puerto Morelos (TGMX; 20.8681 N, -86.8669 W). Elevations at benchmarks were also compared to a LiDAR-derived 5m DEM overlain with interpolated 0.5 m contours.

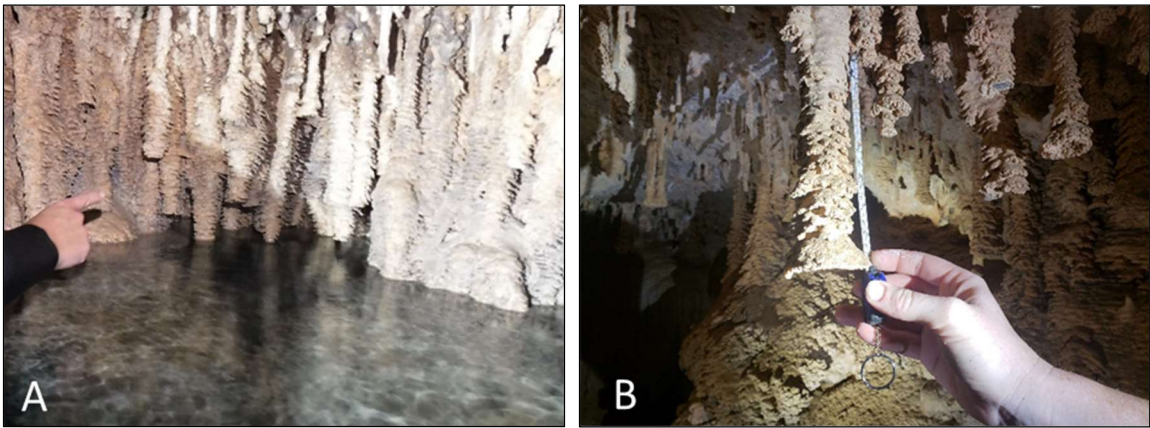


Figure 4-8. Examples of EID *in situ* in cave passage. Samples were collected at the water table (**A**) and from passage walls or ceilings (**B**). Several samples were collected underwater (not shown).

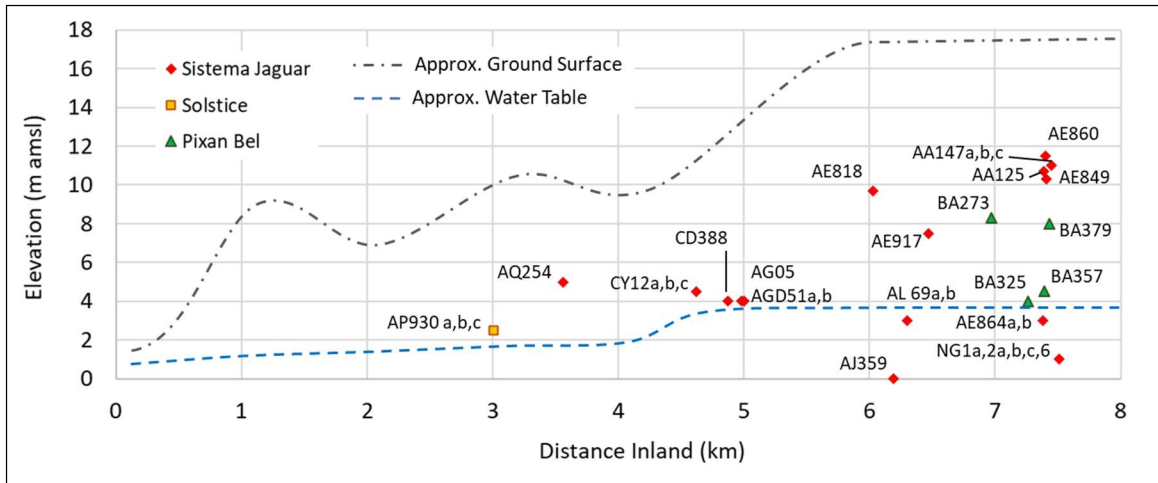


Figure 4-9. Speleothem sample elevations. Sample elevations are shown relative to the modern water table (dashed blue line) and the approximate land surface elevation based on LiDAR data (dashed gray line). Sample numbers correspond to the nearest in-cave survey station. Water table elevations are estimated to be ~3 m amsl in Sistema Jaguar and Pixan Bel, and ~1.5 m amsl in Solstice Cave nearer to the coastline. Elevation data from INEGI (2017).

Samples were collected during four field seasons between December 2015 and August 2018. The highest elevation sample (AE860) was collected from the ceiling in the far northwestern end of Sistema Jaguar and surveyed to the water table as well as to the surface through a nearby entrance. The sample from the lowest elevation (AJ359) was collected by a diver at 3 m below the water table, which is approximately equivalent to sea level. Several samples collected by divers at the far north end of the cave appeared to be modern spar growth occurring underwater. The samples were included in analysis with EID as they provide a reference near modern sea level. A piece of flowstone (AQ254) was also sampled for analysis with the interior samples because it also represents deposition above the water table. This sample was collected from about 5 m amsl on a breakdown boulder in the southern part of the cave away from any water-filled passage. Samples from Solstice cave, a cave containing only 1 km of mapped passage

located in a ridge about 3 km inland, were collected from a wall about 1 m above a pool close to the entrance of the cave. Samples from Pixan Bel were collected from 1.5 to 6 m above the water table.

4.2.3 Sample preparation and laboratory analysis

Small fragments or calcite powder obtained using a dental drill were removed from EID layers and interior stalactites. Some speleothems were cut to more clearly expose internal structures prior to laboratory sampling (**Figure 4-10**). Fragments and powder samples were cleaned twice in an ultrasonic bath to remove any sediment prior to preparation for analysis. U-Th dating was performed on fragments and powder samples using multi-collector inductively coupled plasma mass spectrometry (MC-ICP-MS) at the University of Minnesota using a ThermoFisher Scientific Neptune XT. Laboratory methodology followed ICP-MS procedures described by Cheng et al. (2013).

Both EID and stalactites are composed of very thin concentric layers of growth (**Figure 4-11**), which means that some samples were a composite sample of several layers, despite attempts to drill from a single layer. Unlike stalagmites, stalactites initiate as hollow soda straws that grow as water flows through them and precipitation of calcite occurs along the outer edge. The interior soda straw becomes inactive during dry periods or when it is submerged and resumes activity when conditions are favorable. Eventually, most soda straws become clogged with precipitated calcite, which results in relatively young deposits occurring in the center of the stalactite. This could happen at any time in relation to EID deposition. Therefore, the oldest interior dates should be obtained from the growth layers around the central soda straw rather than at the center. Secondary calcification (recrystallization) occurring during times of submergence can skew

laboratory results, and therefore it is necessary to be certain that laboratory samples are obtained from a single EID layer that represents its primary depositional conditions. This can be evaluated by closely examining speleothem thin sections.



Figure 4-10. Close-up of a speleothem with EID coatings. A slice of EID from sample AE849 was taken for U-Th analysis (A). Top of the speleothem is to the left. The sample was cut to expose the interior stalactite with a central hollow “soda straw”, and the coatings of EID (B). Powder for U-Th analysis was taken from the areas outlined in black.

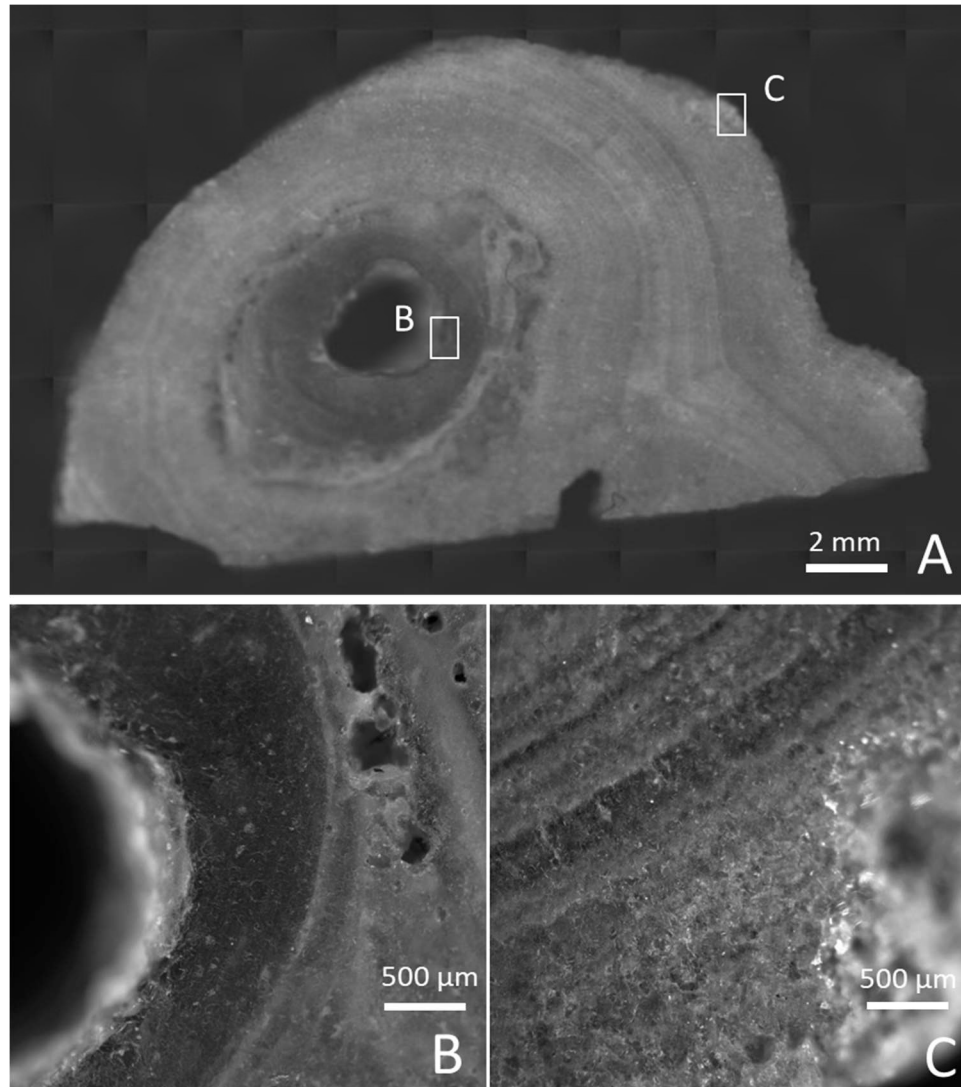


Figure 4-11. A reflective scanned image of a slice of EID. The lower image shows a cross-sectional slice from sample BA273 around an interior stalactite (A) (x4 magnification). Note the stalactite is a hollow “soda straw”, and precipitation at this stage occurs around its rim (B). The bands represent phases of mineralization deposited on the exterior when the interior stalactite was at the water table (C). (Photos: Dale Barnard, Thor Laboratories, Austin, Texas).

The MC-ICP-MS method measures the ratio of ^{238}U (4.5 Ga half-life) to the decay products ^{234}U (246 ka half-life), ^{234}Th (245.25 ka half-life), and ^{230}Th (75.34 ka half-life) to determine the age of a sample (Cheng et al., 2000; Cheng et al., 2013). The sensitivity of the age error to uncertainties in the initial $^{230}\text{Th}/^{232}\text{Th}$ ratio decreases with

increasing initial U concentration, increasing age, and decreasing detrital contamination (Dorale et al., 2004). Under ideal conditions, MC-ICP-MS dating precision of 2σ increases with sample age as follows: 10 ka $\pm 0.1\%$, 130 ka $\pm 0.08\%$, 200 ka $\pm 0.15\%$, 400 ka $\pm 0.5\%$, and 600 ka $\pm 2.0\%$. Given the exponential trend of uncertainty with sample age, this method is considered reliable up to about 400 ka BP, beyond which 2σ error is generally greater than ± 2 ka.

Because virtually all rock in Quintana Roo is carbonate (Ward et al., 1985), there is a very low probability that additional U accumulates through weathering of other source materials. However, red clayey soil occurs in some low-lying areas and comprises the floor of some cave passages, and this sediment likely originates as windblown Saharan dust, which contains detrital grains of volcanic minerals. Sample contamination is therefore possible if trace amounts of U in volcanic grains are incorporated into calcite lattices during deposition where clayey soil has been redeposited by infiltrating water. The most likely source of contamination is via handling or cross-contamination between samples during transport.

4.3 Results

Thirty-two samples from three caves were analyzed, resulting in 26 U-Th ages for EID, and 32 for internal stalactites (**Table 4-1**). Interior stalactite ages range from 0.19 ± 0.01 ka to 646 ± 125 ka. EID dates ranged from 4 ± 0.03 ka to 397 ± 19 ka. Calcite spar deposited underwater was also sampled with dates ranging from 1.51 ± 0.19 ka to 2.36 ± 0.09 ka. All correspond to times of lower sea level. All dates are shown in comparison with mid-Atlantic sea level records for the past 450 ka (**Figure 4-12**).

Table 4-1. U-Th ages from speleothem samples and their collection elevations. Elevations above mean sea level were approximated as the surveyed distance from the measured elevation of the water table in each cave. The naming convention uses the survey station closest to the collection point of the sample, followed by a letter designating an individual speleothem, followed by IN or OUT and a number that tells where a laboratory sample was taken from the speleothem.

Cave	Sample	Type	Approx. Elev (m)	Age (ka)	Error (ka)
Solstice <i>3 samples</i>	AP930a-IN	stalactite	3	110.28	0.74
	AP930a-OUT	EID	3	103.27	0.72
	AP930b-IN	stalactite	3	212.45	2.15
	AP930b-OUT	EID	3	171.77	1.14
	AP930c-IN	stalactite	3	240.92	2.49
	AP930c-OUT	EID	3	252.32	2.98
Pixan Bel <i>4 samples</i>	BA273-IN	stalactite	8	209.55	2.13
	BA273-IN-2	stalactite	8	159.76	1.30
	BA273-OUT	EID	8	175.23	1.57
	BA325-IN	stalactite	4	229.32	2.74
	BA325-OUT-1*	EID	4	211.36	1.41
	BA325-OUT-2	EID	4	171.91	1.57
	BA357-IN	stalactite	5	332.41	5.14
	BA357-OUT	EID	5	167.84	1.43
	BA379-IN	stalactite	8	327.85	5.96
	BA379-IN-2	stalactite	8	224.00	1.80
	BA379-OUT	EID	8	103.89	0.91
Jaguar <i>26 samples</i>	AA125-IN	stalactite	10	397.15	18.8
	AA125-OUT*	EID	10	131.49	1.35
	AA147a-OUT	EID	11	106.01	1.05
	AA147b-OUT	EID	11	108.25	1.14
	AA147c-IN	stalactite	11	117.11	1.39
	AA147c-OUT*	EID	11	125.28	1.21
	AE818-IN	stalactite	10	206.61	1.67
	AE818-OUT	EID	10	249.92	2.26
	AE846a-OUT	EID	3	0.32	0.10
	AE846b-IN	stalactite	3	180.10	0.89
	AE846b-OUT	EID	3	0.07	0.03
	AE849-OUT*	EID	11	132.75	1.38
	AE849-OUT-2	EID	11	128.17	1.08
	AE860-IN	stalactite	12	88.14	0.60
	AE917-IN	stalactite	7	252.15	2.28

Table 4-1. Continued

AE917-OUT-1**	EID	7	48.95	2.01
AE917-OUT-2	EID	7	125.01	0.98
AGD5-IN	stalactite	4	342.45	5.92
AGD5-OUT*	EID	4	236.36	1.90
AGD5-OUT-2*	EID	4	275.42	5.47
AGD51-IN	stalactite	3	404.11	15.32
AGD51-IN-2	stalactite	3	646.11	124.94
AJ359-OUT	EID	0	3.61	0.04
AL359-OUT-2	EID	0	4.24	0.03
AL69a-OUT-1***	EID	3	143.86	1.62
AL69a-OUT-2	EID	3	224.11	3.26
AL69b-OUT	EID	3	215.06	3.36
AL69b-OUT-2	EID	3	205.55	1.99
AQ254	Flowstone	5	418.68	17.43
CD388-IN	stalactite	4	305.88	7.29
CD388-OUT	EID	4	206.74	2.93
CY12a-IN	stalactite	4	231.76	2.20
CY12a-OUT	EID	4	256.68	3.04
CY12b-IN	stalactite	4	317.79	5.68
CY12b-OUT	EID	4	226.39	2.21
CY12c-IN	stalactite	4	337.96	6.49
CY12c-OUT	EID	4	251.30	3.57
NG1a-IN	stalactite	4	1.25	0.10
NG1b-OUT	UW deposits	4	1.51	0.19
NG2a-IN	stalactite	1	1.47	0.04
NG2b-IN	stalactite	1	0.47	0.03
NG2c-IN	stalactite	1	26.77	0.13
NG2c-IN-2	stalactite	1	0.19	0.01
NG6-IN	stalactite	2	105.04	0.69
NG6-OUT	UW deposits	2	2.36	0.09

*Removed from analysis due to mixed layers in laboratory sample.

**Removed from analysis due to possible dust contamination.

***Removed from analysis due to possible recrystallization.

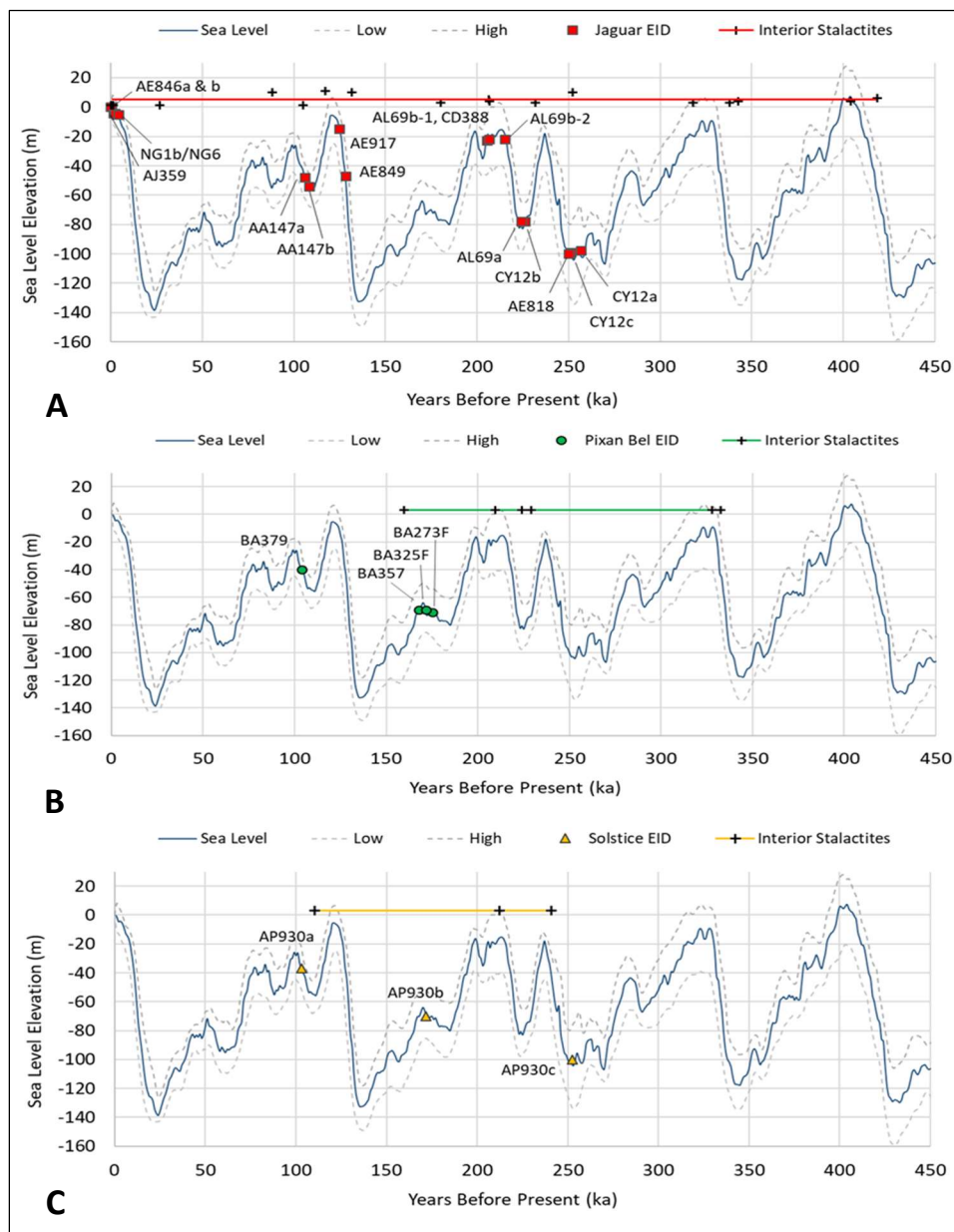


Figure 4-12. Speleothem age comparison with sea level records. EID U-Th ages from Sistema Jaguar (**A**), Pixan Bel (**B**), and Solstice Cave (**C**), are plotted against North Atlantic Sea Level curves compiled from ocean sediments, ice cores, and coral records at 1,000 year resolution (Spratt & Lisiecki, 2016). Error of the sea level records is shown by the dashed gray lines. The vertical axis shows the elevation of an EID at the time of its deposition. All samples shown were collected between 0 and 12 m amsl. The oldest date of $646 \text{ ka} \pm 125 \text{ ka}$ (not shown) was from an interior stalactite collected from Sistema Jaguar at $\sim 3 \text{ m amsl}$. Colored bars and +’s along the top represent the ages of interior speleothems and are plotted at the modern sample elevation.

4.4 Discussion

4.4.1 Evidence of uplift

Ages of stalactites and flowstone represent periods of time when the sample location was under vadose conditions, and therefore provide minimum ages of a conduit (i.e., the conduit must have existed first in order for speleothems to form). The oldest age of 646 ± 125 (AGD-51b) was obtained from an interior stalactite collected from a wall about 1 m above the water table (~ 4 m amsl) in the north-central portion of Sistema Jaguar. The large error margin is a result of the limitations of the U/Th isotope dating methods for samples >500 ka. The speleothem collected next to it, AGD51a, dated from 404 ± 15 ka, and a flowstone sample collected from the southern end of the cave at a similar elevation of ~ 5 m amsl returned an age of 419 ± 17 ka. While these older samples could be analyzed using U-Pb methods for more precise results, these U/Th results are conclusive evidence that large conduits existed, and were subaerially exposed, much earlier than the high stands of the late Pleistocene.

Our results permit a reconstruction of the caves' position relative to the water table over changing sea levels, where EID represent transitional periods when the water table was recorded in calcite deposits (**Figure 4-13**). Matching the ages of EID with past sea level elevations suggests that nearly all our EID samples were deposited during times of lower sea levels, and that the only reasonable explanation for why these samples are now found at or above modern sea level is that uplift has occurred. A best-fit trendline through EID date/paleo-elevation data suggests that for at least the past ~ 250 ka, uplift has occurred at a rate of ~ 329 mm/ka. Interior stalactite dates are generally consistent

with this explanation, and date to times when low sea levels occurred in the late Pleistocene (<200 ka).

Five interior stalactite dates from samples AE818, CD388, BA273, BA379, and AP930b range from 207 to 224 ka. This is inconsistent with relatively higher sea levels that are assumed to have occurred during this time period, although they are consistent with out-lying EID results (AL69a and AL69b) from the same time period. For all samples and dates, it is difficult to constrain prior elevations beyond 300 ka due to higher error of the U-Th dating method and greater uncertainty in sea level records. Interior stalactite ages that plot near peaks in the sea level curve often have error margins of $\pm 1-2$ ka that overlap with lower sea levels and would allow these samples to be placed at paleo elevations that generally agree with uplift rates. We have assumed that uplift has occurred linearly, but it is important to remember that these results indicate cumulative vertical displacement, which may be up or down, and does not necessarily occur at a consistent rate.

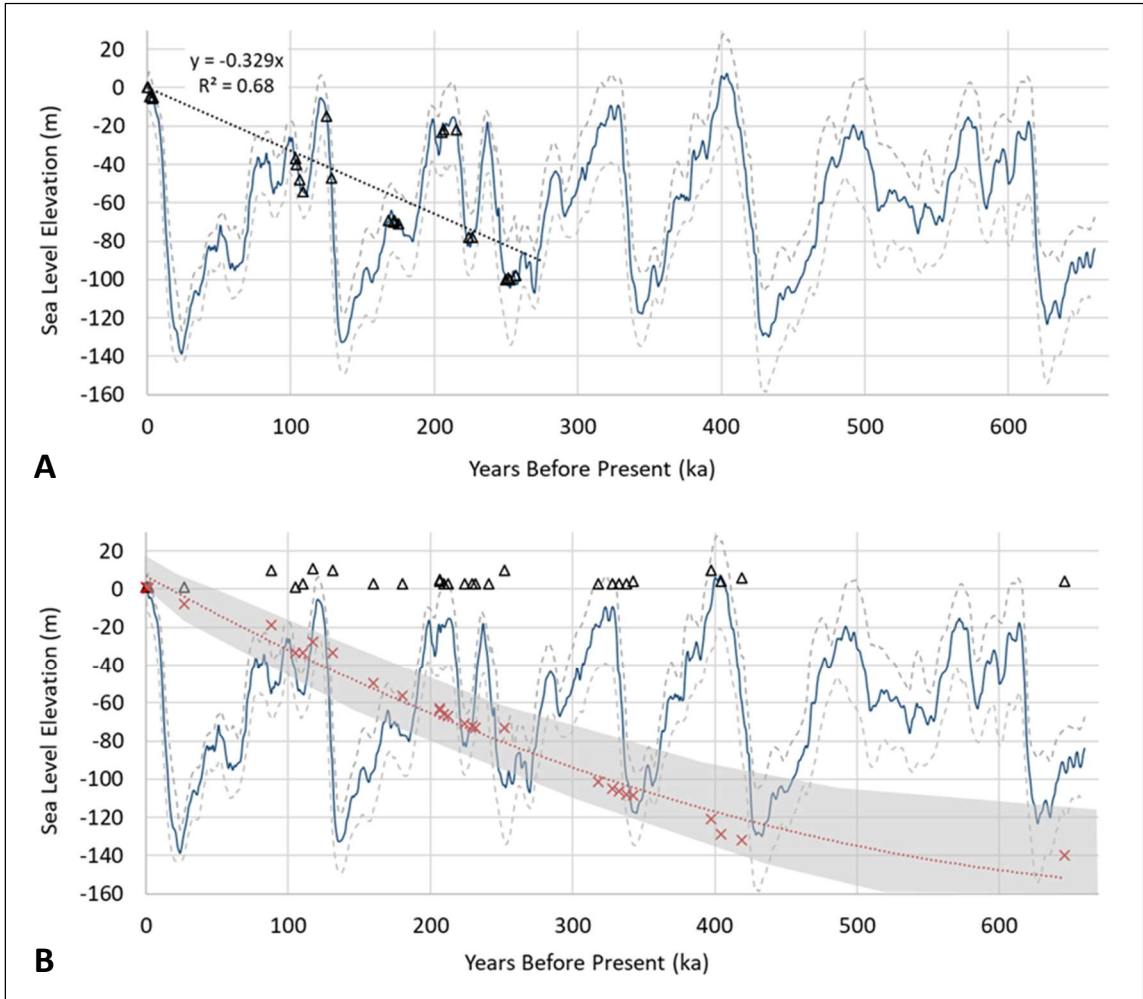


Figure 4-13. Possible prior conduit depths constrained by uplift. **(A)** A plot of all EID at the elevation of their deposition (assuming paleo-sea level is approximately equal to water table elevation) with a regression line indicating an average uplift rate of 329 mm/ka since ~250 ka. **(B)** Open triangles represent the modern elevations at which stalactites were collected. Red dotted line shows modeled past elevations, assuming an uplift rate of 329 mm/ka. Ages of interior stalactites (red x's) are expected to plot between peaks in the sea level curve. Shaded grey area represents uncertainty in conduit depth derived from errors in the sea level curve.

4.4.2 **Sample outliers**

Some sample dates are inconsistent with what might be expected, and possible reasons for these inconsistencies include: 1) limitations of stalactites and EID as a geological records, 2) laboratory samples with mixed layers of EID and/or interior speleothem, 3) contamination by dust or modern calcite/recrystallization, 4) error margins of the dating method, and 5) inaccuracy in sea level curves. Of these, only (2) and (3) warrant the removal of a sample from analyses. Samples with a possibility of recrystallization or contamination will be examined by thin section prior to publication of this data.

Interior samples in our results were older than EID covering them, except where sampling occurred close to a hollow soda straw (AP930c-IN, AE818-IN, and CY12a-IN). In these cases, it is likely water levels dropped relative to the location of the speleothem that the soda straw became active again after EID were deposited.

EID for this study were entirely collected from stalactites, but they can form on any speleothem or rock surface at the water table. Because EID are deposited with changing water levels, ages of exterior layers from the bottom to the top of a sample are not necessarily sequential. It is therefore important to cut a speleothem crosswise or lengthwise and obtain a sample for laboratory analysis from within a layer and avoid mixing the sample across layers or with the interior speleothem or rock. Several samples had to be removed from the final dataset because close inspection after analyses showed that the sample had been extracted from mixtures of EID, stalactite, and/or younger calcite inside the soda straw. AE849-OUT-1 was cut across layers on the exterior, so it was removed from analysis. A repeat sample of this material (AE849-OUT-2) was taken

from a cut cross section in which the layers could be more clearly seen and discretely sampled. AA147c and AA125 were mixed with the interior stalactite and removed from analysis. However, AA147a and AA147c were collected in the same area as these speleothems, and those samples were cut and sampled properly. AGD5 was removed from analysis because the speleothem was crumbly and had very thin layers, making it difficult to obtain accurate exterior samples.

CD388-OUT was collected in the central portion of Sistema Jaguar approximately 1 m above the water table, or ~4 m amsl. The age of the EID sample was 207 ± 3 ka, corresponding to a former sea level of -22 m below msl, which would place it at a higher paleo-sea level elevation than the trend shown in **Figure 4-12** would suggest. This sample may have been recrystallized during times of higher past sea level because it is within 1 m of the water table.

In other cases where sea level and sample ages do not appear to follow the uplift trend, they could have been affected by U- contamination from detrital sediment or re-crystallization:

AE917-OUT-1 was dated at 49 ± 2 ka. This is surprising because sea level at that time is thought to have been around -80 m below modern sea level, yet the speleothem was collected near ~10 m amsl and ~6.5 km inland. Composite curves derived largely from ocean and ice cores are known to be insensitive to rapid changes in sea level depending on where glacial volumes are changing (Arz et al., 2007), and it is possible that this sample records a brief high stand. Evidence consistent with a brief high stand between 49-51 ka BP has been documented in the Red Sea (Arz et al., 2007), Sea of

Japan (Bahk et al., 2000), California (Muhs, 1992), and the Bahamas (Myroie & Carew, 1988). However, this sample is also crumbly and covered with red clayey dust that potentially contains trace amounts of U that could skew results toward a younger age. The source of this clayey dust is uncertain but could either be Saharan windblown dust or residual clay that has weathered from limestone in-situ and leached through the vadose zone. This sample was removed from analysis due to poor sample quality and low confidence in laboratory results.

AL69a-OUT-1 was dated at 144 ± 2 ka which places the elevation of deposition at -112 m bmsl, while a second date on the same speleothem, AL69a-OUT-2, corresponds to 224 ± 3 ka, a time of higher sea level that places a phase of deposition at -23 m bmsl. Another speleothem, AL69b, was collected next to and slightly above AL69a, and had two EID dates of 215 ± 3 ka and 206 ± 2 ka suggesting that EID at this site were deposited earlier. AL69a-OUT-1 was collected at the water table within the range of modern seasonal fluctuations in water level, and consequently had a thin exterior modern calcite coating where it has been submerged. This sample was extracted from the side in the coated part of the speleothem, and recent calcification or recrystallization is suspected of skewing the result toward a younger age.

The ages of EID plot at progressively lower paleo-sea level elevations over time, except for three EID dates obtained from two samples discussed below:

AE917-OUT-2. A sample was obtained from a central ring of the EID surrounding the interior stalactite and yielded an age of 125 ± 1 ka. This corresponds to a time when sea level was -15 m bmsl (Spratt & Lisiecki, 2016), but coincides with a period of rapid

sea-level rise. Overlapping error bars on the sea level record and EID age confounds precise interpretation of a depositional elevation.

AL69b-OUT-1 and -2. The speleothem was collected ~6 km inland in the north-central part of Sistema Jaguar at 21 cm above the water table or ~3 m amsl. The age of AL69b-OUT-1 was 206 ± 2 ka corresponding to a former sea level of -22 m below msl, which plots higher than the trend of all samples. The age of AL69b-OUT-2 was 215 ± 3 ka, corresponding to an elevation of -23 m below msl. The results may be skewed by recent calcite deposits, as the collection site was located near the water table and within the range of storm-related water level fluctuations. Recrystallization could also have occurred during past higher sea levels. If the age is correct, then it either constrains the timing of the sea level rise to after 215 ka BP, or indicates a brief low stand occurring between 205 and 215 ka BP.

4.4.3 Accuracy of sea level curves

Caribbean Sea level records spanning the timeframe of this research (0 to 600 ka), and with resolution comparable to the precision of our U-Th ages, either do not yet exist or are not available, and therefore we used a global composite record comprised of seven data sets (Spratt & Lisiecki, 2016). The composite record incorporated sources from various geographic areas and using different methods including: Atlantic coral and benthic $\delta^{18}\text{O}$ (Sosdian & Rosenthal, 2009; Waelbroeck et al., 2002), Pacific benthic $\delta^{18}\text{O}$ (Elderfield et al., 2012), global planktonic $\delta^{18}\text{O}$ (Shakun et al., 2015), Mediterranean and Red Sea hydraulic modeling (Rohling et al., 2014, 2009), and inverse modeling of ice sheets (Bintanja et al., 2005). The accuracy of individual sea level reconstructions is limited by measurement error, local variations in salinity and temperature, and

assumptions particular to each technique (Spratt & Lisiecki, 2016). All seven data sets were interpolated to a 1 ka time-step up to 800 ka and a common signal was identified using PCA analysis (Spratt & Lisiecki, 2016). An orbitally-tuned age model (Lisiecki & Raymo, 2005) with an uncertainty of ± 4 ka provided the framework for the timing of sea level changes; the focus of the composite reconstruction was on the amplitude of sea level variability rather than its precise timing (Spratt & Lisiecki, 2016). In particular, the composite high stand estimates likely fail to capture short-term fluctuations but rather reflect the mean sea level during each interglacial period (Spratt & Lisiecki, 2016).

The Spratt & Lisiecki, 2016 curve is compared to other sea level reconstructions of varying time-steps in **Figure 4-14**. An orbitally-tuned model based on sediment cores from the Red Sea and correlation to the Asian monsoon in a speleothem from China (Grant et al., 2014), has the highest available resolution of 0.125 ka, but only extends to 500 ka. Another global composite curve derived primarily from ice core, coral, and ocean sediment (Miller et al., 2005) extends back to 9 Ma at 5 ka resolution, and tends to have greater uncertainty in both amplitude and timing in comparison to the Spratt & Lisiecki, 2016 data. A 450 ka reconstruction with a 1.5 ka time-step is based on data from $d^{18}\text{O}$ of foraminifera in ocean sediments from the North Atlantic fitted to sea level trends derived from Caribbean coral (Waelbroeck et al., 2002). While this record was incorporated in the composite data set, it is provided here for comparison to highlight any discrepancies that may explain outliers.

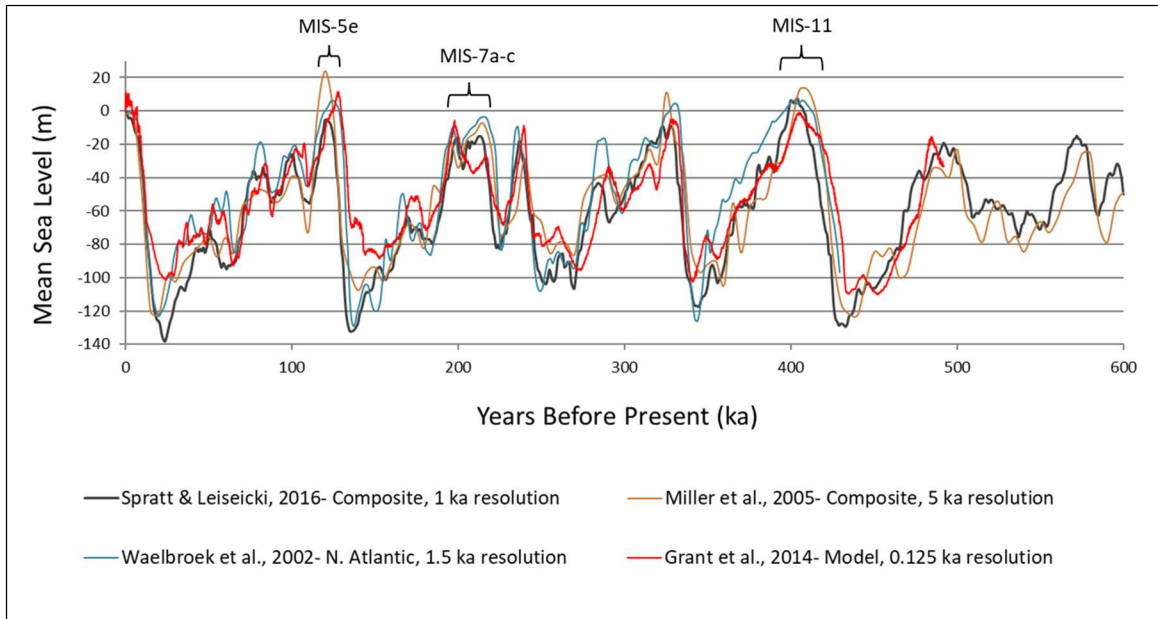


Figure 4-14. A comparison of Pleistocene sea level curves. Each sea level record is derived from multiple sources and methods providing resolutions ranging from 0.125 ka (Grant et al., 2014) to 5 ka (Miller et al., 2005). Marine Isotope Stages of sea level high stands are identified with brackets, showing ranges of possible timing and amplitude across sea level records.

AE917-2 (125 ± 1 ka) is located near a peak that occurs between ~ 119 to 126 ka BP, also known as the Marine Isotope Stage (MIS) 5e high stand. The reconstruction with the most precise timing (Grant, 2014), places the initial rise in sea level at 134 ka BP. The MIS5e high stand may have consisted of two high stands, each separated by several thousand years (Kopp et al., 2009). If this is the case, then AE917-2 likely represents a short low stand between these sudden rises. (**Figure 4-15**).

AL69b-1 (215 ± 3 ka), AL69b-2 (206 ± 2 ka), and CD388 (207 ± 3) were all deposited during MIS stages 7a-c (~ 197 to 214 ka BP). There is a possibility that these samples have undergone recrystallization at the modern water table or during prior high stands. However, it is also possible that they were deposited during brief low stands, and that existing sea level records fail to capture sudden changes at the millennial-scale.

Isotope records from speleothems deposited during these intervals should indicate any significant climate shifts.

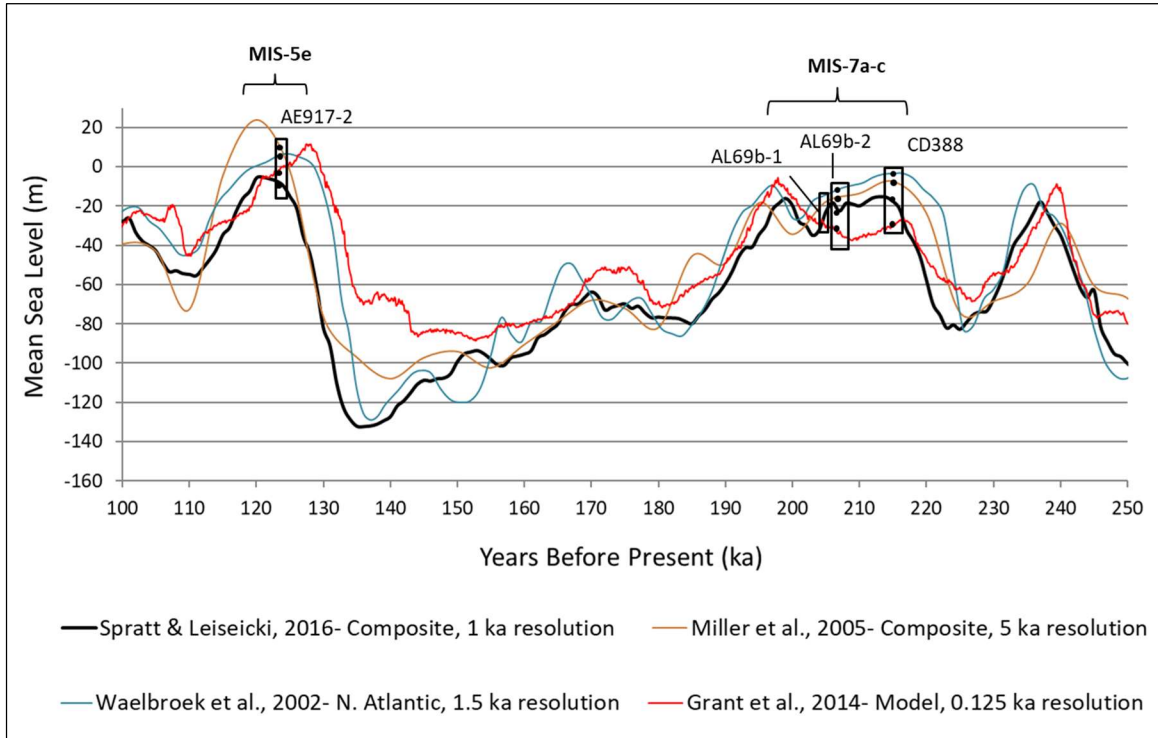


Figure 4-15. A comparison of outlier EID elevations. Spratt & Liesiecki (2016), shown by the bold black line, was the composite curve used in this analysis. Outliers from this study are plotted according to different sea level records ranging in resolution from 0.125 ka to 5 ka. The black boxes outline the range in possible sea level elevations within the age error of each sample. The timing of sea level high stand or low stands is imprecise, and this likely explains the occurrence of outliers near peaks.

4.4.4 Comparison to coral and other speleothem records

U-Th ages of 124-133 ka from six coral samples collected at 2 to 4 m amsl near Xel Ha and in Cozumel were interpreted as evidence of tectonic stability since the MIS-5e high stand, because the coral elevations are consistent with coral of similar age and elevation in other locations throughout the Caribbean (Szabo et al., 1978). This interpretation followed from the assumptions that the modern elevation of the collected

coral represented the maximum elevation of the former reef crest, and that negligible surface erosion has occurred since the time of its exposure. The coral specimens collected by Szabo, et al., (1978) were identified as *Diploria sp.*, and *Montestrea sp.*; stony corals that prefer mid-reef environments of 5 to 30 m depth but, depending on the species, can tolerate depths of 40 to 90 m. Our results are consistent with a scenario in which uplift has occurred at approximately 329 mm/ka, placing coral from 124-133 ka BP at 40-43 m bmsl. While this is deeper than coral would be expected to thrive, a rapid rise in sea level drowning the reef would result in a preserved assemblage of more depth-tolerant species. A summary of the vertical ranges of fossil coral species documented at Xel Ha is presented below in **Table 4-2**:

Table 4-2. Fossil corals documented near the study area by prior work.

Species	Depth preference (m)	Depth tolerance (m)	Elevation (m amsl)	Source
<i>Acropora palmata</i>	1-5	20	1-5	Blanchon et al., 2009
<i>Acropora cervicornis</i>	5-20	30	0-5	Blanchon et al., 2009; Back et al., 1986
<i>Siderastrea siderea</i>	0-10	40	1-2	Blanchon et al., 2009
<i>Porites sp.</i>	0-10	40	2.5-4	Blanchon et al., 2009
<i>Diploria sp.</i>	5-15	40	4	Szabo et al., 1978; Back et al., 1986
<i>Montastrea sp.</i>	12-30	90	2	Szabo et al., 1978; Back et al., 1986

Coral growth information from: (Fricke & Meischner, 1985; Goreau & Wells, 1967; Humann & Deloach, 1992; Warner, 2012).

Yucatan speleothems have also been sampled to constrain the timing of sea level changes, as most speleothems only develop above water. Moseley et al. (2013) sampled 11 stalagmites from submerged and dry passages, all of which dated from the late Pleistocene (59-117 ka) (**Figure 4-16**). This is consistent with lower sea levels but does

not provide a proxy for sea level position; it merely provides a potential maximum elevation for sea level at that time. A speleothem collected from Rio Secreto, an epiphreatic cave north of the study site, was sampled for Holocene climate data (Medina-Elizalde et al., 2016). Its position marks the elevation of modern cave passage that has remained above the water table for ~14 ka. Additional sampling of specific kinds of cave formations that develop at or near sea level provide more precise constraints on tectonic history and existing sea level records.

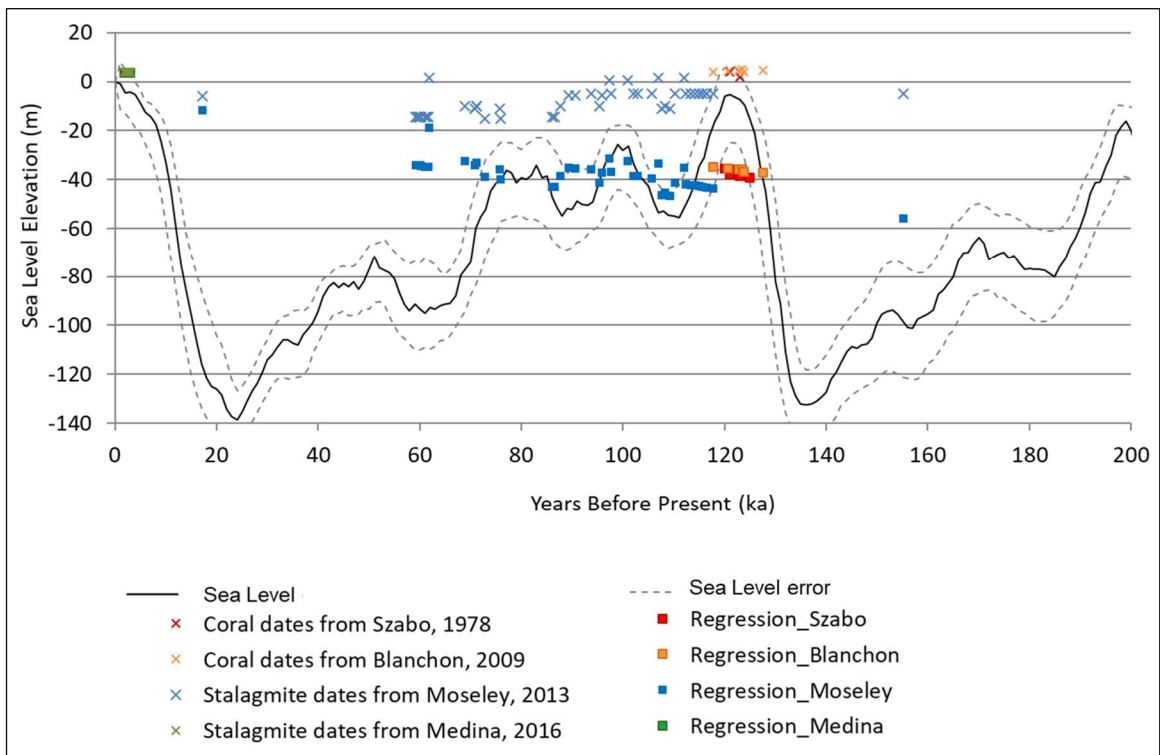


Figure 4-16. Published U-Th dates from coral and speleothem samples. Sea level is from Spratt & Lisiecki (2016), shown by the bold black line with high and low error margins dashed in grey. U-Th ages of stalagmites and corals are plotted with “x’s” at the elevation of sample collection. The squares represent paleo- elevations of samples assuming a cumulative uplift rate of 329 mm/ka.

4.4.5 Landscape evolution

If caves formed at their present elevation, then this restricts the possible time of speleogenesis and conduit formation to very brief periods during the Pleistocene, totaling approximately 20,000 years, as the mixing zone passed through the elevation where they now occur. A large, deeply-incised lagoon at Xel Ha, ~10 km north of Sistema Jaguar, would potentially have been in the coastal mixing zone for 5,000 years while sea level rose to its present elevation, and its development has been explained using theoretical geochemical mixing models, although no conclusive field data was collected demonstrating extensive undersaturation with respect to calcite occurred in the lagoon (Back et al., 1979). It has been suggested that coastal caves can form in as little as 10,000 years (Mylroie & Carew, 1990), but such work considered relatively small-volume caves and it seems doubtful that 1,000's of km of large (e.g., 10+ m tall and 80+ m wide in Sistema Jaguar) passage in Quintana Roo, Mexico could have developed so rapidly under even the most ideal geochemical conditions. In addition, many portions of the above-water conduits have dissolutionally-formed ceilings that are 8-10+ m above modern water table elevations. This further restricts the possible duration of conditions under which conduits could have formed at these elevations and makes it even more unlikely that they formed during brief high stands.

Surface lowering, or denudation, occurs as rainfall, runoff, and percolating surface waters chemically erode bedrock and hydrologic systems transport the dissolved mass out of the system. This process reduces surface elevation relative to sea level, and will expose, collapse, and ultimately remove any underlying conduits over geologic timescales. Surface erosion of carbonates is accelerated by colder temperatures and by

higher precipitation rates (Ford & Williams, 2007). Precipitation is far more influential than temperature, and denudation rates measured or modeled in a wet, tropical environment can be exceptionally high –between 175 and 300 mm/ka – based on experimental and modeled rates (**Table 4-3**); (Ford, Palmer, & White, 1988; Sheen, 2000). Modeled rates assume runoff as the difference between precipitation and evapotranspiration, which are often poorly constrained parameters across geologic time scales. Field observations of erosion beneath boulders along the northern coastline of Guam suggest lower denudation rates of ~50 mm/ka (Myroie & Myroie, 2018). This much lower rates could be attributed to very thin soil cover, as higher pCO₂ values greatly accelerate of dissolution (Brook et al., 1983).

Table 4-3. Modeled and measured rates of tropical karst denudation. Surface lowering rates have been determined by experiment (micro erosion meters, laboratory), by geochemical modeling, and from field observations of erosion beneath boulders (“Pedestals”) of known age.

Location	Max SL Rate (mm/ka)	Method	Source
Kikai jima, Japan	205	Pedestal	Matsukura et al., 2014
Aldabra atoll, Indian Ocean	260	Pedestal	Trudgill, 1976
	200	Laboratory testing	Ford et al., 1988
	175	Modeling estimate	Sheen, 2000
Bikini atoll, Marshall Islands	300	Micro Erosion Meter	Revelle & Emery, 1957
Victoria, Australia	300	Micro Erosion Meter	Gill & Lang, 1983
Grand Cayman Isl., Bahamas	177	Micro Erosion Meter	Spencer, 1985
Guam, Mariana Islands	50	Pedestal	Myroie & Myroie, 2018

Landscape evolution by denudation has functionally been discounted by omission in prior speleogenesis work on the Yucatan Peninsula, which could perhaps be justified under assumptions of very recent conduit formation. However, using the measured and modelled rates of denudation, the land surface should have been lowered between 18 and 24 m during subaerial exposure in the past ~120 ka, which means that much of the Yucatan Peninsula should, in fact, lie below modern sea level, even assuming that significant carbonate deposition occurred during the last sea level high stand.

In the context of our new data demonstrating that conduits that now lie at or above sea level were well-developed at least 400-600 ka, and assuming that measured and modeled denudation rates are applicable for the Yucatan Peninsula, then the existence of a Pleistocene or older carbonate land surface that lies at or above modern sea level raises serious questions about assumptions of tectonic stability of the Yucatan Peninsula. In order for the current land elevation to be consistent with estimated surface lowering rates, then either 1) surface lowering processes must have occurred much more slowly (or not at all) over the past 2 Ma than has been estimated and measured for tropical environments, or 2) the peninsula has not remained tectonically stable. If tectonic uplift has occurred, then it must have been at rates similar to, or slightly higher than, denudation in order to result in the low-relief landscape that is currently near or slightly above sea level. If the rock exposed at the surface is of Pliocene age, and the average sea level elevation at the end of the Pliocene ~2.6 Ma was -35 m bmsl (Miller et al., 2005), then the modern rock surface would have been at least that much lower even assuming zero denudation.

Our data warrants a revision of the current conceptual model of speleogenesis in the Yucatan Peninsula. Rather than conduit development occurring *in-situ* at their presently observed elevations as the mixing zone passes through across changing sea levels, a combination of uplift and surface lowering have also influenced the vertical distribution of karstification. The result is a complex overlay of younger and older passages containing formations across a range of ages, whose elevation reflects the cave's history relative to changing sea level (**Figure 4-17**). The geologic timescales over which landscape-forming processes act presents practical limitations for experimental determination and direct observations, however, inferences can be made from multiple data sources and evaluated for consistency. (**Table 4-4**).

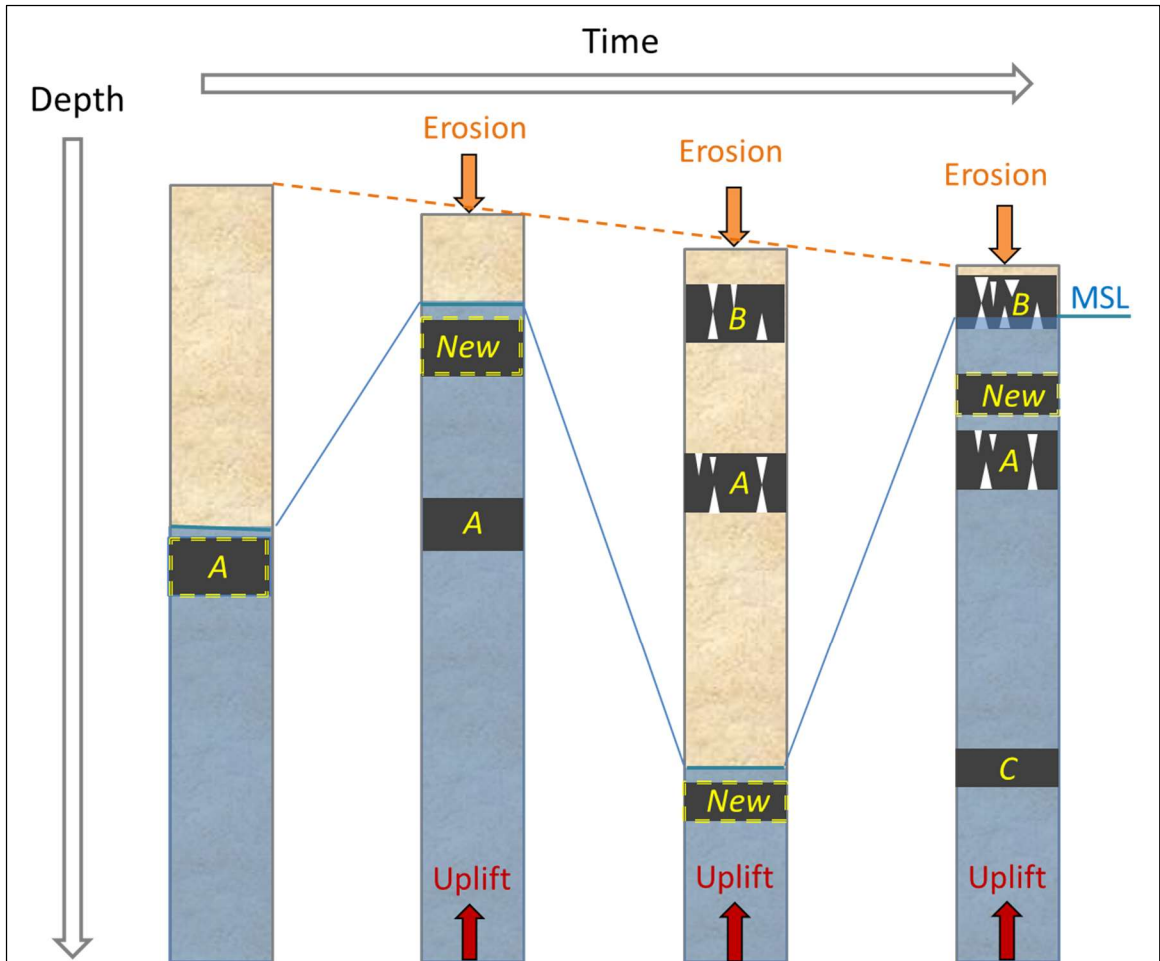


Figure 4-17. A diagram representing phases of cave development. Conduits develop in mixing zones that correspond to changing sea level, with uplift and denudation occurring simultaneously. The result is a complex overprinting of conduit levels containing formations that develop during times of subaerial exposure.

Table 4-4. A summary of observations and assumptions of tectonic stability. H_0 = no uplift has occurred since the Pleistocene, and H_1 = uplift has occurred since the Pleistocene.

Observation	Source	H_0	H_1	Notes
Coral head dates from 120-125 ka at 2-4 m amsl	Szabo et al., 1978	✓	✗	Assumes no surface denudation; <i>Diplora sp.</i> & <i>Montastrea sp.</i> prefer 12-30 m depth, tolerate 40 m.
Reef crest coral from 120 ka at 6 m amsl	Blanchon & Shaw, 1995	✓	✗	<i>Acropora palmata</i> prefers 0-5 m, but tolerates 12 m depth. 329 mm/ka uplift would result in 40 m vertical displacement to modern sea level.
Level topography, lack of outcrops and fault scarps	Ward & Weidie, 1985	✓	✗	Structural features may be obscured by vegetation or removed via erosion.
Tropical denudation rates ~150 to 200 mm/ka	Sheen, 2000; White, 1984	✗	✓	18-24 m of overlying rock would be removed in 120 ka.
Coastal caves can form in 10 ka; Large Caletas (Xel-Ha) can be incised in 5 ka	Mylroie & Carew, 1990; Hanshaw & Back, 1980	✗	✓	Rapid dissolution would generate the largest conduits at 20-50 m below msl in a stable platform; yet few are known.
Ages of speleothems from the Pleistocene	Moseley et al., 2013; this study	✓	✓	Sea level was very low during most of the Pleistocene; speleothem ages document vadose conditions but are inconclusive about elevation.
Lack of distinct cave levels or sea terraces	Kambesis, 2014	✗	✓	Tiers of cave development and/or sea level terraces would be expected in a stable tectonic scenario, but these have not been clearly identified.
Large cave volume found higher than any recent high stand	this study	✗	✓	Underwater caves form via mixing dissolution; if shallow caves form by the same process, they must have formed during higher sea levels.
EID samples indicate uplift	this study	✗	✓	Older ages correspond to times of lower sea levels, indicating an uplift rate of ~329 mm/ka.

4.5 Conclusions

Calcite speleothems are deposited in caves only during subaerial exposure and therefore constrain a minimum age of passage development. EID develop only during times where the cave passage is coincident with the water table and, in combination with sea level records, therefore provide a record of prior water table elevations that serve as indicators of uplift.

Assuming that caves in the Yucatan formed along the halocline, this research concludes that elevations of past conduit development should lie at or below elevations of

past sea levels. Cave systems that presently lie at or above the water table were formed at lower elevations, and their current position relative to the land surface is the result of both uplift and surface denudation. Deeper conduits have gradually risen as uplift occurred, and new conduit form at higher or lower positions relative to them as sea level changes. Simultaneously, surface erosion is occurring and removing overlying rock, which eventually leads to the collapse of passage ceiling (i.e., documented linear zones of large passage collapse and collapse sinkholes).

The ages of submerged speleothems found in many caves in Quintana Roo demonstrate that the conduits predate the Pleistocene (Collins et al., 2015; Moseley et al., 2013). Interior stalactites collected underwater in this study demonstrate that even 5 to 10 ka BP, the now-active conduit system was dry. Zones of mixing and active flow are presently located in caves only because existing conduits provide hydraulically efficient flow paths, as evidenced by a thinner freshwater lens than theory predicts, and not because the caves formed at their present position relative to the water table.

Our results are consistent with speleogenesis by mixing dissolution but contradict the hypothesis of formation within a stable platform experiencing changing sea levels. Our results instead provide the first concrete evidence that cave passages are much older than previously assumed. Caves appear to have developed over much longer periods of time, experiencing multiple episodes of submergence, enlargement, and vadose speleothem formation as the platform slowly uplifts at a rate of ~ 329 mm/ka. Cumulative uplift in the Yucatan Peninsula could be a result of tectonic movement and/or rebound from mass loss via chemical dissolution.

5. CONCLUSIONS

5.1 Review of Chapter Objectives

5.1.1 Chapter 2: Identify hydrogeologic controls on karstification

The morphology, orientation, and distribution of sinkholes were evaluated for patterns indicative of influence of structural features or geologic properties. No significant difference in morphology occur across Tertiary and Quaternary geologic units, but there are differences in depression distribution and orientation. The point density and clustering of depressions $>25 \text{ m}^2$ identified in a LiDAR-derived DEM is significantly higher in the Tertiary rock. This is supported by field observations that include sinkholes $\sim 1 \text{ m}^2$, where density is significantly higher along transects in Tertiary rock. Long-axis orientations of all sinkholes revealed three trends at $\sim 45^\circ$, 300° , and 345° ; depressions in the Tertiary rock contain proportionally more sinkholes oriented at 345° , which suggests that hydraulic gradients have been oriented at this trend over geologic time and groundwater flow paths have preferentially developed along it.

Alignment of sinkholes with their Nearest Neighbor showed two trends at 45° and 315° , which suggests hydrologic and geologic properties may be controlling sinkhole formation. The same trends are apparent in both geologic units, but the 45° trend is stronger in the Quaternary rock and 315° is stronger in the Tertiary rock. Cave passage trends and field observations of the alignment of sinkhole clusters also identified these trends, as well as some features oriented north, which were not detected in the DEM analysis.

The similarities in morphology across geologic units suggest that similar formative processes, geologic controls, and hydrogeologic conditions exist across the study area. The differences in distribution and density likely reflect stages in karst maturity, as the Tertiary rock has experienced more time for dissolution to occur. Dominant trends in sinkhole orientation were observed at approximately 120° and 60° to one another, which is possibly related to jointing where the Rio Hondo and Holbox/Catoche Fault Zones overlap; however, the lack of outcrops or observable joints in cave passage make this interpretation inconclusive. Local variation in rock properties due to facies changes, and related influence of the hydraulic gradient could also explain the elongation of depressions, particularly for large solutional sinkholes. Sinkhole alignment to Nearest Neighbor, trends of cave passage, and alignment of sinkhole clusters observed in the field, all support the same trends parallel and perpendicular to the coastline. These trends are interpreted to represent the hydraulic gradient perpendicular to the coastline, and changes in depositional facies parallel to the coastline (which could also influence flow direction).

Higher resolution DEM data and improvements in processing will permit more detailed analysis in the coming years, but further interpretation will also benefit from additional field observations. Future work could include detailed geologic mapping to identify lateral and vertical changes in depositional facies, and any possible fault scarps. Porosity measurements of rock samples would provide indications of geological influence on clustering and alignment. Finally, water table elevations and hydraulic gradients could be monitored in large, shallow depressions (such as the one north of

Chango Mistico) to establish their hydrogeologic connectivity and relation to conduit development.

5.1.2 Chapter 3: Quantify and constrain coastal aquifer properties

Long-term high-frequency water level data were collected in hydrologically connected pools in epiphreatic caves and were analyzed to constrain a range of values for aquifer properties including diffusivity (1.74×10^7 - 1.02×10^9 m²/day), transmissivity (5.23×10^6 - 3.07×10^8 m²/day), and hydraulic conductivity (4.36×10^4 - 2.55×10^6 m/day).

Diffusivity was determined using both tidal data and stormwater recession curves.

Hydraulic conductivity was calculated using an assumption of aquifer thickness equivalent to the freshwater lens to permit comparison with previous work, but also using the entire permeable thickness of the bedrock. The hydraulic gradient was measured from the coast to ~7 km inland. Total discharge was estimated per 1m² cross-sectional area and per km of coastline; contributions to discharge from conduit, fracture, and matrix components were estimated using slope changes in stormwater recession curves.

Aquifer property values of D, T, and K vary across two orders of magnitude, which is comparable to other coastal karst systems. Diffusivity values derived from tidal data match well with values calculated from the inferred conduit component of discharge observed in stormwater recession curves. The hydraulic gradient was expected to be low, based on previous work done at the regional scale, but is up to 1.2 m/km within 0.5 km of the coastline, and levels out to ~0.1 m/km approximately 5 km inland. The steep gradient is interpreted to reflect a change in permeability between Tertiary and Quaternary rock units that is mapped at approximately 4 km inland. Discharge occurs primarily via conduits, but also via fractures and small coastal seeps observed along the beach at low

tide. Water in epiphreatic caves in our study area does not represent flow through primary conduits, but full-conduit flow could be occurring in deeper, hydrologically connected phreatic passage.

Some limitations of this study include assumptions for values used in calculations, namely storativity and aquifer thickness. Storativity was assumed to range from 0.1 to 0.3 based on work in other coastal karst areas but would ideally be determined by pump tests in wells. However, no wells exist yet in the study area. The permeable depth of the aquifer is not known but is assumed to be, at most, the maximum depth that sea level has been during the Quaternary (and where dissolution likely occurred in the mixing zone relative to past sea levels). Previous work has considered the effective permeable depth to be equivalent to the thickness of the freshwater lens, since conduits are coincident with it and facilitate flow. The thickness of the freshwater lens is not known in the study area; the deepest pit in Chango Mistico contained completely mixed meteoric water to a depth of 30 m with no halocline detected. The equation that was used to estimate lens thickness, based on halocline depths observed in cenotes, likely provides an underestimate. In addition to uncertainty in calculations, there was uncertainty in measurement of the hydraulic gradient. Water level elevations were established by survey to GPS benchmarks, but even with differential correction the precision of the signal was limited by vegetation cover and available satellites. Future work would benefit from a high-precision level loop survey from water table pools to a benchmark at the coastline. Gradients could also be measured parallel to the coastline and between conduits.

5.1.3 Chapter 4: Constrain timing of conduit development

Cave ages were constrained using U-Th dating of stalactites and EID. Samples also included flowstone and recent secondary calcite deposits collected 1 to 3 m underwater. U-Th ages of the EID generally coincided with times of lower sea level, and the trend of all depositional depths with age indicate an uplift rate of ~ 329 mm/ka since at least 200 ka. A minimum conduit age of 646 ± 125 ka was established from a stalactite collected in Sistema Jaguar. Speleothem and flowstone ages from 400 to 600 ka to constrain the timing of uplift initiation to no earlier than 300 ka, as these samples must have been deposited in subaerial conditions and continuous uplift would place them underwater at the time of deposition.

Based on the current understanding of speleogenesis and assumptions of tectonic stability in the Yucatan, it was expected that EID ages would all correspond to relatively recent prior high stands and that the cave passage would be geologically young (< 125 ka). Results instead indicate that conduits developed at lower elevations and have been lifted to their modern position relative to sea level. EID outliers occur close to peaks and likely represent short-duration low stands on a millennial timescale that are not reflected in global sea level records. The time available for cave formation is ultimately constrained by the age of the rock, which is thought to be at most 5.8 Ma, but considerable passage volume occurs in units mapped as younger than 2.6 Ma. The time of conduit formation is therefore roughly constrained between 636 ka and 2.6 Ma, with an estimated land surface elevation 20 to 40 m lower than present, based on modeled and measured denudation rates for tropical karst areas.

Further work should be done to clarify inconsistencies in the data. EID outliers are potentially altered by recrystallization occurring during periods of submergence, and this possibility needs to be addressed by close examination of thin sections. U-Pb dating of wall rock would provide a more certain maximum conduit age by constraining the matrix age. Stratigraphic interpretations of reef crests need to be revisited with a consideration of uplift occurring during the Pleistocene. A mechanism for uplift needs to be identified; likely either tectonic displacement or isostatic rebound related to mass-loss from denudation, or a combination of both mechanisms. Denudation could have accelerated as a result of increased precipitation, and additional paleo-climate research could identify any change in climate that may coincide with the initiation of isostatic rebound. EID from elsewhere in the Yucatan should be collected and tested to more precisely define the uplift rate, to test for possible variations in uplift in different geographic locations, and to determine if and where uplift is still occurring.

5.2 Significance

5.2.1 Scientific contribution

This research contributes a revision of the conceptual model of speleogenesis and tectonic history of the Yucatan Peninsula. The assumption of tectonic stability has been refuted, meriting reinterpretation of studies that utilized coral ages as sea level indicators and necessitating more detailed data on the rates of denudation and mixing dissolution. Previous work that relied on assumptions of tectonic stability for geologic interpretation, such as the formation process of Xel Ha lagoon and rapid dissolution of extensive cave systems, can now be placed in their proper context of geologic time. Future work is

needed to identify the causal mechanisms of observed cumulative uplift and to clarify the geographic extent and linearity of vertical displacement trends.

EID offer a new method for measuring rates of vertical displacement and for interpreting the hydrogeologic history of coastal karst regions. Differences between EID ages and sea level records need to be further examined, but assuming precise ages and high-quality samples, the accuracy and precision of U-Th dates of speleothems is greater than that of most other sea level proxies. Geologically rapid deposition within a narrow range at the water table make EID ideal markers for both the amplitude and timing of millennial-scale sea level changes that have potentially been omitted in global-scale models derived from ocean sediment and ice cores.

My studies of sinkhole geomorphology and coastal hydrogeologic properties highlight the importance of characterizing related aspects of a karst systems across scales to identify heterogeneities that influence how and where groundwater flows. Locally and regionally, these data help to 1) relate and explain patterns in karstification that reflect underlying geology, 2) parameterize aquifer properties between conduits, and 3) provide new knowledge regarding the coastal hydraulic gradient. Globally, these data provide comparisons for other coastal karst systems such as in Florida, South-central Australia, Southeast Asia, and some Caribbean and Pacific islands.

5.2.2 Application and social impact

Geomorphic and point-pattern analysis of depressions provides a means to assess the risk of sinkhole formation in areas with few geologic outcrops and limited surface exposure for effective geologic mapping. My research provides detailed data that can

potentially be applied to other areas in the region or in the world with similar geology to assess the likelihood of encountering caves and facilitating the collapse of passage. These data will be needed as urban expansion continues, as it will help inform responsible construction practices and safe placement of roads and rails.

The quantification of aquifer properties and an improved understanding of the regional flow dynamics will increase the accuracy of water budget calculations in Quintana Roo, Mexico, where effective water management is strained by a lack of data, rapid population growth, and urbanization. High connectivity in karst facilitates transport of contaminants across the entire region, and eventually water discharges through springs at the shoreline, where contaminants threaten coastal ecosystems and coral reefs. My research will help those who develop numerical models better address problems of water resource management in this and other coastal karst regions.

Comparisons of EID ages from around the world to sea level curves derived from various sources would provide valuable data to inform climate models and help to answer questions about system sensitivity related to climate change. Coastal areas are vulnerable to the consequences of rapid sea level rise, and concerns about climate change provide motivation to understand global climate mechanisms that can result in sea level fluctuations at a millennial scale. Precise measurements possible with U-Th dates of EID, will help to refine the resolution of existing sea level records and possibly identify past rapid changes in sea level that are obscured in other records.

APPENDIX SECTION

APPENDIX A

Terms of Karst Hydrogeology:

(based on Neuendorf, Mehl, and Jackson, 2005)

Calcrete or Caliche – Hardened limestone crust that forms at the ground surface in arid climates where calcite precipitates from evaporating water.

Carbonate – Rock containing calcium carbonate, namely limestone deposited in a marine environment.

Cenote – A cavern that has collapsed into passage and exposed the water table.

Diffusivity – A measure of how a pressure pulse propagates through a porous medium.

Doline – A naturally formed closed depression occurring in karst terrain.

Epiphreatic – The subterranean zone that encompasses the transition between the vadose and phreatic zones, and which includes the water table.

Halocline – The density interface where freshwater floats above saline water.

Hydraulic conductivity – The volume of water at a given viscosity that will move in a porous medium in a unit time under a unit hydraulic gradient measured perpendicular to the direction of flow.

Isostatic rebound – The rise of a landmass in response to the relief of weight, via melting of glacial ice or by mass loss due to denudation.

Karst – A landscape formed in soluble rock, typically limestone, characterized by underground drainage.

Lithology – The physical properties of rock related to its composition, such as mineral content, texture, or grain size that defines its type.

Mixing dissolution – A geochemical process by which limestone is dissolved when two waters with different calcite saturation levels are mixed and result in an under saturated solution.

Permeability – The capacity of a porous medium to transmit fluid under equal pressure.

Polje – A large, flat-floored depression whose long axis is guided by structural trends.

Porosity – The percentage of bulk volume of a rock or soil that is occupied by interstitial space, whether isolated or connected.

Platform – A low-relief landscape formed through the deposition of sediments in a marine environment.

Phreatic – The subterranean zone below the water table, saturated with groundwater.

Soda straw – A tubular stalactite that maintains the diameter of drop of water and grows as water flows through it and calcite precipitates along the outside edge.

Speleogenesis – The process by which caves form, usually a geochemical mechanism.

Speleothem – A cave formation comprised of minerals that have precipitated under appropriate geochemical conditions, usually layers of calcite deposited where CO₂ outgasses from water.

Swale – A flat-floored depression that intercepts the water table for all or part of the year.

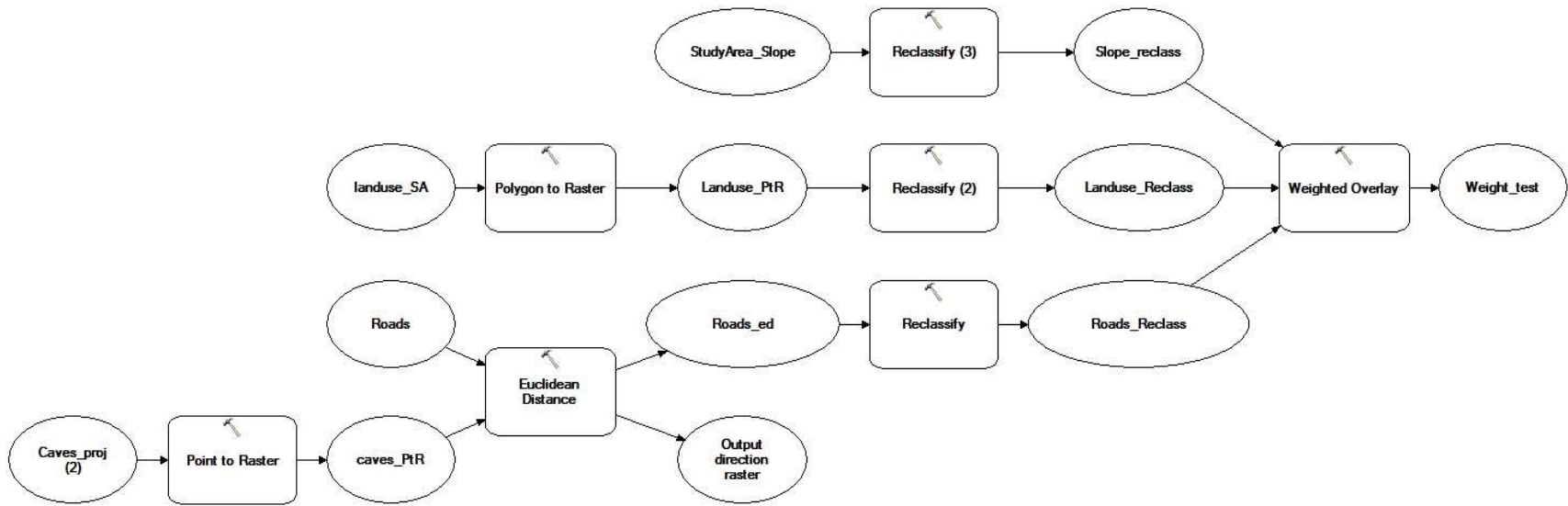
Transmissivity – The rate at which water of a given viscosity is transmitted through a unit width of the aquifer under a unit hydraulic gradient.

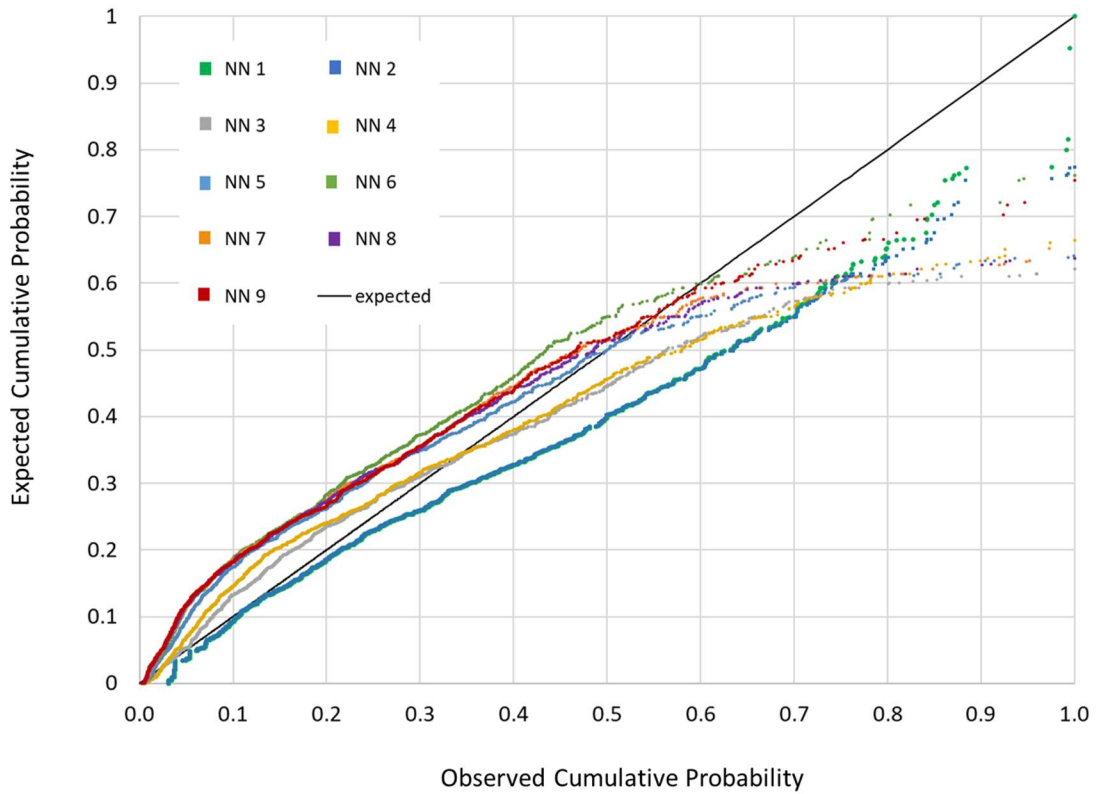
Uvala – A closed depression formed by the coalescence of smaller sinkholes.

Vadose – The subterranean zone above the water table where surface water may infiltrate but not all pore spaces are saturated.

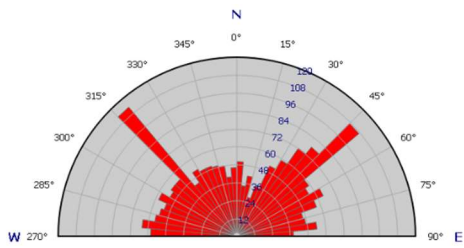
Water table or **Potentiometric surface** – The groundwater surface where the total pressure is equal to atmospheric pressure.

GIS Process Workflow for Weighted Overlay of Cave Entrance Access

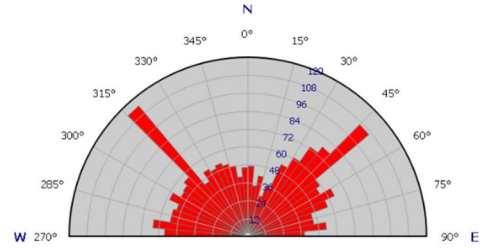




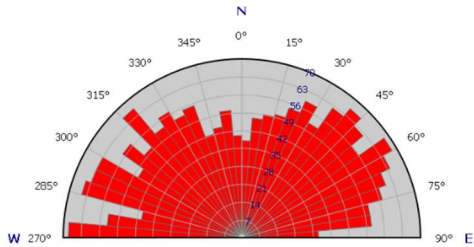
A P-P plot of 1st through 9th Nearest Neighbor distances. The black line represents the expected lognormal distribution of point distances among random points. The 1st Nearest Neighbor distance distributions plot below this line, which indicates that the data set is clustered at this scale. The distribution pattern changes from clustered to dispersed where the observed points cross the expected trend line.



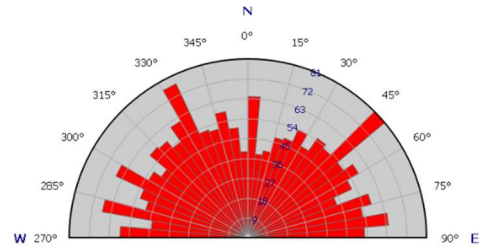
1st Nearest Neighbor, n= 1,971



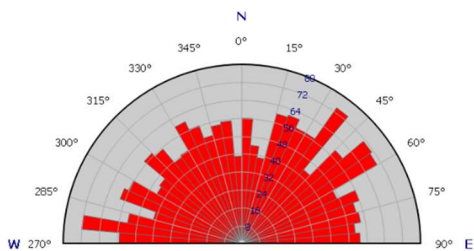
2nd Nearest Neighbor, n= 1,967



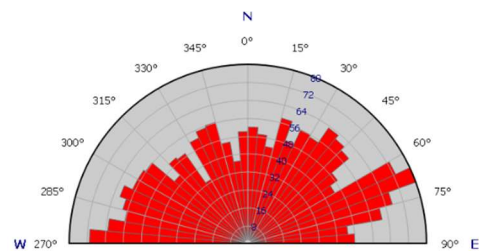
3rd Nearest Neighbor, n= 1,942



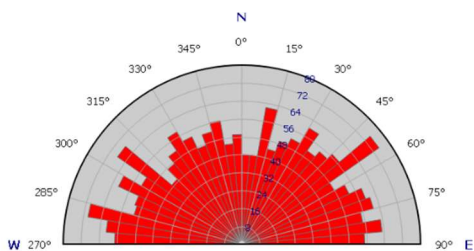
4th Nearest Neighbor, n= 1,953



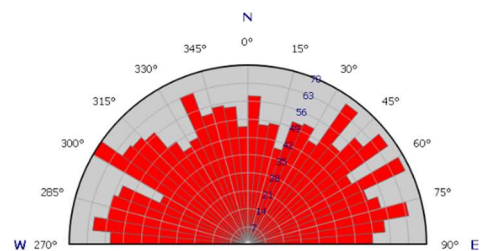
5th Nearest Neighbor, n= 1,949



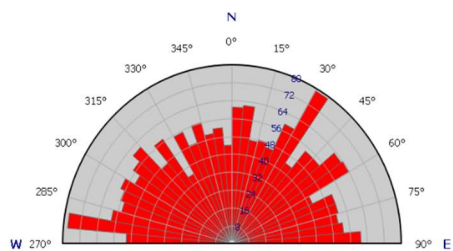
6th Nearest Neighbor, n= 1,964



7th Nearest Neighbor, n= 1,947



8th Nearest Neighbor, n= 1,947



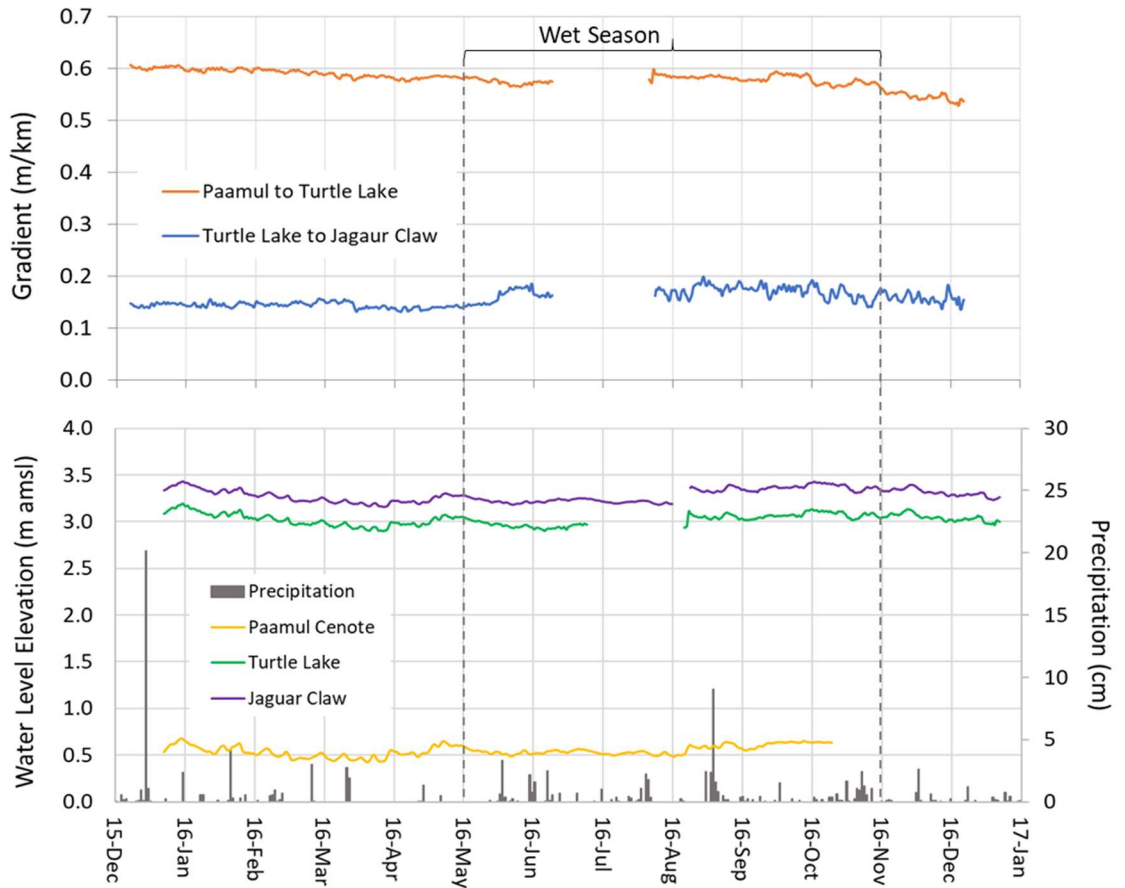
9th Nearest Neighbor, n= 1,962

APPENDIX B

Laboratory porosity measurements from samples collected in Quintana Roo, Mexico. Storativity is calculated based on the assumption that specific yield, which is equivalent to storativity in an unconfined aquifer, is ~80% of effective porosity in fractured limestone (Younger, 1993).

ID	Location	Type	LAT	LONG	Porosity (%)	Storativity
CY292	Chango mistico	cave	2273481	478186	9	0.07
AGD 40	Jaguar claw	cave	2272704	476292	58	0.46
AQ266	Jaguar Jaw	cave	2271635	477370	4	0.03
AP621	Jaguar Paw	cave	2272186	477021	13	0.11
CG19	Sech Chen	cave	2272762	479307	18	0.14
AP291	Gills Gamble	cave	2271659	477595	29	0.23
CY12	Turtle Lake	cave	2272341	476641	15	0.12
AQ411	Twisted sister	cave	2271741	477069	56	0.44
AR149	Lara Ha	surface	2273407	475905	7	0.05
CM	Chango mistico	surface	2272550	477710	2	0.02
HM	Howling Man	surface	2271125	478706	3	0.03
Angelita	Angelita	UW cave	2226783	439565	10	0.08
Casa	Casa Cenote	UW cave	2241024	459151	27	0.22
KL	Kaan Lum	UW cave	2229800	442146	27	0.22
C1	Calcite	control			0.1	0.00
Hays	Edwards Limestone	control			6	0.05
LS19	Austin Chalk	control			15	0.12

Coordinates in UTM (NAD83) Zone Q16-North



Water level and gradient responses to precipitation in the Paamul area from January to December 2016 at 30-min resolution. Data for water level elevations at long-term monitoring sites from January-December 2016 and August 2017-August 2018 are provided in the supplementary file Long-term *WLE_supplemental.xlsx*.

APPENDIX C

²³⁰Th dating results. The error is 2σ. These data are also provided electronically in *U-Th Supplemental.xlsx*.

Sample ID	Laboratory Name	²³⁸ U		²³² Th		²³⁰ Th / ²³² Th		²³⁰ Th / ²³⁸ U		$\delta^{234}\text{U}_{\text{Initial}}^{**}$		²³⁰ Th Age (yr BP) ^{***}	
		(ppb)		(ppt)		(n x10 ⁻⁶)		(activity)		(corrected)		(corrected)	
AA125	AA125	859	±2	36255	±729	269.6	±5.5	0.6901	±0.0022	-25	±3	131490	±1347
AA125OUT	AA125OUT	521.5	±1.6	27891	±570	288	±6	0.9349	±0.0033	-91	±7	397152	±18801
AA147a-OUT	AA147a	1291	±5	21113	±428	619.3	±12.7	0.6143	±0.0030	-18	±3	106013	±1049
AA147b-OUT	AA147b	1852	±7	25545	±520	737.2	±15.3	0.6167	±0.0033	-27	±3	108252	±1140
AA147c-IN	AA147c	1311	±5	32181	±656	435.4	±9.0	0.6482	±0.0035	-23	±3	117107	±1389
AA147c-OUT	AA147C-OUT	1452.4	±5.5	20411	±421	782	±16	0.6667	±0.0028	-32	±3	125281	±1206
AE818-IN	AE-818-IN	353.3	±0.5	751	±15	6789	±137	0.8749	±0.0016	43	±3	206606	±1667
AE818-OUT	AE818-OUT	258.3	±0.2	10540	±211	364	±7	0.9018	±0.0012	3	±3	249920	±2262
AE846a-OUT	AE846a	1508	±6	7284	±148	16.5	±0.4	0.0048	±0.0000	-11	±2	323	±101
AE846b-OUT	AE846b	1533	±5	2271	±46	18.6	±0.6	0.0017	±0.0000	-13	±2	72	±31
AE846b-IN	AE846b-IN	311.6	±0.3	3610	±72	1172	±24	0.8239	±0.0011	25	±2	180096	±888
AE849-OUT-2	AE849	766	±2	32248	±649	274.5	±5.6	0.7006	±0.0024	-12	±3	132749	±1383
AE849-OUT-2	AE849-OUT	1047.4	±3.2	21583	±441	546	±11	0.6818	±0.0024	-20	±3	128167	±1085
AE860-IN	AE860	193	±0	3422	±69	540.9	±10.9	0.5820	±0.0017	52	±3	88136	±598
AE917-IN	AE917	438.9	±0.6	38	±1	171735	±4956	0.9089	±0.0014	14	±3	252147	±2279
AE917-OUT-1	AE917-OUT	2274.6	±44	152969	±4366	91	±3	0.3708	±0.0077	-8	±11	48950	±2005
AE917-OUT-2	AE917-OUT	349.5	±1.0	5779	±118	673	±14	0.6745	±0.0022	-17	±3	125009	±981
AGD51-IN	AG05-IN	386.4	±0.4	1868	±37	3247	±65	0.9521	±0.0016	-10	±3	342447	±5919
AGD-OUT-1	AG05-OUT	716.1	±0.9	5640	±113	1825	±37	0.8717	±0.0013	-25	±2	236361	±1898
AGD5-OUT	AG05-OUT	1459.9	±4.5	21594	±437	1008	±20	0.9040	±0.0031	-30	±4	275419	±5473
AGD51-IN	AGD51B-IN	597.3	±0.7	162	±3	60753	±1232	0.9970	±0.0016	-1	±8	646106	±12493 6
AGD51-IN-2	AGD51B-OUT	1518.2	±3.3	28532	±574	833	±17	0.9495	±0.0025	-61	±5	404113	±15320
AJ359-OUT-1	AJ359	1557	±4	2848	±57	300.6	±6.2	0.0333	±0.0002	-9	±2	3609	±43

APPENDIX C. Continued

AJ359-OUT-2	AL359-MIDDLE	1394.6	±2.8	1626	±33	545	±11	0.0386	±0.0001	-11	±1	4237	±28
AL69a-OUT-1	AL69a	1330	±4	30314	±614	516.0	±10.6	0.7135	±0.0033	-36	±3	143863	±1622
AL69a-OUT-2	AL69A-OUT	1420.3	±4.6	16423	±336	1204	±25	0.8445	±0.0030	-48	±3	224108	±3263
AL69b-OUT-2	AL69b	1174	±3	24962	±505	660.4	±13.5	0.8515	±0.0036	-17	±3	215058	±3363
AL69b-OUT-2	AL69b-OUT	1241.9	±2.8	18971	±382	896	±18	0.8301	±0.0021	-32	±3	205551	±1988
AQ254	AQ254	338	±0	3663	±74	1513.5	±30.5	0.9949	±0.0024	40	±7	418685	±17433
BA273-IN-3	BA273F-M	1369.5	±3.1	48859	±984	334	±7	0.7229	±0.0019	-25	±2	144604	±1250
BA273-IN-2	BA273-F-MIDDLE	1021.2	±2.3	24461	±492	520	±10	0.7549	±0.0020	-27	±2	159763	±1304
BA273-OUT	BA273F-OUT	1235.8	±3.2	8031	±162	1999	±40	0.7880	±0.0023	-20	±3	175227	±1574
BA273-IN-1	BA273-IN	455.9	±0.9	8777	±176	728	±15	0.8498	±0.0023	-8	±3	209553	±2126
BA325-OUT	BA325F-OUT	808.5	±1.0	6581	±132	1703	±34	0.8407	±0.0014	-27	±2	211358	±1412
BA325-OUT-2	BA325F-OUT	924.4	±2.3	23452	±475	508	±10	0.7810	±0.0022	-23	±3	171907	±1568
BA325-IN	BA325-IN	224.0	±0.5	858	±17	3836	±77	0.8907	±0.0023	22	±4	229315	±2736
BA357-IN	BA357-IN	252.0	±0.3	970	±19	4049	±81	0.9455	±0.0016	-14	±3	332414	±5139
BA357-OUT	BA357-OUT	921.8	±1.8	32050	±643	367	±7	0.7733	±0.0018	-24	±2	167840	±1425
BA379-IN	BA379-IN	219.3	±0.3	711	±14	4784	±97	0.9411	±0.0017	-19	±4	327852	±5962
BA379-IN-3	BA379-M	233.1	±0.3	6990	±140	520	±10	0.9462	±0.0014	32	±4	287199	±3595
BA379-IN-2	BA379-MIDDLE	229.9	±0.3	3646	±73	907	±18	0.8722	±0.0015	0	±2	224002	±1797
BA379-OUT	BA379-OUT	828.7	±1.4	30354	±609	275	±6	0.6101	±0.0012	-16	±2	103891	±909
CD388-OUT	CD388	1272	±3	27315	±551	641.1	±13.1	0.8353	±0.0032	-26	±4	206738	±2931
CD388-IN	CD388-OUT	1293.4	±4.0	18335	±372	1070	±22	0.9203	±0.0031	-37	±4	305881	±7289
CY12c-IN	CY12	161.2	±0.2	650	±13	3914	±79	0.9576	±0.0015	5	±5	337960	±6486
CY12c-OUT	CY12-OUT	1029.6	±2.4	31639	±637	476	±10	0.8867	±0.0024	-25	±4	251301	±3566
NG1a-IN	NG1a	1086	±3	5424	±110	43.4	±0.9	0.0132	±0.0001	-14	±2	1249	±105
NG1b-OUT	NG1b	1179	±5	10631	±217	30.2	±0.7	0.0165	±0.0002	-14	±2	1506	±189
NG2a-IN	NG2a	1086	±3	2268	±46	113.4	±2.3	0.0144	±0.0001	-14	±2	1471	±45
NG2b-IN	NG2b	1215	±4	1640	±33	63.6	±1.4	0.0052	±0.0000	-15	±2	469	±29
NG2c-IN	NG2c	1262	±4	794	±16	64.9	±1.7	0.0025	±0.0000	-12	±2	186	±14

APPENDIX C. Continued													
NG2c-IN-2	NG2C-IN	209.4	±0.6	259	±5	2871	±59	0.2151	±0.0008	-16	±2	26767	±125
NG6-OUT	NG6	1140	±4	5107	±103	84.6	±1.7	0.0230	±0.0001	-12	±2	2363	±94
NG6-IN	NG6-IN	620.5	±1.8	518	±11	12037	±247	0.6093	±0.0020	-18	±2	105041	±691
AP930a-IN	S01-1-IN	1661.7	±4.1	25997	±524	649	±13	0.6156	±0.0017	-42	±2	110275	±740
AP930a-OUT	S01-1-OUT	1760.8	±3.9	40206	±810	430	±9	0.5950	±0.0015	-38	±2	103268	±724
AP930b-IN	S01-2-IN	1059.2	±2.2	12712	±256	1152	±23	0.8388	±0.0020	-33	±3	212449	±2153
AP930b-OUT	S01-2-OUT	1365.2	±2.4	16658	±335	1030	±21	0.7623	±0.0016	-53	±2	171767	±1144
AP930c-IN	S01-3-IN	1135.6	±1.9	20605	±414	792	±16	0.8714	±0.0018	-34	±3	240920	±2487
AP930c-OUT	S01-3-OUT	1026.5	±1.8	25319	±509	588	±12	0.8802	±0.0019	-38	±3	252321	±2985
Crustacea	SOUOSW05 (Coral)	2178.4	±2.0	13173	±264	3711	±74	1.3611	±0.0014	#####	###	#####	#####
CY12a-IN	TLLY12A-IN	1065.4	±1.7	16607	±333	919	±18	0.8689	±0.0017	-21	±3	231759	±2195
CY12a-OUT	TLLY12A- OUT	1011.9	±1.7	46989	±943	317	±6	0.8923	±0.0018	-25	±3	256681	±3036
CY12b-IN	TLLY12B-IN	382.3	±0.5	3837	±77	1552	±31	0.9446	±0.0022	-3	±3	317789	±5682
CY12b-OUT	TLLY12B- OUT	1173.9	±2.1	13751	±276	1210	±24	0.8595	±0.0019	-27	±3	226393	±2207
AR550	XPLOR (Coral)	438.2	±0.3	5471	±109	3021	±60	2.2874	±0.0020	#####	###	#####	#####

U decay constants: $\lambda_{238} = 1.55125 \times 10^{-10}$ (Jaffey et al., 1971) and $\lambda_{234} = 2.82206 \times 10^{-6}$ (Cheng et al., 2013).
 Th decay constant: $\lambda_{230} = 9.1705 \times 10^{-6}$ (Cheng et al., 2013).
 * $\delta^{234}\text{U} = ([^{234}\text{U}/^{238}\text{U}]_{\text{activity}} - 1) \times 1000$. ** $\delta^{234}\text{U}_{\text{initial}}$ was calculated based on ^{230}Th age (T), i.e., $\delta^{234}\text{U}_{\text{initial}} = \delta^{234}\text{U}_{\text{measured}} \times e^{\lambda_{234}T}$.
 Corrected ^{230}Th ages assume the initial $^{230}\text{Th}/^{232}\text{Th}$ atomic ratio of $4.4 \pm 2.2 \times 10^{-6}$. Those are the values for a material at secular equilibrium, with the bulk earth $^{232}\text{Th}/^{238}\text{U}$ value of 3.8. The errors are arbitrarily assumed to be 50%.
 ***B.P. stands for “Before Present” where the “Present” is defined as the year 1950 A.D.

REFERENCES

- Aguilar, Y., Bautista, F., Mendoza, M. E., Frausto, O., & Ihl, T. (2016). Density of karst depressions in Yucatán state, Mexico. *Journal of Cave and Karst Studies*, 78(2), 51–60. doi: 10.4311/2015ES0124
- AMCS. (2014). *unpublished data*. Austin, TX: Association for Mexican Cave Studies.
- Andreychouk, V., Błachowicz, T., & Domino, K. (2013). Fractal dimensions of cave for exemplary gypsum cave-mazes of Western Ukraine. *Landform Analysis*, 22, 3-8. doi: 10.12657/landfana.022.001
- Angel, J. C., Nelson, D. O., & Panno, S. V. (2004). Comparison of a new GIS-based technique and a manual method for determining sinkhole density: An example from Illinois' sinkhole plain. *Journal of Cave and Karst Studies*, 66 (1), 9-17.
- Arz, H. W., Lamy, F., Ganopolski, A., Nowaczyk, N., & Pätzold, J. (2007). Dominant Northern Hemisphere climate control over millennial-scale glacial sea-level variability. *Quaternary Science Reviews*, 26(3–4), 312–321. doi: 10.1016/j.quascirev.2006.07.016
- Atkinson, T. C. (1977). Diffuse flow and conduit flow in limestone terrain in the Mendip Hills, Somerset (Great Britain). *Journal of Hydrology*, 35(1–2), 93–110. doi: 10.1016/0022-1694(77)90079-8
- Back, W., & Hanshaw, B. B. (1970). Principles of chemical thermodynamics This provides a brief summary of some concepts and terminology which are. *Journal of Hydrology*, 10(1970), 330–368.
- Back, W., Hanshaw, B. B., Herman, J. S., & Van Driel, J. N. (1986). Differential dissolution of a Pleistocene reef in the groundwater mixing zone of coastal Yucatan, Mexico. *Geology*, 14(2), 137–140.
- Back, W., Hanshaw, B. B., Pyle, T. E., Plummer, L. N., & Weidie, A. E. (1979). Geochemical significance of groundwater discharge and carbonate solution to the formation of Caleta Xel Ha, Quintana Roo, Mexico. *Water Resources Research*, 15(6), 1521–1535.
- Bahk, J. J., Chough, S. K., & Han, S. J. (2000). Origins and paleoceanographic significance of laminated muds from the Ulleung Basin, East Sea (Sea of Japan). *Marine Geology*, 162(2–4), 459–477.
- Bauer-Gottwein, P., Gondwe, B. R. N., Charvet, G., Marín, L. E., Rebolledo-Vieyra, M., & Merediz-Alonso, G. (2011). Review: The Yucatán Peninsula karst aquifer, Mexico. *Hydrogeology Journal*, 19(3), 507–524. doi: 10.1007/s10040-010-0699-5

- Bautista, F., Bautista, D., & Delgado-Carranza, C. (2009). Calibration of the equations of Hargreaves and Thornthwaite to estimate the potential evapotranspiration in semi-arid and subhumid tropical climates for regional applications. *Atmosfera*, 22(4), 331–348.
- Beddows, P. A. (2004). *Groundwater Hydrology of a Coastal Conduit Carbonate Aquifer : Caribbean Coast of the Yucatán Peninsula , México*. PhD Dissertation, University of Bristol, Bristol, U.K.
- Beddows, P. A., & Mallon, E. K. (2018). Cave pearl data logger: A flexible arduino-based logging platform for long-term monitoring in harsh environments. *Sensors (Switzerland)*, 18(2). doi: 10.3390/s18020530
- Bendjoudi, H., & Hubert, P. (2002). The Gravelius compactness coefficient: Critical analysis of a shape index for drainage basins. *Hydrological Sciences Journal*, 47(6), 921–930. doi: 10.1080/02626660209493000
- Bintanja, R., Van De Wal, R. S. W., & Oerlemans, J. (2005). Modelled atmospheric temperatures and global sea levels over the past million years. *Nature*, 473(7055), 125–128. doi: 10.1038/nature03975
- Blanchon, P., Eisenhauer, A., Fietzke, J., & Liebetrau, V. (2009). Rapid sea-level rise and reef back-stepping at the close of the last interglacial highstand. *Nature*, 458(7240), 881–884. doi: 10.1038/nature07933
- Blanchon, P., & Shaw, J. (1995). Reef drowning during the last deglaciation: evidence for catastrophic sea-level rise and ice-sheet collapse. *Geology*, 23 (1), 4:8. doi: 10.1130/0091-7613(1995)023<0004:RDDTLD>2.3.CO;2
- Bolster, C. H., Genereux, D. P., & Saiers, J. E. (2001). Determination of specific yield for the Biscayne Aquifer with a canal-drawdown test. *Ground Water*, 39(5), 768–777. doi: 10.1111/j.1745-6584.2001.tb02368.x
- Brinkmann, R., Parise, M., & Dye, D. (2008). Sinkhole distribution in a rapidly developing urban environment: Hillsborough County, Tampa Bay area, Florida. *Engineering Geology*, 99(3–4), 169–184. doi: 10.1016/j.enggeo.2007.11.020
- Brook, G. A., Folkoff, M. E., & Box, E. O. (1983). A world model of soil carbon dioxide. *Earth Surface Processes and Landforms*, 8(1), 79–88. doi: 10.1002/esp.3290080108
- Carlson, T. (2007). An overview of the “triangle method” for estimating surface evapotranspiration and soil moisture from satellite imagery. *Sensors*, 7(8), 1612–1629. doi: 10.3390/s7081612

- Charvet, G. (2009). *Exploration, modeling and management of groundwater resources in northern Quintana Roo, Mexico*. MSc Thesis, Technical University of Denmark, Copenhagen, Denmark.
- Cheng, H., Edwards, R. L., Hoff, J., Gallup, C. D., Richards, D. A., & Asmerom, Y. (2000). The half-lives of uranium-234 and thorium-230. *Chemical Geology*, 169(1-2), 17-33. doi: 10.1016/S0009-2541(99)00157-6
- Cheng, H., Lawrence Edwards, R., Shen, C. C., Polyak, V. J., Asmerom, Y., Woodhead, J., ... Calvin Alexander, E. (2013). Improvements in ^{230}Th dating, ^{230}Th and ^{234}U half-life values, and U-Th isotopic measurements by multi-collector inductively coupled plasma mass spectrometry. *Earth and Planetary Science Letters*, 371–372, 82–91. doi: 10.1016/j.epsl.2013.04.006
- Climate-Data.org. (2019). Retrieved September 20, 2003, from <https://en.climate-data.org/>
- Coke, J. G. (2012). Underwater caves of the yucatán peninsula. In *Encyclopedia of Caves*, Culver, D. C., & White, W. B. (Eds.) (pp. 833-838). Amsterdam: Elsevier. doi: 10.1016/B978-0-12-383832-2.00120-1
- Collins, S. V., Reinhardt, E. G., Rissolo, D., Chatters, J. C., Nava Blank, A., & Luna Erreguerena, P. (2015). Reconstructing water level in Hoyo Negro, Quintana Roo, Mexico, implications for early Paleoamerican and faunal access. *Quaternary Science Reviews*, 124, 68-83. doi: 10.1016/j.quascirev.2015.06.024
- Connors, M., Hildebrand, A. R., Pilkington, M., Ortiz-Aleman, C., Chavez, R. E., Urrutia-Fucugauchi, J., ... Halpenny, J. F. (1996). Yucatán karst features and the size of Chicxulub crater. *Geophysical Journal International*, 127(3), F11-F14. doi: 10.1111/j.1365-246X.1996.tb04066.x
- Danielson, J. J., & Gesch, D. B. (2011). *Global multi-resolution terrain elevation data 2010 (GMTED2010)*. ESRI.
- Davis, J. C. (2002). *Statistics & Data Analysis in Geology* (3rd editio). New York, New York: John Wiley & Sons.
- De Waele, J., D'Angeli, I. M., Bontognali, T., Tuccimei, P., Scholz, D., Jochum, K. P., ... Tisato, N. (2018). Speleothems in a north Cuban cave register sea-level changes and Pleistocene uplift rates. *Earth Surface Processes and Landforms*, 43(11), 2313–2326. doi: 10.1002/esp.4393
- Dinno, A. (2017). *Dunn.test*. CRAN package for R. Portland, OR: Portland State University.

- Doctor, D. H., & Doctor, K. Z. (2012). Spatial analysis of geologic and hydrologic features relating to sinkhole occurrence in Jefferson County, West Virginia. *Carbonates and Evaporites*, 27(2), 143–152. doi: 10.1007/s13146-012-0098-1
- Doctor, D. H., & Young, J. A. (2013). An evaluation of automated GIS tools for delineating karst sinkholes and closed depressions from 1-meter LIDAR-derived digital elevation data. In *Proceedings of the 13th Multidisciplinary Conference on Sinkholes and the Engineering and Environmental Impacts of Karst*, held in Carlsbad, New Mexico, May 06-10, 2013, 449–458. doi: PNR61
- Dorale, J. A., Edwards, R. L., Alexander, E. C., Shen, C. C., Richards, D. A., & Cheng, H. (2004). Uranium-series dating of speleothems: current techniques, limits, & applications. In *Studies of cave sediments* (pp. 177–197). Boston: Springer US.
- Dorale, J. A., Onac, B. P., Fornós, J. J., Ginés, J., Ginés, A., Tuccimei, P., & Peate, D. W. (2010). Sea-level highstand 81, 000 years ago in mallorca. *Science*, 327(5967), 860–863. doi: 10.1126/science.1181725
- Dunn, J. O. (1964). Multiple Comparison Using Rank Sums. *Technometrics*, 5, 241-252.
- Elderfield, H., Ferretti, P., Greaves, M., Crowhurst, S., McCave, I. N., Hodell, D., & Piotrowski, A. M. (2012). Evolution of ocean temperature and ice volume through the mid-Pleistocene climate transition. *Science*, 337(6095), 704-709. doi: 10.1126/science.1221294
- Erskine, A. D. (1991). The Effect of Tidal Fluctuation on a Coastal Aquifer in the UK. *Groundwater*, 29(4), 556–562. doi: 10.1111/j.1745-6584.1991.tb00547.x
- Ester Lara, M. (1993). Divergent wrench faulting in the Belize Southern Lagoon: implications for Tertiary Caribbean plate movements and Quaternary reef distribution. *American Association of Petroleum Geologists Bulletin*, 77(6), 1041-1063.
- Ferris, J. G. (1951). Cyclic fluctuations of water levels as a basis for determining aquifer transmissibility. *International Assoc. for Hydrogeology Gen. Assem.*, 33(2), 17 p.
- Fetter, C. W. (2001). *Applied Hydrogeology* (4th ed.). Upper Saddle River, NJ: Pearson Education.
- Ford, C., Palmer, A., & White, W. (1988). Landform development; Karst. *The Geology of North America*, Vol. 0–2, pp. 401–412.
- Ford, D. C., & Williams, P. W. (2007). *Karst hydrogeology and geomorphology*. Chichester: John Wiley & Sons.

- Fragoso-Servón, P., Bautista, F., Frausto, O., & Pereira, A. (2014). Caracterización de las depresiones kársticas (forma, tamaño y densidad) a escala 1:50,000 y sus tipos de inundación en el Estado de Quintana Roo, México TT - Characterization of karst depressions (shape, size and density) at 1:50,000 scale and the associ. *Revista Mexicana de Ciencias Geológicas*, 31(1), 127–137.
- Fricke, H., & Meischner, D. (1985). Depth limits of Bermudan scleractinian corals: *Marine Biology*, 187, 175–187.
- Gao, Y., & Alexander, E. C. (2008). Sinkhole hazard assessment in Minnesota using a decision tree model. *Environmental Geology*, 54(5), 945–956. doi: 10.1007/s00254-007-0897-1
- Gao, Y., Alexander, E. C., & Barnes, R. J. (2005). Karst database implementation in Minnesota: Analysis of sinkhole distribution. *Environmental Geology*, 47(8), 1083–1098. doi: 10.1007/s00254-005-1241-2
- Gao, Y., Ramanathan, R., Hatipoglu, B., Demirkan, M. M., Adib, M. E., Gutierrez, J. J., ... Jr., D. B. (2012). *Development of Cavity Probability Map for Abu Dhabi Municipality Using Gis and Decision Tree Modeling*. In *14th Sinkhole Conference Proceedings*, NCKRI Symposium, held in Rochester, Minnesota, Oct 05-09, 2015, 277–287.
- García Espinosa, V., & Prieto Checa, I. (2010). *La competencia cultural como herramienta para la atención sanitaria a la población inmigrante* (Vol. 24). doi:10.1016/j.gaceta.2010.04.005
- Gill, E. D., & Lang, J. G. (1983). Micro-erosion meter measurements of rock wear on the Otway coast of southeast Australia. *Marine Geology*, 52(1-2), 141-156. doi: 10.1016/0025-3227(83)90025-7
- Gillison, A. N., & Brewer, K. R. W. (1985). The use of gradient directed transects or gradsects in natural resource surveys. *Journal of Environmental Management*, 20(April), 103–127. doi: 10.12890/2014_000086
- Gondwe, B. R. N. (2010). *Exploration , modelling and management of groundwater-dependent ecosystems in karst*. MSc Thesis, Technical University of Denmark, Copenhagen, Denmark.
- Gondwe, B. R. N., Lerer, S., Stisen, S., Marín, L., Rebolledo-Vieyra, M., Merediz-Alonso, G., & Bauer-Gottwein, P. (2010). Hydrogeology of the south-eastern Yucatan Peninsula: New insights from water level measurements, geochemistry, geophysics and remote sensing. *Journal of Hydrology*, 389(1-2), 1-17. doi: 10.1016/j.jhydrol.2010.04.044

- Gonzalez-Herrera, R. A. (1984). *Correlacion de muestras de roca en pozos de la ciudad de Merida*. BEng Thesis, Universidad de Mérida, Merida, Mexico.
- Gonzalez-Herrera, R. A. (1992). *Evolution of groundwater contamination in the Yucatan karstic aquifer*. MSc Thesis, University of Waterloo, Ontario, Canada.
- González-Herrera, R., Sánchez-y-Pinto, I., & Gamboa-Vargas, J. (2002). Groundwater-flow modeling in the Yucatan karstic aquifer, Mexico. *Hydrogeology Journal*, 10(5), 539–552. doi: 10.1007/s10040-002-0216-6
- Goreau, T. F., & Wells, J. . (1967). The shallow-water scleractinia of Jamaica: revised list of species and their vertical distribution range. *Bulletin of Marine Science*, 17(2), 442-453.
- Grant, K. M., Rohling, E. J., Bronk Ramsey, C., Cheng, H., Edwards, R. L., Florindo, F., ... Williams, F. (2014). Sea-level variability over five glacial cycles. *Nature Communications*, 5, 5076. doi: 10.1038/ncomms6076
- Gulley, J. D., B.Martin, J., & Brown, A. (2016a). Organic carbon inputs, common ions and degassing: rethinking mixing dissolution in coastal eogenetic carbonate aquifers. *Earth Surface Processes and Landforms*, 41(14), 2098–2110. doi: 10.1002/esp.3975
- Gulley, J. D., Mayer, A. S., Martin, J. B., & Bedekar, V. (2016b). Sea level rise and inundation of island interiors: Assessing impacts of lake formation and evaporation on water resources in arid climates. *Geophysical Research Letters*, 43(18), 9712–9719. doi: 10.1002/2016GL070667
- Harris, N. J. (1984). *Diagenesis of upper Pleistocene strand-plain limestones, northeastern Yucatan Peninsula, Mexico*. MSc Thesis, Univeristy of New Orleans, New Orleans, USA.
- Haukebo, S. L. (2014). *An ecological and biogeochemical characterization of a subterranean estuary in the Yucatan Peninsula, Mexico*. MSc Thesis, Texas A&M University, College Station, USA. doi: <http://dx.doi.org/110.21043/equilibrium.v3i2.1268>
- Hubbard, D. A. (2001). Sinkhole distribution of the Valley and Ridge province, Virginia. *Geotechnical and Environmental Applications of Karst Geology and Hydrology*. 1, 33-36.
- Humann, P., & Deloach, N. (1992). *Reed Coral Identification* (2nd ed.). Florida: New World Publication, Inc.
- Instituto Nacional de Estadística y Geografía (INEGI). (1997). *Geologic and Mineral Map of Mexico, Cozumel Quadrant F16-11, 2nd Edition*.

- Instituto Nacional de Estadística y Geografía (INEGI). (2015). Retrieved from: <http://en.www.inegi.org.mx/app/areasgeograficas/?ag=23>
- Instituto Nacional de Estadística y Geografía (INEGI). (2017). Retrieved from: <http://en.www.inegi.org.mx/app/areasgeograficas/?ag=23>
- Kaiser, L. (1983). Unbiased estimation in line-intercept sampling. *Biometrics*, 39(4), 965–976. doi: 10.2307/2531331
- Kambesis, P. N. (2014). *Influence of coastal processes on speleogenesis and landforms in the Caribbean Region*. PhD Dissertation, Mississippi State University, Starkville, Mississippi, USA.
- Kambesis, P. N., & Coke IV, J. G. (2016). The Sac Actun System, Quintana Roo, Mexico. *Boletín Geológico y Minero*, 127(1), 177–192.
- Kambesis, P. N., & Coke, J. G. (2013). *Overview of the Controls on Eogenetic Cave and Karst Development in Quintana Roo, Mexico*. In *Coastal Karst Landforms* (pp. 347-373). Springer, Dordrecht. doi: 10.1007/978-94-007-5016-6_16
- Kjerfve, B. (1981). Tides of the Caribbean Sea. *Journal of Geophysical Research*, 86(C5), 4243. doi: 10.1029/jc086ic05p04243
- Klimchouk, A., & Andrejchuk, V. (2005). Karst breakdown mechanisms from observations in the gypsum caves of the Western Ukraine: Implications for subsidence hazard assessment. *Environmental Geology*, 48(3), 336-359.
- Kopp, R. E., Simons, F. J., Mitrovica, J. X., Maloof, A. C., & Oppenheimer, M. (2009). Probabilistic assessment of sea level during the last interglacial stage. *Nature*, 462 (7275), 863-867. doi: 10.1038/nature08686
- Kruskal, W. H., & Wallis, W. A. (1952). Use of Ranks in One-Criterion Variance Analysis. *Journal of the American Statistical Association*, 47(260), 583–621. doi: 10.1080/01621459.1952.10483441
- Lauderdale, R. W., Ward, W. C., & Weidie, A. E. (1979). Carrillo Puerto Formation of Northeastern Quintana Roo, Mexico. *Gulf Coast Association of Geological Societies Transactions*, 29, 275–280.
- Lesser, J. . (1976). Resumen del estudio geohidrologico e hidroeoquimico de la peninsula de Yucatan. *Boletín de Divulgacion Technica*, 10, 10 p.
- Lisiecki, L. E., & Raymo, M. E. (2005). A Pliocene-Pleistocene stack of 57 globally distributed benthic $\delta^{18}\text{O}$ records. *Paleoceanography*, 20(1), 17 p. doi: 10.1029/2004PA001071

- Lodolo, E., Menichetti, M., Guzmán-Speziale, M., Giunta, G., & Zanolla, C. (2009). Deep structural setting of the North American-Caribbean plate boundary in eastern Guatemala. *Geofisica Internacional*, 48(3), 263–277.
- Lohman, S. W. (1972). Ground-water Hydraulics. *Geological Survey Professional Paper*, 48(708), 70 p. doi: 10.1016/0022-1694(80)90129-8
- Lopez R., E. (1975). Geological Summary of the Yucatan Peninsula. In A. E. M. Nairn (Ed.), *The Gulf of Mexico and the Caribbean*. New York: Plenum Press.
- Mann, P. (2007). Overview of the tectonic history of northern Central America. *Geological Society of America Special Papers*, 428, 19 p. doi: 10.1130/2007.2428(01).
- Marin, L. (1990). *Field investigations and numerical simulation of the karstic aquifer of northwest Yucatan, Mexico*. PhD Dissertation, Northern Illinois University, DeKalb, Illinois, USA.
- Marin, L. E., Perry, E. C., Essaid, H. I., & Steinich, B. (2016). Hydrogeological investigations and numerical simulation of groundwater flow in the karstic aquifer of northwestern Yucatan, Mexico. In *Coastal Aquifer Management-Monitoring, Modeling, and Case Studies*, p. 257-277.
- Marroni, M., Pandolfi, L., Principi, G., Malasoma, A., & Meneghini, F. (2009). Deformation history of the eclogite- and jadeitite-bearing mélange from North Motagua Fault Zone, Guatemala: Insights in the processes of a fossil subduction channel. *Geological Journal*, 44(2), 167-190. doi: 10.1002/gj.1145
- Martin, J. B., Gulley, J., & Spellman, P. (2012). Tidal pumping of water between Bahamian blue holes, aquifers, and the ocean. *Journal of Hydrology*, 416–417, 28–38. doi: 10.1016/j.jhydrol.2011.11.033
- Matsukura, Y., Maekado, A., & Aoki, H. (2014). *Ground lowering rates of reef-limestone terraces estimated from the height of pedestal rocks in Kikai-jima, Japan*. unpublished. Retrieved from: <http://citeseerx.ist.psu.edu/viewdoc/download?doi=10.1.1.545.5804&rep=rep1&type=pdf>
- McGee, D. K. (2010). *Microbial Influences on Karst Dissolution : The Geochemical Perspective, with a Chapter on Assessment of the Spreadsheets Across the Curriculum Project*. MSc Thesis, University of South Florida, St. Petersburg, Florida, USA.
- Medina-Elizalde, M. (2013). A global compilation of coral sea-level benchmarks: Implications and new challenges. *Earth and Planetary Science Letters*, 362, 310–318. doi: 10.1016/j.epsl.2012.12.001

- Medina-Elizalde, M., Burns, S. J., Polanco-Martínez, J. M., Beach, T., Lases-Hernández, F., Shen, C. C., & Wang, H. C. (2016). High-resolution speleothem record of precipitation from the Yucatan Peninsula spanning the Maya Preclassic Period. *Global and Planetary Change*, 138, 93–102. doi: 10.1016/j.gloplacha.2015.10.003
- Miller, K. G., Kominz, M. A., Browning, J. V., Wright, J. D., Mountain, G., Katz, M. E., ... Pekar, S. F. (2005). The Phanerozoic Record of Global Sea-Level Change. *Science*, 310, 1293–1298. doi: 10.1126/science.1116412
- Miller, T. E. (1996). Geologic and hydrologic controls on karst and cave development in Belize. *Journal of Cave and Karst Studies*, 58(2), 100–120.
- Moore, G. (1992). Hydrograph Analysis in a Fractured Rock Terrane. *Groundwater*, 30(3), 390-395. doi: 10.1111/j.1745-6584.1992.tb02007.x
- Moore, Y. H., Stoessell, R. K., & Easley, D. H. (1992). Fresh-Water/Sea-Water Relationship Within a Ground-Water Flow System, Northeastern Coast of the Yucatan Peninsula. *Groundwater*, 30(3), 343–350. doi: 10.1111/j.1745-6584.1992.tb02002.x
- Moseley, G. E., Smart, P. L., Richards, D. A., & Hoffmann, D. L. (2013). Speleothem constraints on marine isotope stage (MIS) 5 relative sea levels, Yucatan Peninsula, Mexico. *Journal of Quaternary Science*, 28(3), 293–300. doi: 10.1002/jqs.2613
- Muhs, D. R. (1992). The last interglacial-glacial transition in North America: Evidence from uranium-series ages of coastal deposits. *The Last Interglacial-Glacial Transition in North America*, 270, 31–51. doi: 10.1130/SPE270-p31
- Myroie, J. E., & Carew, J. (1990). The flank margin model for dissolution cave development in carbonate platforms. *Earth Surface Processes and Landforms*, 15, 413–424.
- Myroie, J. E., & Carew, J. J. (1988). Solution conduits as indicators of late Quaternary sea level position. *Quaternary Science Reviews*, 7(1), 55–64.
- Myroie, J. E., Lace, M. J., Albury, N., & Myroie, J. R. (2018). *Mid-Quaternary sea-level highstands in the Bahamian archipelago: Evidence from karst denudation and flank margin cave position*. Geological Society of America. doi: 10.1130/abs/2018am-315535
- Myroie, J. E., & Myroie, J. R. (2009). Caves as sea level and uplift indicators, Kangaroo Island, South Australia. *Journal of Cave and Karst Studies*, 71(1), 32-47.
- Myroie, J. E., & Myroie, J. R. (2018). Role of karst denudation on the accurate assessment of glacio-eustasy and tectonic uplift on carbonate coasts. In *Geological Society Special Publication*, 466, 171–185. Geological Society of London.

- Neuendorf, K., Mehl, J., & Jackson, J. (2005). *Glossary of Geology* (5th ed.). Alexandria, VA: American Geological Institute.
- NOAA. (n.d.). NOAA Hurricane Records. Retrieved August 20, 2019, from 2019 website: <https://coast.noaa.gov/hurricanes/>
- Padilla-Sanchez, R. J. (2013). *Tectonic Map of Mexico*. División de Ingeniería en Ciencias de la Tierra, Universidad Nacional Autónoma de México (UNAM).
- Palmer, A. N. (1991). Origin and morphology of limestone caves. *Geological Society of America Bulletin*, *103*(1), 1-21. doi: 10.1130/0016-7606(1991)103<0001:OAMOLC>2.3.CO;2
- Palmer, A. N. (2007). *Cave Geology* (4th ed.; R. . Watson & E. Winkler, Eds.). Dayton, OH.
- Pardo-Igúzquiza, E., Dowd, P., Durán, J., & Robledo-Ardila, P. (2019). A review of fractals in karst. *International Journal of Speleology*, *48*, 11-20. doi: 10.5038/1827-806x.48.1.2218
- Perry, E. C., Swift, J., Gamboa, J., Reeve, A., Sanborn, R., Marin, L., & Villasuso, M. (1989). Geologic and environmental aspects of caliche formation, north coast, Yucatan, Mexico. *Geology*, *17*, 818–821.
- Perry, E., Paytan, A., Pedersen, B., & Velazquez-Oliman, G. (2009). Groundwater geochemistry of the Yucatan Peninsula, Mexico: Constraints on stratigraphy and hydrogeology. *Journal of Hydrology*, *367*(1–2), 27–40. doi: 10.1016/j.jhydrol.2008.12.026
- Perry, E., Velazquez-oliman, G., & Marin, L. (2002). The Hydrogeochemistry of the Karst Aquifer System of the Northern Yucatan Peninsula, Mexico. *International Geology Review*, *44*(3), 191–221. doi: 10.2747/0020-6814.44.3.191
- Polyak, V. J., Onac, B. P., Fornós, J. J., Hay, C., Asmerom, Y., Dorale, J. A., ... Ginés, A. (2018). A highly resolved record of relative sea level in the western Mediterranean Sea during the last interglacial period. *Nature Geoscience*, *11*(11), 860–864. doi: 10.1038/s41561-018-0222-5
- Pope, K. O., Ocampo, A. C., Kinsland, G. L., & Smith, R. (1996). Surface expression of the Chicxulub crater. *Geology*, *24*(6), 537-530. doi: 10.1130/0091-7613(1996)024<0527:SEOTCC>2.3.CO;2
- Quintana Roo Speleological Society. (2019). Unpublished survey data. Retrieved from: <http://caves.org/project/qrss/qrss.htm>

- Rehrl, C., Birk, S., & Klimchouk, A. (2008). Speleogenesis in hypogene settings : Development and validation of numerical models by field evidence. *Geophysical Research Abstracts*.
- Remson, I., Hornberger, G. M., & Molz, F. J. (1971). *Numerical Methods in Subsurface Hydrology*. Upper Saddle River, NJ: Wiley-Interscience, pubs. John Wiley & Sons. Inc.
- Revelle, R., & Emery, K. O. (1957). Chemical Erosion of Beach Rock and Exposed Reef Rock: Bikini and Nearby Atolls, Marshall Islands. *Geological Survey Professional Paper 260-T*, 11.
- Richards, D., & Richards, S. (2007). Overview of the Geology and Hydrology of Coastal Quintana Roo. *AMCS Activities Newsletter*, 30, 104–108.
- Rodriguez, C. J. (1982). *Petrology and diagenesis of Pleistocene limestones, northeastern Yucatan Peninsula, Mexico*. MSc Thesis, University of New Orleans, New Orleans, USA.
- Rohling, E. J., Foster, G. L., Grant, K. M., Marino, G., Roberts, A. P., Tamisiea, M. E., & Williams, F. (2014). Sea-level and deep-sea-temperature variability over the past 5.3 million years. *Nature*, 508 (7497), 477-482. doi: 10.1038/nature13230
- Rohling, E. J., Grant, K., Bolshaw, M., Roberts, A. P., Siddall, M., Hemleben, C., & Kucera, M. (2009). Antarctic temperature and global sea level closely coupled over the past five glacial cycles. *Nature Geoscience*, 2 (7), 500-504. doi: 10.1038/ngeo557
- Rosencrantz, E. (1990). Structure and tectonics of the Yucatan Basin, caribbean Sea, as determined from seismic reflection studies. *Tectonics*, 9(5), 1037–1059. doi: 10.1029/TC009i005p01037
- Rotzoll, K., Gingerich, S. B., Jenson, J. W., & El-Kadi, A. I. (2013). Etablissement des propriétés hydrauliques d'après l'atténuation de la marée dans l'Aquifère Lenticulaire du Nord de Guam, Territoire de Guam, USA. *Hydrogeology Journal*, 21(3), 643–654. doi: 10.1007/s10040-012-0949-9
- Sanford, W. E., & Konikow, L. F. (1989). Porosity development in coastal carbonate aquifers. *Geology*, 17(3), 249–252. doi: 10.1130/0091-7613(1989)017<0249:PDICCA>2.3.CO;2
- Scholz, D., & Mangini, A. (2007). How precise are U-series coral ages? *Geochimica et Cosmochimica Acta*, 71(8), 1935–1948.
- Shakun, J. D., Lea, D. W., Lisiecki, L. E., & Raymo, M. E. (2015). An 800-kyr record of global surface ocean $\delta^{18}\text{O}$ and implications for ice volume-temperature coupling. *Earth and Planetary Science Letters*, 426, 58-68. doi: 10.1016/j.epsl.2015.05.042

- Sheen, S. W. (2000). A World Model of Chemical Denudation in Karst Terrains. *Professional Geographer*, 52(3), 397–406. doi: 10.1111/0033-0124.00234
- Shevenell, L. (1996). Specific Yields and Continuum Transmissivities. *Hydrology*, 174, 331–355.
- Smart, P. L., Beddows, P. A., Coke, J., Doerr, S., Smith, S., & Whitaker, F. F. (2006). Cave development on the Caribbean coast of the Yucatan Peninsula, Quintana Roo, Mexico. *Special Paper 404: Perspectives on Karst Geomorphology, Hydrology, and Geochemistry - A Tribute Volume to Derek C. Ford and William B. White*, 2404(10), 105–128.
- Smart, P. L., Dawans, J. M., & Whitaker, F. (1988). Carbonate dissolution in a modern mixing zone. *Nature*, 335(6193), 811–813. doi: 10.1038/335811a0
- Sosdian, S., & Rosenthal, Y. (2009). Deep-sea temperature and ice volume changes across the pliocene-pleistocene climate transitions. *Science*, 325 (5938), 306-310.
- Spencer, T. (1985). Marine erosion rates and coastal morphology of reef limestones on Grand Cayman Island, West Indies. *Coral Reefs*, 4(2), 59-70. doi: 10.1007/BF00300864
- Spratt, R. M., & Lisiecki, L. E. (2016). A Late Pleistocene sea level stack. *Climate of the Past*, 2(4), 1079–1092. doi: 10.5194/cp-12-1079-2016
- Sprouse, P. (2019). *unpublished cave survey data*. Underground Texas Grotto, Austin, TX, USA.
- Steig, E. J. (2008). Sources of uncertainty in ice core data. *Reducing and Representing Uncertainties in High-Resolution Proxy Data*. In conference proceedings of the International Centre for Theoretical Physics, Trieste, Italy, June 9 - 11, 2008. Retrieved from: <ftp://ftp.ncdc.noaa.gov/pub/data/paleo/icecore/ice-cores.pdf>
- Steiger, N. J., Steig, E. J., Dee, S. G., Roe, G. H., & Hakim, G. J. (2017). Climate reconstruction using data assimilation of water isotope ratios from ice cores. *Journal of Geophysical Research*, 122(3), 1545–1568. doi: 10.1002/2016JD026011
- Stevanović, Z. (2015). *Karst Aquifers—Characterization and Engineering*. Professional Practice in Earth Science Series, Springer International, Switzerland. 692 p. doi: 10.1007/978-3-319-12850-4
- Szabo, B. J., Ward, W. C., Weidie, A. E., & Brady, M. J. (1978). Age and magnitude of the late Pleistocene sea-level rise on the eastern Yucatan Peninsula. *Geology*, 6(12), 713–715. doi: 10.1130/0091-7613(1978)6<713:AAMOTL>2.0.CO;2

- Thompson, W. G., Spiegelman, M. W., Goldstein, S. L., & Speed, R. C. (2003). An open-system model for U-series age determinations of fossil corals. *Earth and Planetary Science Letters*, 210(1–2), 365–381.
- Trudgill, S. T. (1976). The marine erosion of limestones on Aldabra Atoll, Indian Ocean. *Z. Geomorph. Suppl.*, 26, 164-200.
- Tuccimei, P., Gines, J., Delitala, M. C., Gracia, F., Fornos, J. J., & Taddeucci, A. (2006). Last interglacial sea level changes in Mallorca island (Western Mediterranean). High precision U-series data from phreatic overgrowths on speleotherms. *Z. Geomorph. N. E.*, 50(1), 1-21.
- Tulaczyk, T. . (1993). *Karst geomorphology and hydrogeology of the northeastern Yucatan Peninsula, Mexico*. MSc Thesis, Northern Illinois University, deKalb, Illinois, USA.
- Tulaczyk, T. ., Perry, E. C., Duller, C. E., & Villasuso, M. (1993). Influence of the Holbox fracture zone on the karst geomorphology and hydrogeology of northern Quintana Roo, Yucatan Peninsula, Mexico. In Beck (Ed.), *Applied Karst Geology* (pp. 181–188). Rotterdam: Balkema.
- UNESCO. (2019). United Nations Educational, Scientific, and Cultural Organization. Retrieved from: <https://whc.unesco.org/en/list/410/>
- Vesica, P. L., Tuccimei, P., Turi, B., Fornós, J. J., Ginés, A., & Ginés, J. (2000). Late Pleistocene Paleoclimates and sea-level change in the Mediterranean as inferred from stable isotope and U-series studies of overgrowths on speleothems, Mallorca, Spain. *Quaternary Science Reviews*, 19(9), 865-879. doi: 10.1016/S0277-3791(99)00026-8
- Waelbroeck, C., Labeyrie, L., Michel, E., Duplessy, J. C., McManus, J. F., Lambeck, K., ... Labreacherie, M. (2002). Sea-level and deep water temperature changes derived from benthic foraminifera isotopic records. *Quaternary Science Review*, 21, 295–305. doi: 10.1016/j.hrthm.2007.04.016
- Ward, W. C. (1978). Indicators of Climate in Carbonate Dune Rocks. In *Geology and Hydrogeology of Northeastern Yucatan* (pp. 191–208). New Orleans: New Orleans Geological Society.
- Ward, W. C., Weidie, A. E., & Back, W. (1985). Geology and Hydrogeology of the Yucatan and Quaternary Geology of Northeastern Yucatan Peninsula. *New Orleans Geol.Soc.*, 1–160.
- Warner, G. (2012). *Corals of Florida & the Caribbean*. Gainesville, FL.: University Press of Florida.

- Warren, W. G., & Olsen, P. F. (1964). A Line Intersect Technique for Assessing Logging Waste. *Forest Science*, *10*(3), 267-276.
- White, W. B. (2002). Karst hydrology: Recent developments and open questions. *Engineering Geology*, *65*(2-3), 85-105. doi: 10.1016/S0013-7952(01)00116-8
- White, W. B. (2003). Conceptual models for karstic aquifers. In *Karst Modeling: Special Publication 5*, Palmer, A.N., Palmer, M.V., and Sasowsky, I.D. (eds.), The Karst Waters Institute, Charles Town, West Virginia (USA), 11-16.
- Williams, P. W. (1981). Morphometric Analysis of Polygonal Karst in New Guinea. In M. M. Sweeting (ed.), *Karst Geomorphology* (p. 374-409). Stroudsburg, PA: Hutchinson Ross Publishing Company.
- Woo, H. B., Panning, M. P., Adams, P. N., & Dutton, A. (2017). Karst-driven flexural isostasy in North-Central Florida. *Geochem. Geophys. Geosyst.*, *18*, 3327-3339. doi: 10.1002/2017GC006934
- Worthington, S., Jeannin, P.-Y., Alexander, E. C., Davies, G. J., & Schindel, G. M. (2017). Contrasting definitions for the term 'karst aquifer.' *Hydrogeology Journal*, *25*(5), 1237-1240. doi: 10.1007/s10040-017-1628-7
- Worthington, S. R. H., Ford, D. C., & Beddows, P. A. (2001). Porosity and permeability enhancement in unconfined carbonate aquifers as a result of solution. *Speleo Brazil 2001 - 13th International Congress of Speleology*, (November 2015).
- Wu, Q., Deng, C., & Chen, Z. (2016). Automated delineation of karst sinkholes from LiDAR-derived digital elevation models. *Geomorphology*, *266*, 1-10. doi: 10.1016/j.geomorph.2016.05.006
- Yong Technology Inc. (2014). *GeoRose*. Retrieved from: <http://www.yongtechnology.com/download/georose>
- Younger, P. L. (1993). Simple generalized methods for estimating aquifer storage parameters. *Quarterly Journal of Engineering Geology and Hydrogeology*, *26*(2), 127-135. doi: 10.1144/gsl.qjeg.1993.026.02.04
- Zhu, J., & Pierskalla, W. P. (2016). Applying a weighted random forests method to extract karst sinkholes from LiDAR data. *Journal of Hydrology*, *533*, 343-352.